IMPACT OF NON-UNIFORM TEMPERATURE DISTRIBUTION ON THERMAL STRESS BEHAVIOUR IN ENERGY WALLS

by
Mert Güner
B.S., Civil Engineering, Boğaziçi University, 2016
M.S., Civil Engineering, Boğaziçi University, 2019

Submitted to the Institute for Graduate Studies in
Science and Engineering in partial fulfillment of
the requirements for the degree of
Doctor of Philosophy

Graduate Program in Civil Engineering
Boğaziçi University
2025

To my father, Zorlu Güner

ACKNOWLEDGEMENTS

Firstly, I would like to express my sincere gratitude to my advisor, Prof. Özer Çinicioğlu, and my co-advisor, Dr. Melis Sütman, for their continuous support, guidance, and encouragement throughout the course of my doctoral research. Their insightful feedback, expertise, and unwavering patience have been invaluable to the successful completion of this dissertation.

I would also like to extend my appreciation to Prof. Pelin Özer Tohumcu and Assoc. Prof. İrem Zeynep Yıldırım for serving on my thesis committee and for their constructive feedback, which significantly contributed to the quality of this work.

Special thanks go to my colleagues, Semra Polat and Uğur Can Erginağ, for their collaboration, friendship, and the many insightful discussions that enriched my research experience.

I am profoundly grateful to my mother, Ayşe, and my sister, Hatice, for their unwavering support, love, and belief in me throughout this journey.

Finally, I would like to acknowledge the financial support provided by TÜBİTAK (The Scientific and Technological Research Council of Türkiye) under the BİDEB 2211-A program.

ABSTRACT

IMPACT OF NON-UNIFORM TEMPERATURE DISTRIBUTION ON THERMAL STRESS BEHAVIOUR IN ENERGY WALLS

Energy geostructures, such as energy piles and energy walls, serve a dual purpose by providing both structural stability and renewable thermal energy exchange. While their thermo-mechanical behaviour has been widely studied, many investigations simplify the problem by assuming uniform temperature distributions. This assumption fails to capture the realistic, spatially varied temperature fields caused by the flow of heat-transfer fluids within embedded piping networks. These temperature variations give rise to intricate three-dimensional thermal stress patterns, which are further shaped by both internal and external boundary conditions. This research addresses the resulting stress responses in energy walls exposed to non-uniform thermal loading under both heating and cooling operations. A comprehensive three-dimensional numerical model, verified using COMSOL Multiphysics, was employed to simulate the effects of spatial temperature differences on stress development. The simulation outcomes highlight the emergence of significant circumferential, radial, and axial stresses driven by thermal gradients and the configuration of mechanical constraints. During heat injection, zones surrounding the heated pipes experienced marked compressive stress, whereas cooling operations led to the formation of tensile stresses, particularly near the piping zones. Elevated tensile stresses were also observed at sensitive regions, such as the interface with surrounding soil and building-facing surfaces. These results underline the critical need for incorporating non-uniform temperature distributions and realistic boundary conditions into the design and evaluation of energy geostructures. Neglecting these aspects can introduce substantial errors in stress predictions, potentially affecting the durability and performance of such systems over time.

ÖZET

ENERJİ DUVARLARINDA HOMOJEN OLMAYAN SICAKLIK DAĞILIMININ TERMAL GERİLME DAVRANIŞI ÜZERİNDEKİ ETKİSİ

Enerji kazıkları ve enerji duvarları gibi enerji jeo-yapıları, hem yapısal stabilite sağlama hem de yenilenebilir ısı enerjisi alışverişi işlevi görerek çift amaçlı bir kullanım sunmaktadır. Termo-mekanik davranışları kapsamlı şekilde incelenmiş olsa da, birçok çalışma bu sistemi sabit sıcaklık dağılımları varsayımıyla basitleştirmektedir. Ancak bu varsayım, gömülü boru ağları içerisinden geçen ısı transfer akışkanlarının oluşturduğu gerçekçi ve konumsal olarak değişken sıcaklık alanlarını yansıtamamaktadır. Bu sıcaklık farkları, iç ve dış sınır koşulları tarafından şekillendirilen karmaşık üç boyutlu termal gerilme dağılımlarına yol açmaktadır. Bu çalışma, hem ısıtma hem de soğutma işlemleri sırasında, gerçekçi ve homojen olmayan sıcaklık dağılımlarında enerji duvarlarında oluşan gerilme tepkilerini ele almaktadır. COMSOL Multiphysics yazılımı kullanılarak doğrulanmış, kapsamlı bir üç boyutlu sayısal model yardımıyla, sıcaklık farklarının gerilme gelişimine etkisi simüle edilmiştir. Elde edilen sonuçlar, sıcaklık gradyanları ve mekanik sınır koşullarına bağlı olarak belirgin çevresel, radyal ve eksensel gerilmelerin ortaya çıktığını göstermektedir. Isı enjeksiyonu sırasında, ısınan boruların çevresinde belirgin basınç gerilmeleri gözlenirken; ısı çekimi uygulamalarında özellikle borulara yakın bölgelerde çekme gerilmeleri oluşmuştur. Ayrıca, çevredeki zemin ile duvar arasındaki arayüz gibi hassas bölgelerde ve binaya bakan yüzeylerde yüksek çekme gerilmeleri kaydedilmiştir. Bu bulgular, enerji jeo-yapılarının tasarım ve analiz süreçlerinde gerçekçi, konumsal olarak değişken sıcaklık dağılımlarının ve uygun mekanik sınır koşullarının dikkate alınmasının kritik önemini ortaya koymaktadır. Bu unsurların göz ardı edilmesi, gerilme tahminlerinde ciddi hatalara yol açabilir ve bu yapıların uzun vadeli dayanıklılığı ile performansını olumsuz yönde etkileyebilir.

TABLE OF CONTENTS

LIST OF FIGURES

LIST OF TABLES

LIST OF SYMBOLS

c	Specific heat capacity
C	Volumetric heat capacity
E	Young's modulus
T	Temperature
T_{air}	Ambient air temperature
T_{in}	Inlet temperature of the heat exchanger fluid
T_{out}	Outlet temperature of the heat exchanger fluid
T_f	Temperature of the fluid
T_{ref}	Reference temperature
α	Thermal expansion coefficient
γ	Unit weight
$\varepsilon_{blocked}$	Blocked strain
ε_{free}	Free thermal strain
ε_M	Building load induced strain
ε_{obs}	Observed strain
λ	Thermal conductivity coefficient
v	Poisson's ratio
ρ	Density
σ_M	Building load induced stress
σ_{th}	Thermally induced axial stress

LIST OF ACRONYMS / ABBREVIATONS

3D	Three-dimensional
ASHRAE	American Society of Heating Refrigerating and Air-Conditioning Engineers
CFA	Continuous Flight Auger
COP	Coefficient of Performance
GSHP	Ground Source Heat Pump
PE-100	High-Density Polyethylene Pipe Material with a Minimum Required Strength of 10 MPa at 20°C
PEX	Crosslinked Polyethylene
HDPE	High Density Polyethylene

1. INTRODUCTION

The global energy landscape is undergoing a profound transformation in response to the mounting pressures of climate change, fossil fuel depletion, and urban population growth. As cities continue to expand and energy demands rise, there is an urgent need to adopt integrated and sustainable solutions that align infrastructure development with low-carbon energy production. In this context, shallow geothermal energy has emerged as a promising renewable resource that can be harnessed directly from the ground to support low-carbon building operations.

Energy geostructures represent a novel and efficient approach to this transition. By embedding heat exchange systems within conventional geotechnical elements such as piles, walls, and slabs, these structures are capable of fulfilling dual roles: providing structural support while simultaneously serving as a medium for ground-source heating and cooling (Brandl, 2006; Laloui and Sutman, 2021). This multifunctionality makes them especially attractive in urban settings where space is limited and the energy footprint of buildings must be minimized.

Despite the growing implementation of energy geostructures, challenges remain in predicting their long-term thermal and mechanical performance. Their behaviour is influenced by a complex interplay of factors including ground thermal properties, structural boundary conditions, operational regimes, and climate variability. Accurate numerical modeling is therefore essential to ensure safe design and reliable performance over the lifespan of such systems.

This research specifically addresses the behaviour of energy walls, which are energy geostructures incorporated into underground retaining systems. The primary focus is on understanding the thermally induced stresses generated by non-uniform temperature distributions within energy walls during heat injection (summer conditions) and heat extraction (winter conditions). To achieve this, a detailed numerical model has been developed using COMSOL Multiphysics, enabling the investigation of coupled thermal and structural responses. The numerical approach was validated against experimental data obtained from previously published full-scale tests on an energy pile (Sutman, 2016) and an energy wall (Xia et al., 2012), ensuring the reliability of the simulations. By analyzing stress development along key sections of the energy wall, this study aims to clarify how thermally induced stresses arise under realistic thermal loading conditions.

Furthermore, the dissertation explores how different thermal zones within the energy wall influence the distribution of these stresses. The wall cross-section was categorized into three distinct zones based on their unique temperature profiles: Zone 1, characterized by a circular temperature field around the heat exchanger pipes; Zone 2, serving as a transitional area where temperature profiles shift; and Zone 3, exhibiting a linear temperature gradient near the excavation side (building side). Each zone was analyzed in detail to reveal how these varying temperature distributions affect local stress patterns and structural responses.

In addition to stress characterization, this study also considers the practical implications of the findings by discussing potential structural risks associated with observed stress levels. Given that concrete typically has low tensile strength, specific attention is given to tensile stresses, as these can pose significant risks to structural integrity if overlooked in the design phase. As such, the results provide valuable guidance to engineers and designers regarding critical considerations for long-term safety and reliability.

Ultimately, this study aims to contribute valuable insights to the existing literature on energy geostructures, specifically by enhancing the understanding of energy wall behaviour under realistic operational conditions. The findings not only highlight the limitations of conventional simplified approaches but also demonstrate the necessity and benefits of adopting detailed numerical modeling methods. The outcomes of this research are intended to assist engineers and designers in making informed decisions, ultimately improving the safety and sustainability of geothermal energy integration in urban construction.

1.1. Aims and Objectives

The primary aim of this research is to investigate thermally induced stresses in energy walls resulting from realistic, non-uniform temperature distributions. By utilizing advanced three-dimensional numerical modeling techniques, the study aims to capture the complete stress response of energy walls under actual operational conditions. Unlike previous studies that often assume uniform or simplified temperature profiles, this research addresses how genuine temperature gradients affect structural behaviour, providing a more accurate understanding of the stresses that arise within energy walls.

To achieve this overarching aim, several key objectives were established. Initially, a comprehensive and validated three-dimensional thermo-mechanical model was developed using COMSOL Multiphysics. This modeling platform was selected for its capability to simultaneously simulate heat transfer and structural deformation, allowing detailed exploration of the interactions between thermal effects and mechanical stresses. The model was carefully structured to represent the typical geometry, material characteristics, and surrounding conditions of energy walls, ensuring realistic simulation outcomes

Following the development and validation of the model, two representative operational scenarios were investigated: a summer scenario (heat injection) and a winter scenario (heat extraction). These simulations provided valuable insights into how temperature and stress distributions form and evolve within energy walls under different thermal loading conditions. By examining both heating and cooling operations, the study was able to analyze the directional impacts of thermal loads on stress development, highlighting critical differences in wall behaviour during various seasonal conditions.

Another significant objective was to capture the inherently non-uniform temperature distributions that naturally occur within energy walls. These non-uniformities are caused by physical and geometric factors such as pipe placement, concrete properties, and soil interaction. Unlike simplified analyses, this study explicitly addressed how these temperature gradients lead to differential expansions and contractions across the wall cross-section. The simulations allowed detailed investigation into how localized temperature differences create internal thermal strains and stresses, thus challenging the assumption of uniform thermal loading often found in conventional approaches.

In addition, the study aimed to evaluate the influence of both mechanical and thermal boundary conditions on stress formation. Boundary conditions significantly impact how thermal stresses distribute within the wall. By systematically analyzing these boundary effects, the research identified the relationship between external constraints and internal stress patterns, providing essential insights for improved energy wall design practices.

Another objective was to examine how thermally induced stresses evolve over extended periods under continuous operational conditions. To achieve this, long-term simulations spanning 90 days were performed for both summer and winter scenarios. These analyses revealed the time-dependent nature of temperature and stress development, demonstrating that thermal stresses are not static but instead accumulate or redistribute over prolonged operational periods. The outcomes underscore the importance of considering the temporal evolution of stresses when designing energy walls, thereby promoting safer and more reliable structural solutions.

Moreover, the research highlights critical limitations in current simplified design methodologies that typically assume uniform or one-dimensional thermal input. Particularly, circumferential stresses, which have been frequently overlooked, can become significant, especially within the clear cover region between heat exchanger pipes and the surrounding soil. These results emphasize the need for adopting more detailed and realistic modeling approaches in the design and analysis of energy walls, challenging conventional assumptions and advocating for more comprehensive assessments.

Finally, although the thesis primarily focuses on numerical analyses, it also provides general recommendations for the practical design and operation of energy walls. Suggested strategies include the selection of improved concrete materials, operational temperature control, and balanced heat exchanger pipe configurations. While these suggestions were not directly tested within this numerical study, they are grounded in established engineering practices and relevant literature. Their practical effectiveness should be further validated through dedicated experimental investigations or detailed, project-specific evaluations.

In summary, this research offers enhanced insight into the complex structural behaviour of energy walls under thermal loading conditions. By systematically addressing non-uniform temperature distributions and their resulting stress patterns, the study contributes valuable knowledge that can guide the development of safer, more efficient, and more durable energy geostructure applications.

1.2. Dissertation Structure

This dissertation is structured into nine chapters, organized to guide the reader logically through the research, analysis, and findings related to thermally induced stresses in energy walls.

Chapter 2 (Literature Review) provides a detailed review of existing literature on energy geostructures, particularly energy piles and walls. It summarizes prior research, key methodologies, and significant findings on thermal stress behaviour, identifying gaps in current knowledge that this thesis aims to address.

Chapter 3 (Mechanism of Non-Uniform Thermal Stresses in Energy Walls) discusses in detail how non-uniform temperature distributions occur within energy walls and explores the underlying mechanisms leading to complex stress development. This chapter explains why these stresses cannot be adequately captured by simplified one-dimensional approaches, highlighting their importance for realistic structural analysis.

Chapter 4 (Validation of Energy Pile) focuses on validating the numerical approach by modeling a previously studied energy pile case that includes detailed stress data. This step was essential for testing the model's ability to capture non-uniform thermally induced stresses accurately. Although the main subject of the thesis is energy walls, the pile case provides a reliable reference for verifying stress behaviour before applying the method to wall simulations.

Chapter 5 (Validation of Energy Wall) presents the validation of thermal behaviour in the context of energy walls. This step confirms that the model can realistically capture the thermal response of the system, providing a reliable basis for the subsequent stress analysis.

Chapter 6 (Numerical Model) outlines the detailed methodology used in developing the three-dimensional numerical model with COMSOL Multiphysics. It describes the geometric setup, boundary conditions, material properties, and simulation parameters employed in analyzing energy wall behaviour under different thermal loading scenarios.

Chapter 7 (Results and Discussions) presents the outcomes of the numerical simulations, examining the development of thermally induced stresses under realistic, non-uniform temperature distributions. This chapter includes detailed analyses of stress patterns in all directions, and evaluates how these stresses evolve over time during both summer and winter scenarios.

Chapter 8 (Strategies to Minimize Thermally Induced Stresses) proposes several practical strategies aimed at reducing thermal stresses within energy walls. Although not directly tested in the current simulations, these recommendations highlight potential improvements in design, materials selection, operational temperature control, and pipe configuration, providing a foundation for future research and practical applications.

Chapter 9 (Conclusions) summarizes the key outcomes of the study, highlighting how the initial objectives were addressed through detailed numerical analyses. It emphasizes the importance of accounting for non-uniform temperature distributions and realistic boundary conditions when evaluating thermal stresses in energy walls.

2. LITERATURE REVIEW

2.1. Geothermal Energy

Geothermal energy is the thermal energy stored beneath the Earth's surface, originating from the planet's internal heat. This energy is primarily derived from three sources: the residual heat from Earth's formation, the continuous radioactive decay, and the absorption of solar radiation at shallow depths (Barbier, 2002).

Temperature within the Earth increases with depth, a phenomenon known as the geothermal gradient. In the top 8–10 meters, ground temperatures are influenced by atmospheric conditions and seasonal fluctuations. Beyond this depth, however, temperatures tend to remain stable year-round, reflecting the average annual surface temperature (Kalogirou and Florides, 2005). This thermal behaviour in the shallow subsurface is illustrated in Figure 2.1, which shows how temperature stabilizes below the depth influenced by seasonal variations.

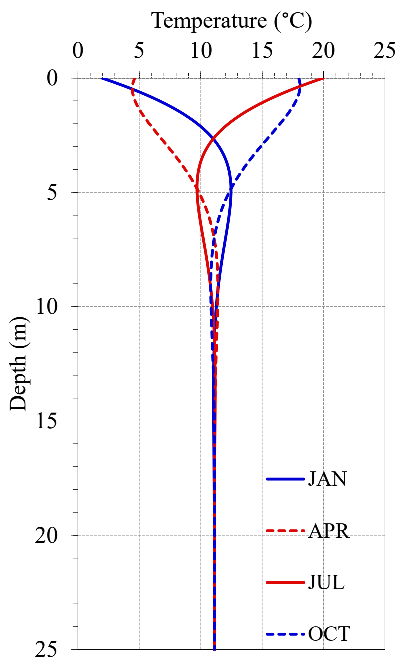

Figure 2.1. Seasonal temperature variation in shallow ground layers.

As depth increases further, the influence of surface conditions diminishes, and temperature begins to rise more steadily due to the Earth's internal heat. On average, geothermal gradients vary between 1°C and 3°C per 100 meters, depending on local geological and hydrogeological conditions (Barbier, 2002). A typical geothermal gradient profile is depicted in Figure 2.2, demonstrating the temperature-depth relationship in deeper ground layers.

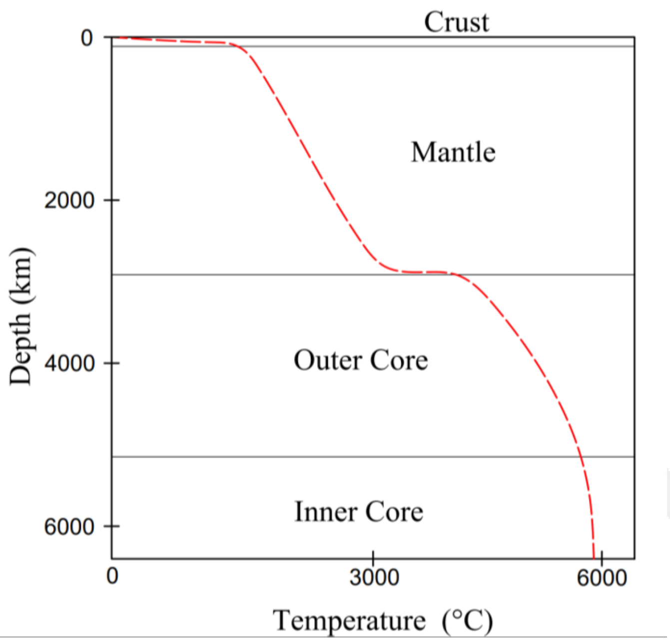

Figure 2.2. Typical geothermal gradient showing temperature increase with depth (Modified after Barbier, 2002).

Geothermal energy stands out as one of the most reliable and sustainable renewable energy resources. After solar energy, it is considered the second most abundant primary energy source globally. Unlike fossil fuels, its extraction and utilization involve no combustion, resulting in negligible greenhouse gas emissions. Furthermore, geothermal systems can provide continuous, base-load energy independently of weather or seasonal changes, offering a distinct advantage compared to solar and wind technologies that depend on environmental conditions (Lee et al., 2007). This inherent stability not only enhances long-term energy security but also contributes to reducing dependency on imported energy, making it a strategic component of sustainable energy policies worldwide.

2.2. Geothermal Systems

Geothermal systems are engineered solutions designed to extract and utilize the Earth’s internal heat. These systems are broadly categorized into two main types based on installation depth and thermal characteristics: shallow geothermal systems and deep geothermal systems.

Shallow geothermal systems typically operate at depths of less than 400 meters and are characterized by low-temperature and low-enthalpy heat exchange. These systems primarily serve heating, cooling, and domestic hot water needs, particularly in regions where subsurface temperatures remain below 25°C. Due to their relatively shallow installation depth, they are especially suitable for applications close to the ground surface and can be readily integrated into urban environments and buildings. In contrast, deep geothermal systems are installed at depths greater than 400 meters and tap into higher-temperature reservoirs, typically ranging from 25°C to over 200°C. Due to the elevated temperatures and enthalpy levels, deep systems are capable not only of meeting heating and hot water demands but also of generating electricity (Laloui and Rotta Loria, 2020).

Common configurations of shallow geothermal systems include horizontal geothermal boreholes, vertical boreholes, geothermal baskets, and energy geostructures such as energy piles, energy walls and energy tunnels. On the other hand, deep geothermal systems generally comprise technologies like thermal springs, hydrothermal systems, and petrothermal systems, which require specific geological conditions to be viable.

Regardless of their depth or configuration, all geothermal systems operate based on the same fundamental principle: the transfer of heat between the ground and the built environment through a circulating fluid. Each system consists of three primary components: a heat source, a heat sink, and a heat exchanger. The heat exchanger enables thermal energy to be transferred between the source and sink, usually via water or a water–antifreeze mixture in a closed-loop or open-loop piping system. In heating mode, heat is extracted from the ground and delivered to the building, making the ground the heat source and the building the heat sink. In cooling mode, this process is reversed: heat is removed from the building and discharged into the ground. In this case, the building acts as the heat source, while the ground serves as the heat sink.

2.3. Energy Geostructures

Among shallow geothermal systems, energy geostructures stand out as one of the most promising and widely implemented solutions in the construction industry. These systems utilize conventional subsurface structural elements (such as piles, diaphragm walls, tunnel linings, and barrettes) not only to provide structural support but also to facilitate thermal energy exchange with the surrounding ground. This dual functionality is made possible by embedding heat exchanger pipes into the reinforcement cages of these elements during construction (Brandl, 2006; Batini et al., 2015; Akrouch et al., 2020; Makasis and Narsilio, 2021; Lou et al., 2021; Laloui and Sutman, 2021). Once adapted for geothermal use, energy geostructures can contribute to a variety of applications, including space heating and cooling, domestic hot water production, snow and ice prevention on pavements and bridge decks, and seasonal underground thermal energy storage.

The embedded pipes—typically made of high-density polyethylene (HDPE)—form a closed-loop system that allows a heat transfer fluid, such as water or a water-antifreeze mixture, to circulate through the structure. Driven by electrically powered devices, the fluid absorbs or rejects heat depending on the operational mode, enabling efficient thermal interaction between the geostructure and the surrounding soil.

In most applications, energy geostructures are connected to a ground source heat pump (GSHP), which regulates the transfer of heat between the structure and the building. As shown in Figure 2.3, the system typically comprises two interconnected loops: a primary circuit, where the heat transfer fluid circulates through the geostructure and exchanges heat with the ground, and a secondary circuit, which delivers or removes heat from the indoor environment. The heat pump sits between these two circuits, adjusting temperatures as needed to optimize system performance.

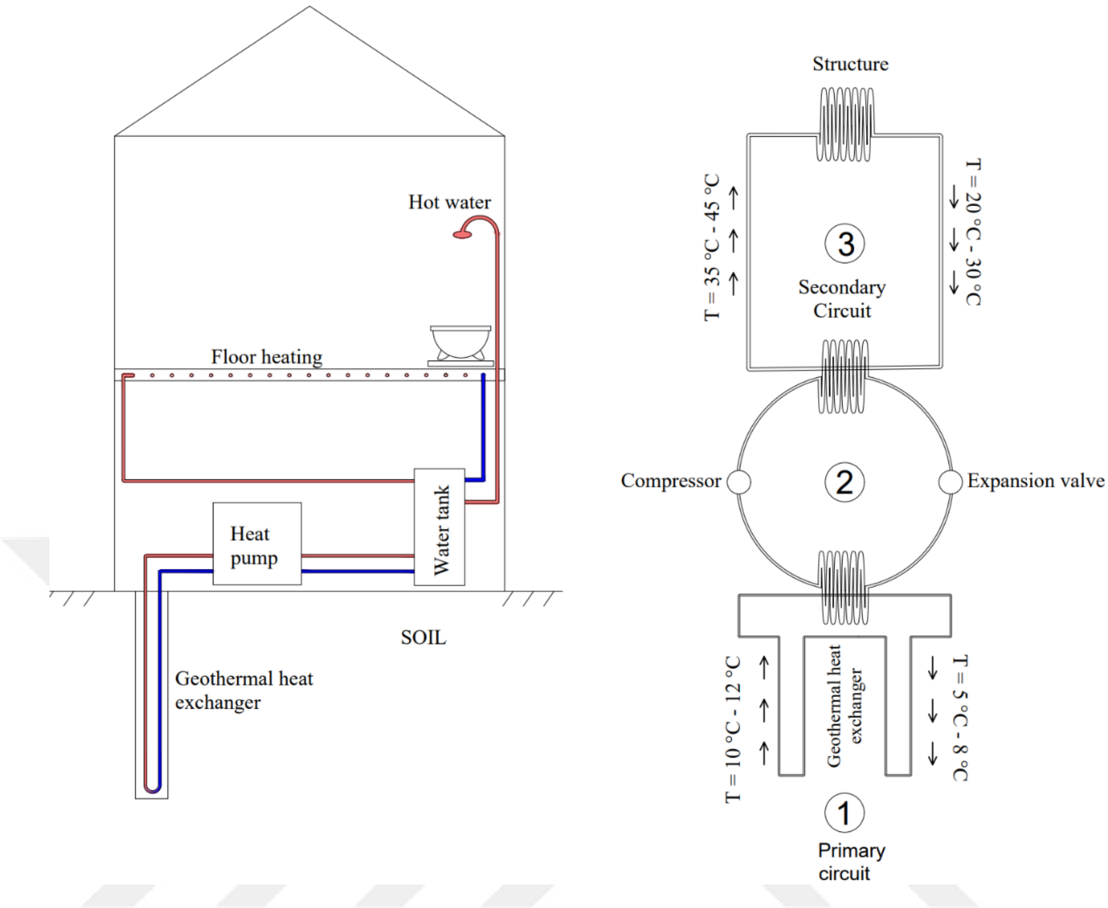

Figure 2.3. Functional layout of a ground source heat pump system used for building heating applications.

In cases where the system operates without a heat pump—relying only on a circulation pump to move fluid—the operation is known as free heating or free cooling, depending on the direction of heat flow. While this mode does not provide active temperature control, it allows for energy exchange when the thermal gradient between the ground and the building is naturally sufficient.

Because heat pumps require external electrical input, the overall efficiency of an energy geostructure system depends on how effectively it can convert this input into useful heating or cooling. This efficiency is typically measured using the coefficient of performance (COP), defined as the ratio of thermal energy output to the electrical energy consumed by the heat pump. A higher COP indicates a more efficient system. In well-designed installations, COP values for energy geostructures commonly range between 3.5 and 4.0 (Brandl, 2006), meaning the system delivers 3.5 to 4 units of heat or cooling for every unit of electricity used. This ratio is a key indicator of the energy savings potential and environmental benefit of geothermal systems integrated with structural foundations. The coefficient of performance can be calculated as

$$COP = \frac{Energy\ output\ after\ heat\ operation\ [kW]}{Energy\ input\ for\ heat\ pump\ operation\ [kW]}. \tag{2.1}$$

2.3.1. Energy Piles

Energy piles are among the most commonly implemented forms of energy geostructures, primarily due to their compatibility with conventional foundation systems. These elements function both as structural supports and as thermal energy exchangers. This dual role is achieved by embedding heat exchanger pipes into standard foundation piles during construction. As a result, the pile not only transfers building loads to the ground but also enables heat exchange between the structure and the subsurface (Brandl, 2006).

In bored piles, thermal pipes are typically fixed to the reinforcement cage, while in continuous flight auger (CFA) piles, the pipes are installed around a central steel bar positioned in the middle of the pile (Soga and Rui, 2016; Polat et al., 2025). These pipes are usually made of high-density polyethylene and can be arranged in various configurations, including U-shape, multi-U, W-shape, or spiral loops (Figure 2.4). The choice of configuration depends on design preferences, thermal load requirements, and pile geometry.

Before concrete is poured, the pipes are generally subjected to internal pressure testing. This step helps verify the integrity of the pipe system and prevents deformation due to concrete pressure during casting (Brandl, 2006). Once the system is in operation, the embedded pipes allow heat to be extracted from the ground and transferred to the building during winter. Conversely, during summer, excess heat from the building is rejected into the ground through the same system, allowing the pile to support cooling needs (Brandl, 2006; Laloui and Sutman, 2021).

Growing interest in the use of energy piles has led to a significant increase in research focusing on their thermal and structural behaviour. Many of these studies include both experimental investigations (Park et al., 2013; Polat et al., 2024; Faizal et al., 2025) and numerical simulations (Gashti et al., 2014; Sutman et al., 2020; Cecinato and Salciarini, 2022; Yang et al., 2025), aiming to assess the influence of various design and environmental factors on overall system efficiency. Parameters such as inlet fluid temperature (Hu et al., 2025), flow rate (Batini et al., 2015; Chen et al., 2023), pipe configuration (Zhao et al., 2016), local groundwater movement (Alqawasmeh et al., 2024; Yang et al., 2025), thermal properties of surrounding soils (Moradshahi et al., 2021) have all been found to significantly affect the heat transfer performance and long-term effectiveness of energy piles.

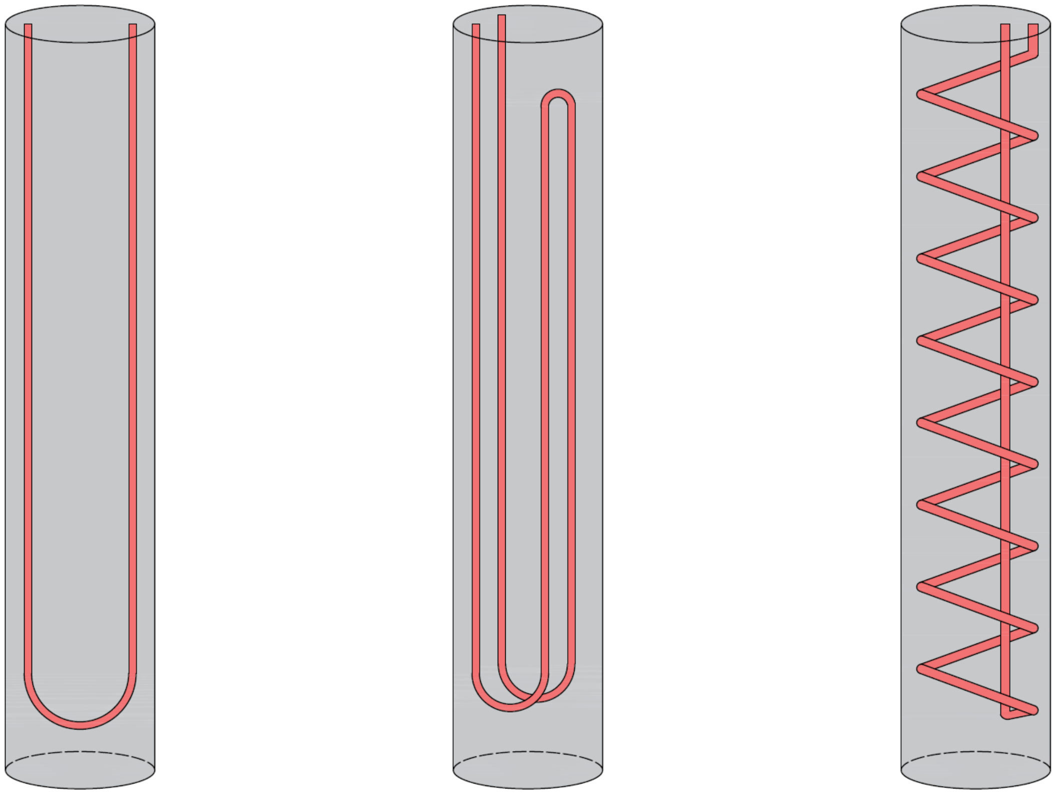

Figure 2.4. Schematic representation of U-shaped, W-shaped, and spiral pipe arrangements used within energy piles.

Beyond thermal performance, considerable attention has been given to the thermo-mechanical behaviour of energy piles—particularly the development of stresses and deformations caused by temperature fluctuations (Erginag et al., 2025). Both experimental tests (Sutman et al., 2019a; Fang et al., 2020) and computational models (Polat et al., 2025; Chen et al., 2025) have been employed to investigate axial and radial stresses resulting from thermal expansion and contraction. Studies focusing on axial stress development (Faizal et al., 2016; Sutman et al., 2019b; Polat et al., 2025) and radial strain distributions (Faizal et al., 2019; Moradshahi et al., 2021, 2022) have provided insights into how temperature variations influence internal force distributions within the pile.

Further physical modeling, particularly centrifuge testing, has been conducted to evaluate the impact of thermal cycles on the shaft friction and end-bearing resistance of piles (Stewart and McCartney, 2014; Ng et al., 2015, 2021; Vitali et al., 2022). These tests have helped simulate real-world conditions at reduced scale and revealed how thermal loads can alter geotechnical resistance mechanisms. Collectively, these experimental and numerical efforts have expanded our understanding of how energy piles behave under combined thermal and mechanical actions and support their optimization for long-term geothermal applications.

2.3.2. Energy Walls

Diaphragm walls are reinforced concrete retaining structures commonly used in deep excavation projects, particularly in urban environments where space constraints prevent the use of sloped excavations. Their primary purpose is to ensure the stability of surrounding soils and to prevent groundwater ingress into the excavation pit during construction. These walls can serve as temporary excavation support elements or remain as permanent basement walls after construction is completed. Especially in city-center excavations, diaphragm walls help protect adjacent structures from potential settlement or damage by providing rigid lateral support (Ou, 2006).

By embedding heat exchanger pipes into these structures, similar to the approach used in energy piles, diaphragm walls can be transformed into thermo-active energy walls. The first known application of such a system was constructed in Austria in 1996 (Brandl, 2006). As shown in Figure 2.5, these pipes are typically installed vertically or horizontally along the wall, depending on the structural layout and construction sequence (Makasis and Narsilio, 2020).

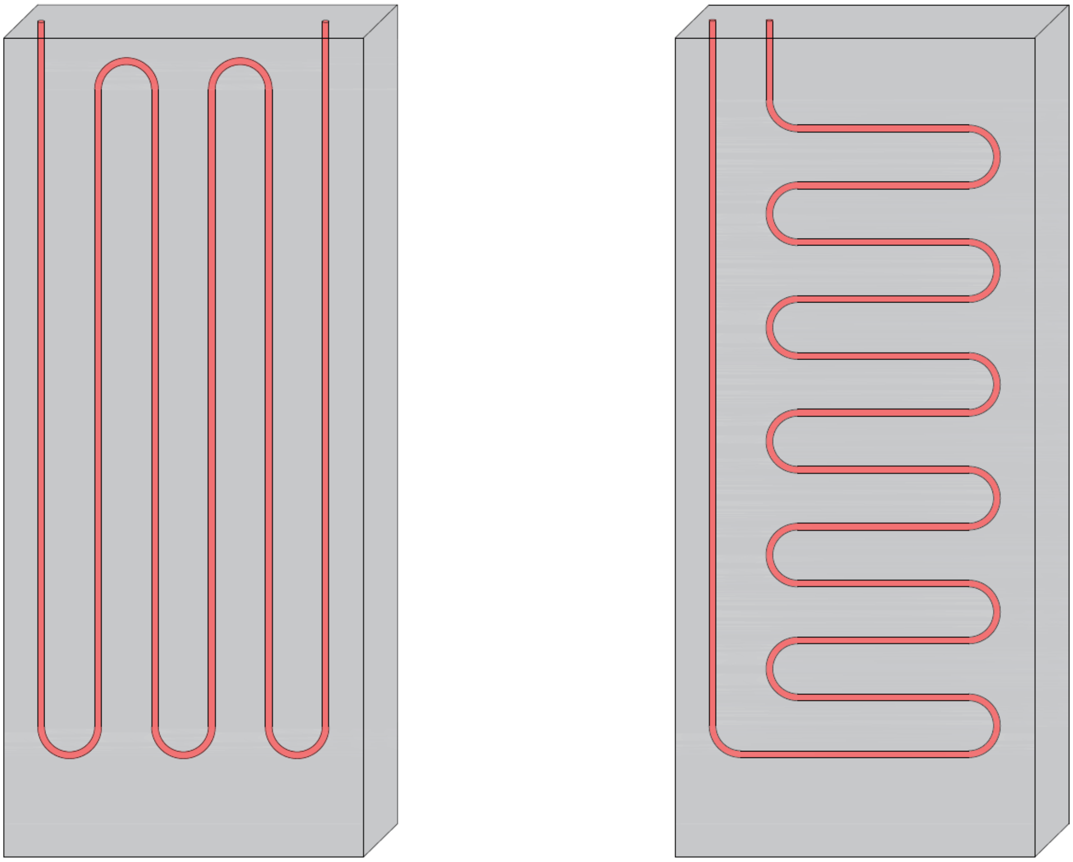

Figure 2.5. Common design practices for pipe layouts in energy walls.

One distinctive feature that sets energy walls apart from energy piles lies in their asymmetric boundary conditions, particularly in the upper portion exposed to the excavation. As illustrated in Figure 2.6, the upper segment of the wall typically has soil contact on one side and air on the other, while the lower segment remains surrounded by soil on both faces. This air–soil interface on the excavation side introduces a thermal discontinuity, significantly influencing the wall's heat transfer behaviour. Consequently, the excavation-side air exposure has become a focal point in recent research (Makasis et al., 2020; Dai et al., 2022; Ravera et al., 2024), especially for its impact on transient thermal performance and surface heat losses.

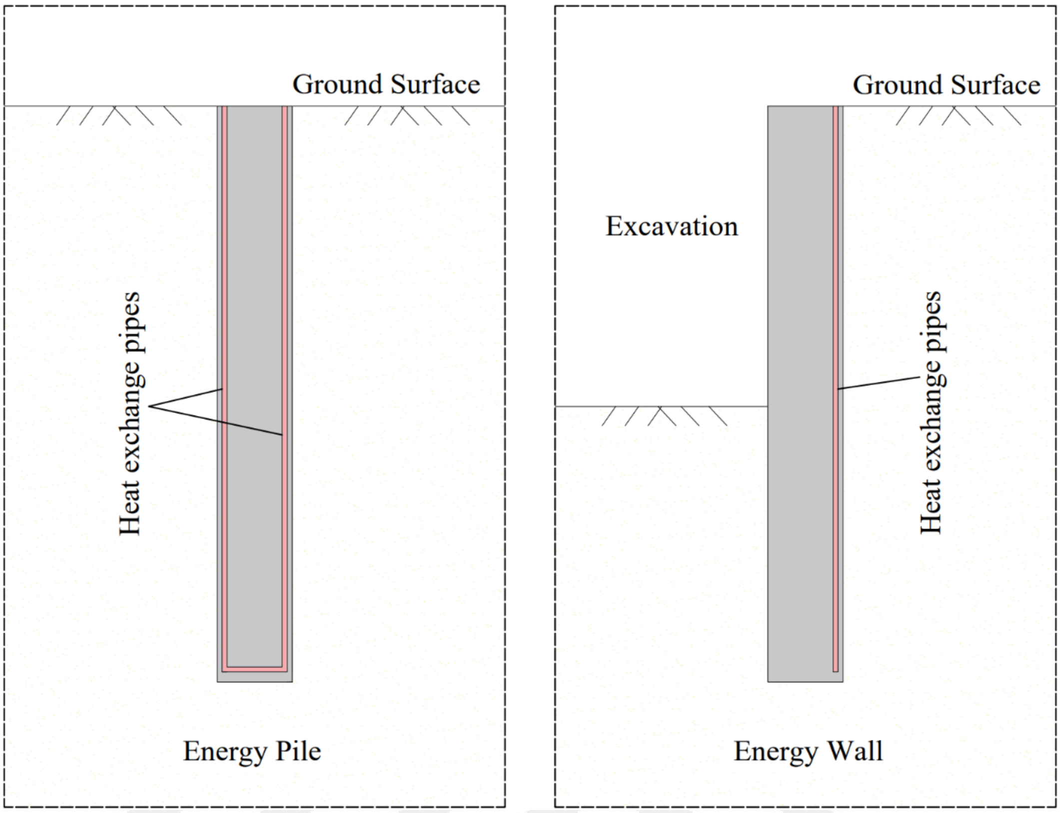

Figure 2.6. Cross-sectional view of a geothermal installation featuring an energy pile on the left and an energy wall on the right.

Beyond the boundary condition differences, numerous studies have investigated the thermal behaviour of energy walls, exploring the effects of several key parameters that influence heat exchange efficiency. These include inlet water temperature (Xia et al., 2012), pipe configuration (Sterpi et al., 2020; Makasis and Narsilio, 2020; Zhou et al., 2023), flow rate (Zeng et al., 2021; Chen et al., 2023), groundwater flow (Zannin et al., 2022; Mi et al., 2024), material properties (Di Donna et al., 2021; Bodas Freitas et al., 2024), and atmospheric conditions (Zhu et al., 2024). These studies have provided valuable insights for improving the energy efficiency and reliability of energy wall systems, contributing to better-informed design and operation practices.

In addition to thermal performance, recent research has also focused on the structural implications of cyclic thermal loading. In energy walls, thermally induced horizontal displacements, axial forces, shear forces, and bending moments have been investigated to assess the interaction between thermal and structural responses (Bourne-Webb et al., 2016;

Sterpi et al., 2017; Dai et al., 2022; Ravera et al., 2024). These findings are essential not only for ensuring the long-term stability of the wall but also for integrating energy systems into structural design without compromising safety or serviceability.

2.4. Thermo-Mechanical Behaviour of Energy Geostructures

Temperature fluctuations resulting from heat exchange processes between energy geostructures and the surrounding ground significantly influence their mechanical behaviour. Particularly in underground components such as energy piles and energy walls, thermal variations induce expansion and contraction, directly affecting their geometrical dimensions and interaction with the soil.

In a simplified scenario where a structural element is completely unconstrained, meaning it is free from mechanical loading or soil friction, it deforms purely due to temperature change. This deformation is referred to as free thermal strain and arises from the material's inherent tendency to expand when heated and contract when cooled. The magnitude of this strain depends on the applied temperature difference and the thermal expansion coefficient of the material. It can be calculated as

$$\varepsilon_{free} = \alpha\left(\mathrm{T} - T_{ref}\right), \quad (2.2)$$

where ε_{free} represents the free thermal strain, α is the material's thermal expansion coefficient, T is the applied temperature, and T_{ref} denotes the reference in-situ temperature. In such unconstrained conditions, deformation occurs without generating internal stress since there is no resistance to motion.

However, in practical engineering scenarios, energy piles are embedded within soil and typically subjected to loads from the structures they support. As a result, they cannot freely deform. Instead, the surrounding soil restricts their ability to expand or contract fully. Consequently, the strain actually observed (observed strain) is smaller than the theoretical free thermal strain, and this difference is referred to as blocked thermal strain. This relationship is expressed as

$$\varepsilon_{blocked} = \varepsilon_{free} - \varepsilon_{obs}. \quad (2.3)$$

This blocked strain generates internal stresses in the structure. These stresses, termed thermally induced stresses, are proportional to the blocked strain and depend on the Young's modulus of the structural element. They can be calculated as

$$\sigma_{th} = E \cdot \varepsilon_{blocked}, \tag{2.4}$$

where σ_{th} refers to the thermally induced axial stress, while E is the Young's modulus of the pile material.

In a fully unconstrained situation, a pile would deform freely in response to temperature changes, resulting in zero blocked strain and therefore no development of internal thermal stresses (Figure 2.7a). In contrast, if the pile is completely restrained at both ends, the deformation would be fully prevented, and thus the observed strain would become zero. Consequently, blocked strain equals the free thermal strain, causing significant thermal stresses to arise within the pile, as depicted in Figure 2.7b.

In practice, energy piles operate under conditions that lie between the two idealized extremes of fully free and fully restrained boundaries. These piles are typically subjected to mechanical loads from the superstructure, which significantly influence their thermo-mechanical response. The resulting behaviour largely depends on whether the pile's load-bearing capacity is governed primarily by shaft friction or end-bearing resistance.

For friction piles subjected to combined mechanical and thermal loads, heating generally causes differential vertical displacement along the pile length. Specifically, the upper segment tends to move upwards, whereas the lower segment moves downwards, creating a displacement profile that reaches a minimum near the pile's mid-depth. If the pile ends have sufficient flexibility, meaning the pile base rests on relatively soft material, and the superstructure moves freely as a rigid body, the thermal strain at both ends approaches the theoretical free thermal strain. Consequently, the largest thermal restraint, and thus minimal thermal expansion, occurs around the pile's mid-section. This restraint induces compressive axial stresses within the pile, and the rate of stress change along the pile length directly relates to the frictional resistance at the soil–pile interface. Near the pile's lower end, thermal movement occurs in the same direction as friction generated by mechanical loads, thereby increasing shaft friction. Conversely, near the pile's top end, thermal displacement opposes the mechanical friction direction, reducing overall frictional resistance. During cooling, the displacement profile reverses direction, potentially inducing tensile stresses at certain depths within the pile, an essential factor to assess carefully during structural design (Figure 2.8).

For end-bearing piles under mechanical loading, the response to heating differs significantly due to the presence of a rigid bearing layer beneath the pile tip. In this scenario, upward movement dominates the entire pile length, but displacement is notably limited at the pile base, constrained by the hard bearing stratum. As a result, thermally induced axial strains tend to increase progressively towards the pile top, whereas thermally induced compressive stresses become more pronounced with depth. This increased stress gradient implies a reduction in shaft friction along the pile, thus transferring a greater proportion of the load directly to the base. These elevated compressive stresses must be verified against structural design limits, such as concrete strength. During cooling, the response is reversed, enhancing frictional resistance along the shaft while decreasing the load concentration at the pile tip (Figure 2.9).

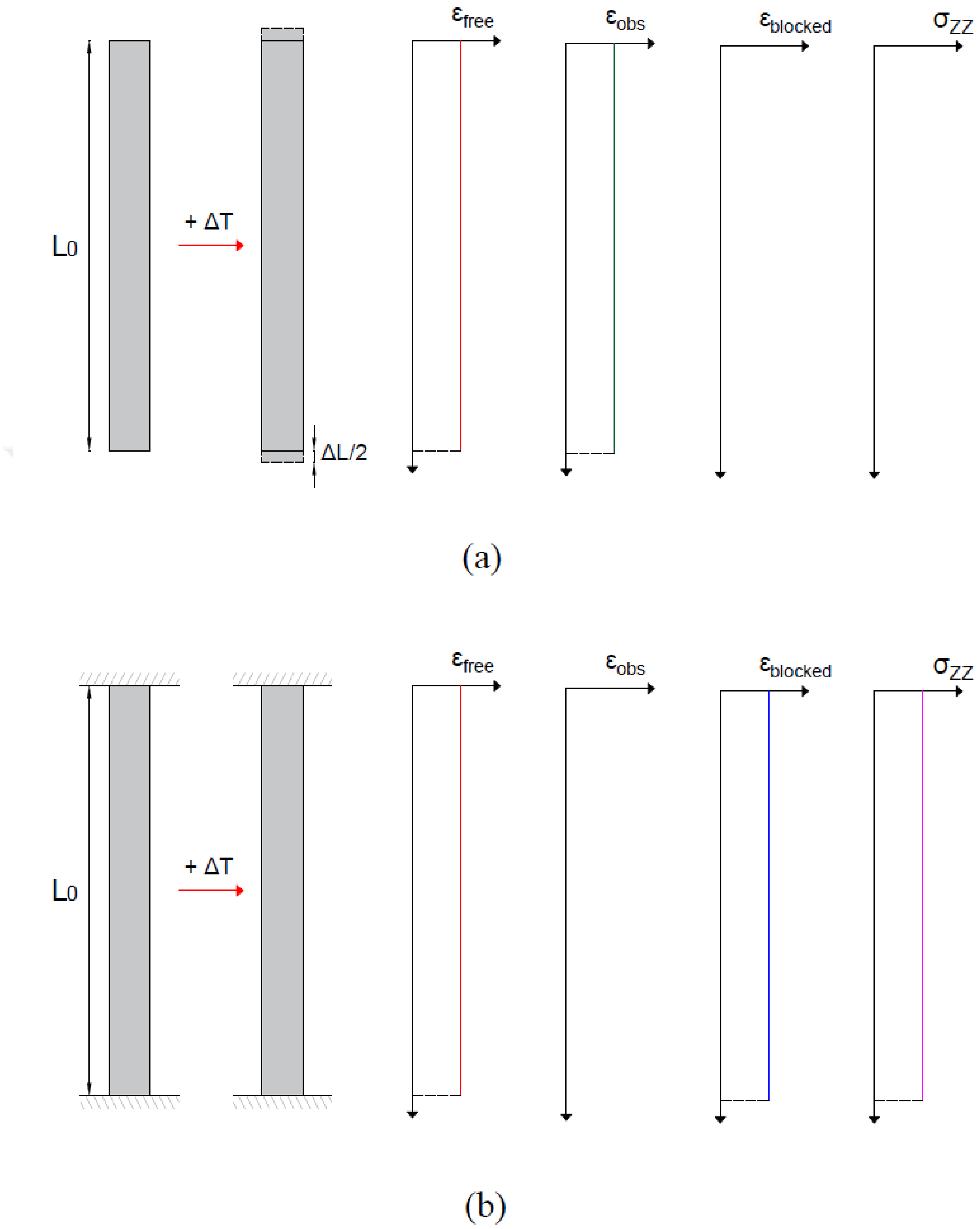

Figure 2.7. Thermally induced stress conditions for an energy pile under: (a) free deformation, (b) fully restrained deformation.

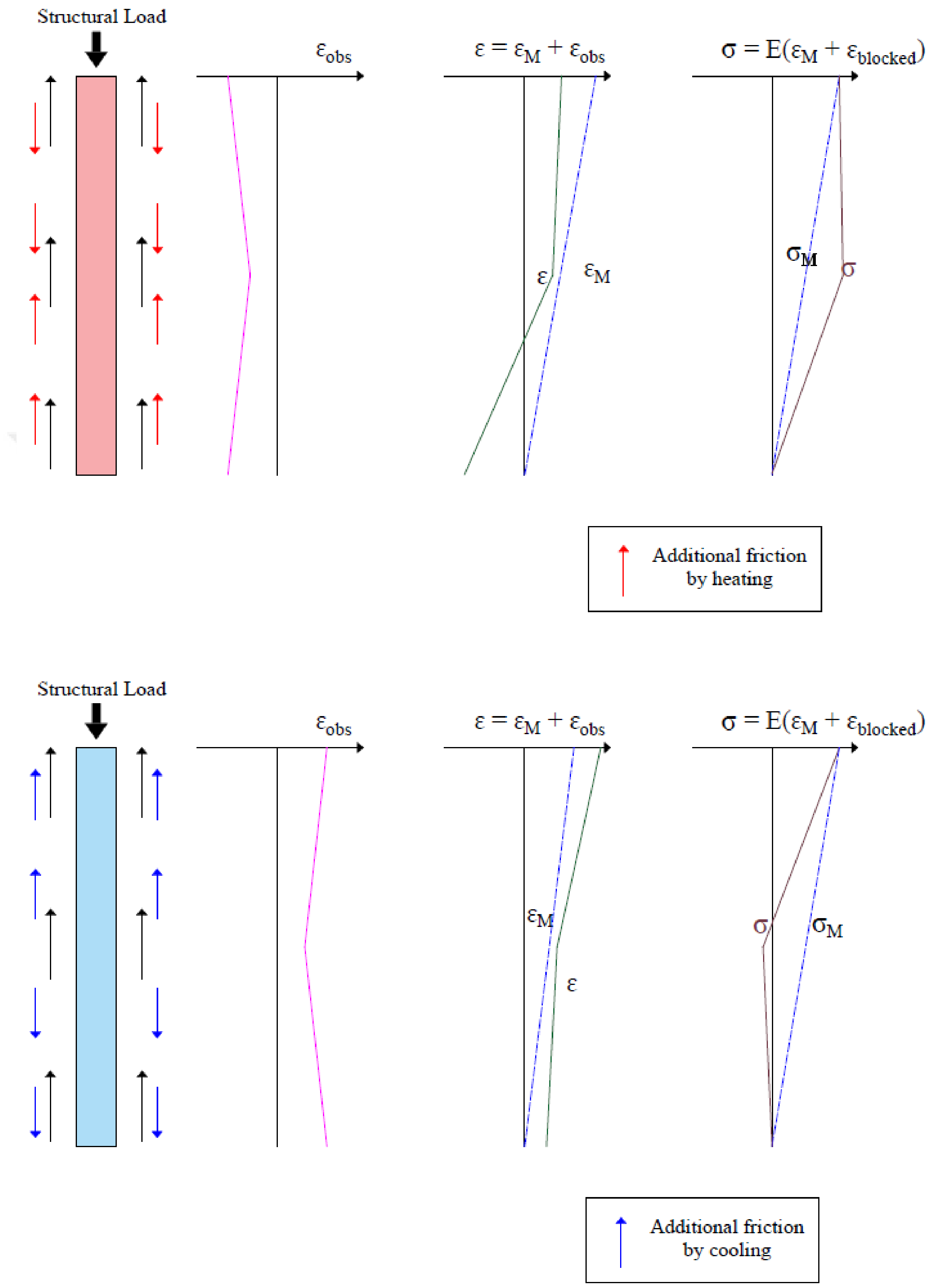

Figure 2.8. Thermo-mechanical behaviour of a friction pile under combined thermal and mechanical loads.

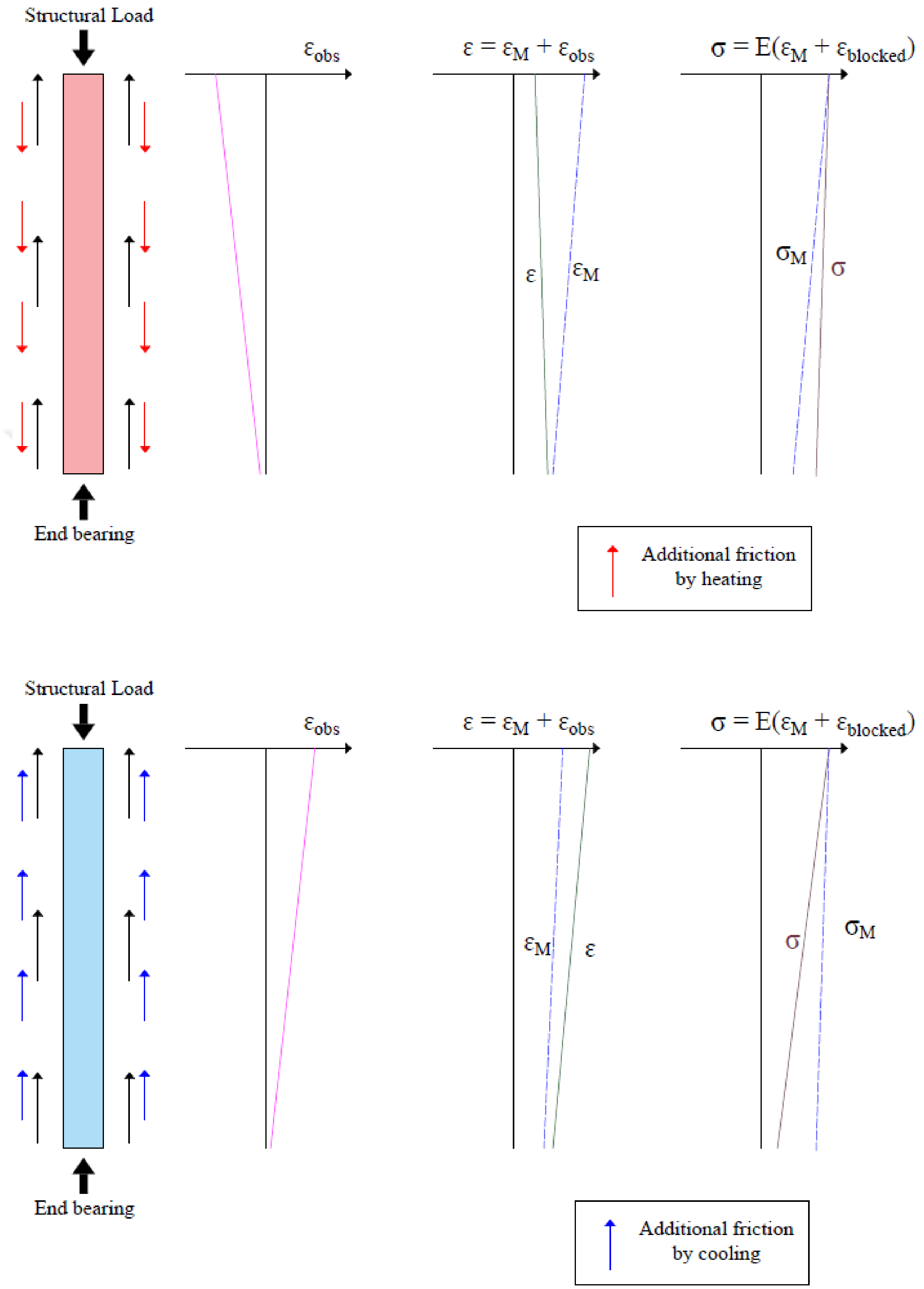

Figure 2.9. Thermo-mechanical behaviour of an end-bearing pile under combined thermal and mechanical loads.

2.4.1. Non-Uniform Thermally Induced Stresses

Energy piles are exposed to temperature fluctuations throughout their operation, resulting in non-uniform temperature distributions across the pile cross-section. These variations not only influence thermal strains and stresses in the axial direction but also lead to differential responses within the cross-sectional plane. Several studies have demonstrated that assuming a uniform temperature field can cause significant inaccuracies in estimating thermally induced strains and stresses. Consequently, non-uniform stress states have been investigated in the axial, radial, and circumferential directions, underscoring the need for multi-dimensional assessment in energy pile analysis (Abdelaziz and Ozudogru, 2016; Faizal et al., 2019; Moradshahi et al., 2021; Polat et al., 2025; Erginag et al., 2025).

To explore the axial dimension in detail, Abdelaziz and Ozudogru (2016) carried out 3D finite element simulations under both heating and cooling scenarios. Their results revealed that temperature gradients were more pronounced near the heat exchanger pipes, while the rest of the section experienced significantly lower temperature changes. As a result, differential expansion and contraction occurred simultaneously within a single cross-section—leading to non-uniform axial thermal strains. These strain patterns translated into the simultaneous development of compressive and tensile stresses, effectively challenging the traditional assumption of uniformly distributed axial behaviour. Their findings also emphasized that simplifying the thermal field as one-dimensional could lead to considerable errors, especially in reinforcement detailing and stress predictions.

Extending this understanding, Polat et al. (2025) also investigated the variation of axial thermal stresses across the pile cross-section using detailed numerical modeling. Their study highlighted that the accuracy of strain measurements depends heavily on sensor placement, as non-uniform stress distributions can lead to misinterpretation if instrumentation is not positioned carefully. This points to the practical importance of sensor layout in both field monitoring and validation of numerical models.

Supporting the numerical insights with field data, Faizal et al. (2019) conducted a full-scale experiment on a 10-meter-long, 0.6-meter-diameter energy pile installed beneath a six-story building. While the primary focus was on the pile's axial behaviour, their measurements also revealed non-uniform radial thermal responses across the cross-section. Although the magnitude of radial stresses was relatively small (remaining below –0.015 MPa) their presence confirmed localized differences in heat transfer and deformation. Meanwhile, axial thermal stresses reached values as high as –4.5 MPa, reaffirming their dominant role in the overall structural response. Even so, the presence of radial non-uniformities indicated localized differences in material behaviour around the pile perimeter, even if their magnitude was secondary.

Going a step further, Erginag et al. (2025) investigated the development of circumferential (hoop) stresses, which arise specifically from non-uniform temperature distributions across the pile section. Their numerical results showed that during heating, inner regions around the pipes expanded faster than the cooler outer concrete cover. This differential expansion generated hoop stresses, which varied in location and intensity depending on seasonal conditions. Notably, during summer months, these stresses approached the tensile strength of concrete near the pile perimeter—indicating a potential design concern. In winter, however, peak stresses shifted toward the inner zones. The study thus emphasized that circumferential effects, though often neglected, must be considered in design when non-uniform thermal loading is present.

3. MECHANISM OF NON-UNIFORM THERMAL STRESSES IN ENERGY WALLS

In order to enhance the understanding of thermal stress development within energy walls under conditions of non-uniform temperature distribution, a numerical simulation was carried out using the finite element software COMSOL Multiphysics. This analysis aims to illustrate a representative temperature distribution pattern and serves as a demonstrative case for the discussions presented in this section.

Figure 3.1 displays the cross-sectional temperature field of an energy wall subjected to a continuous heat injection scenario. Near the embedded thermal pipes (strategically positioned on the side of the wall in contact with the surrounding soil) the temperature contours initially form concentric, nearly circular patterns due to the localized nature of the thermal input. As the heat gradually diffuses toward the interior side of the wall, which faces the building, the initially circular thermal gradient evolves into a more elongated and linear configuration. This shift in temperature profile highlights the asymmetrical heat propagation behaviour resulting from the wall's geometry and boundary conditions.

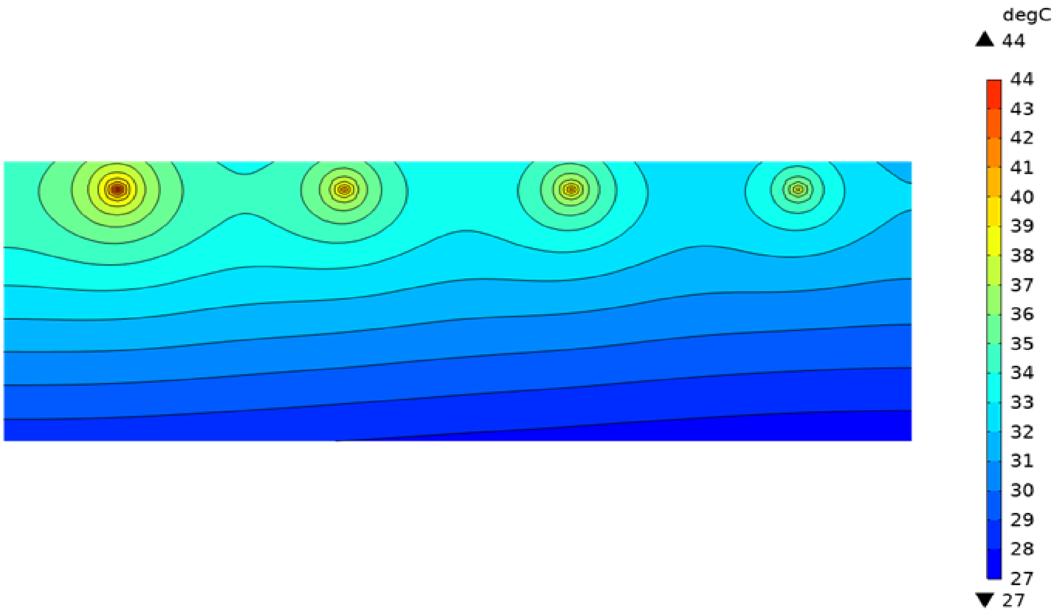

Figure 3.1. Cross-sectional temperature distribution of an energy wall under heat injection.

To investigate this thermal behaviour in greater detail, an idealized three-dimensional model illustrating the non-uniform temperature distribution within the energy wall is presented in Figure 3.2. This visualization forms the basis for evaluating the strain and stress responses that arise due to spatial temperature gradients within the structure. The temperature field depicted in Figures 3.1. and 3.2. allows for a clearer interpretation of how heat propagates through the wall volume under thermal loading

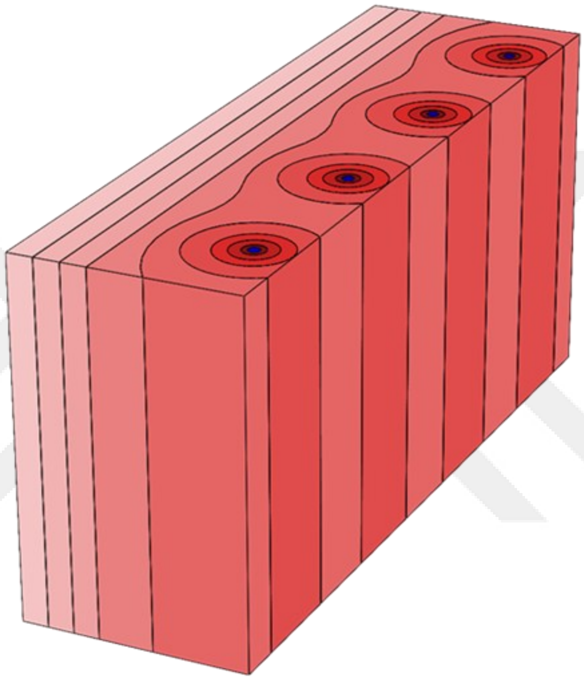

Figure 3.2. Idealized temperature distribution of an energy wall under heat injection.

Based on the observed distribution, the temperature field within the energy wall can be conceptually divided into three characteristic zones. Zone 1 refers to the immediate vicinity of the thermal pipes, where the temperature contours exhibit a predominantly circular pattern. Zone 2 constitutes the intermediate region between the soil and building sides of the wall. Within this zone, the initially circular temperature distribution progressively transforms into a more linear gradient. Zone 3, the region on the building side, characterized by a temperature distribution that becomes noticeably more linear.

In the following sections, detailed analyses will be carried out for Zones 1 and 3 to clarify how spatial variations in temperature fields contribute to the development of strain and stress within the energy wall structure.

3.1. Zone 1: Strains and Stresses Induced by Circular Temperature Distribution

The circular nature of the non-uniform temperature distribution observed in Zone 1 highlights the need for a detailed investigation into the strains and stresses developing in this region. Since this area surrounds the heat exchange pipes, the thermal gradients exhibit radial symmetry, making standard Cartesian coordinates insufficient to fully capture the mechanical response. To more accurately represent the deformation and stress patterns, a cylindrical coordinate system is adopted. This approach allows the stress and deformation to be examined in three principal directions: axial, radial, and circumferential (hoop). Such directional analysis provides a clearer understanding of the thermo-mechanical behaviour of the energy wall in the region most affected by localized heat input.

3.1.1. Axial Direction: Thermally Induced Strains and Stresses

To better illustrate how thermal loading affects strain and stress development in the axial direction, a conceptual schematic is provided in Figure 3.3a. This figure is based on a simplified and deliberately unrealistic heat injection scenario, designed to isolate the mechanical effects of temperature changes. In this illustration, each concentric cylindrical section is assumed to expand or contract independently in response to temperature, without being constrained by adjacent sections. While this assumption does not reflect actual structural behaviour, it allows for a clearer understanding of the mechanisms triggered by non-uniform temperature fields.

As seen in Figure 3.3a1, no deformation is present before the application of heat. Upon heating (Figure 3.3a2), thermal expansion occurs, with the amount of axial elongation varying across the wall's cross-section. The innermost cylinder (K), exposed to the highest temperature increase, undergoes the most significant elongation, whereas the outermost cylinder (M) shows minimal axial expansion. In this scenario, free thermal strain reaches its peak in cylinder K and is smallest in cylinder M.

In reality, however, the energy wall acts as a continuous structure, and free expansion of individual sections is not possible. As a result, the thermal expansion in the hotter inner zones (e.g., cylinder K) is partially restrained by the surrounding material. This constraint leads to compressive stresses in the inner region, while the outer regions—depending on the magnitude of vertical loading and interaction with surrounding soil—may experience lower compression or even tensile stresses (Figure 3.3a3).

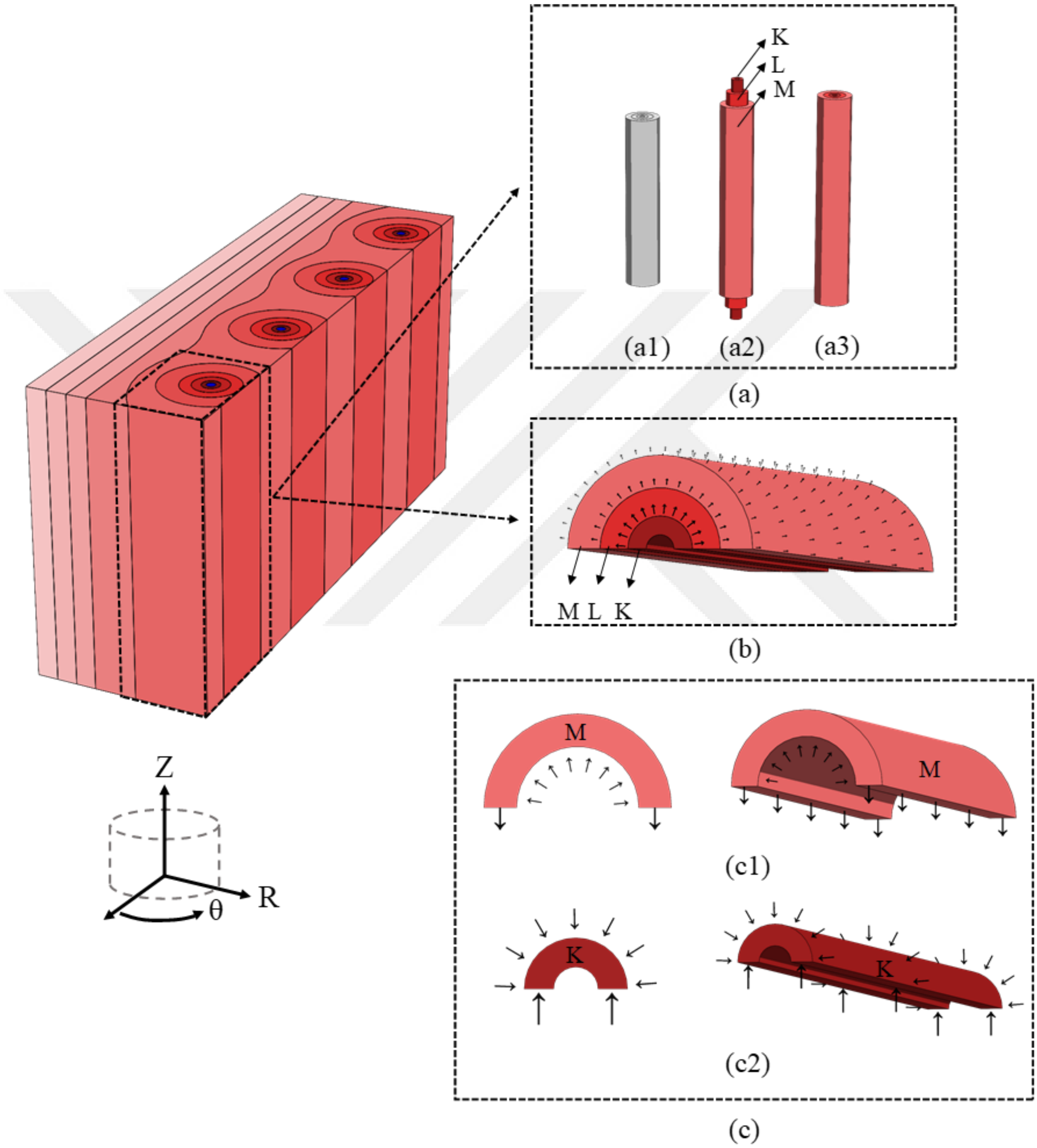

Figure 3.3. Zone 1- displacement and stresses, (a) axial displacement, (b) radial displacement, (c) thermally induced stresses at circumferential direction.

Figure 3.4 illustrates a typical axial thermal stress distribution in Zone 1 during the heat injection phase, assuming structural continuity across the section. In particular, Figure

3.4a highlights how the imposed temperature gradient influences both the magnitude and spatial variation of axial stresses. These stress profiles are intended to serve as representative examples of thermal stresses typically develop under the defined boundary and loading conditions.

3.1.2. Radial Direction: Thermally Induced Strains and Stresses

A similar stress development mechanism takes place in the radial direction, as shown in Figure 3.3b. In a hypothetical case without constraints, where the outer cylinders do not resist the outward expansion of the inner ones, the innermost cylinder (K) would exhibit the highest free radial strain, while the outermost cylinder (M) would show the lowest. These differences in radial strain correspond directly to the variation in temperature experienced by each section.

In practice, however, the structural continuity of the energy wall prevents such free expansion. The inner, hotter cylinders are partially restrained by the surrounding, cooler outer layers. This constraint leads to a progressive decrease in blocked strain from the inner to the outer cylinders, K being the most restricted and M the least. At the outer edge, cylinder M is primarily influenced by the pressure exerted by the surrounding soil at the soil-structure interface. As a result, notable radial compressive stresses develop in the inner zone (K), which gradually reduce toward the exterior, where M undergoes compression mostly due to soil confinement. A conceptual representation of the resulting radial stress distribution, from K to the soil boundary, is provided in Figure 3.4b.

3.1.3. Circumferential (Hoop) Direction: Thermally Induced Stresses

Circumferential (hoop) stresses develop as a result of the circular temperature distribution and the uneven thermal expansion between the inner and outer regions of the energy wall (Figure 3.3c). Similar to the radial direction, the highest thermal expansion occurs in the innermost cylinder (K), while the outermost cylinder (M) experiences the least. This non-uniform expansion is constrained by the cooler, outer regions, particularly M, which limits the outward movement of the warmer inner sections. As a result, compressive circumferential stresses form in K due to the inward resistance imposed by the surrounding material (Figure 3.3c2).

In contrast, the outermost cylinder (M), although undergoing minimal thermal expansion itself, is subjected to outward forces transmitted from the expanding inner zones. This leads to the development of tensile hoop stress in M (Figure 3.3c1). It is important to note that these circumferential stresses are primarily driven by thermal expansion and internal restraint mechanisms, rather than by externally applied vertical loads.

The circumferential stress distribution, starting with maximum compression at K and transitioning to maximum tension at M. This profile is conceptually depicted in Figure 3.4c, demonstrating how thermally induced deformation patterns translate into hoop stress development across the section.

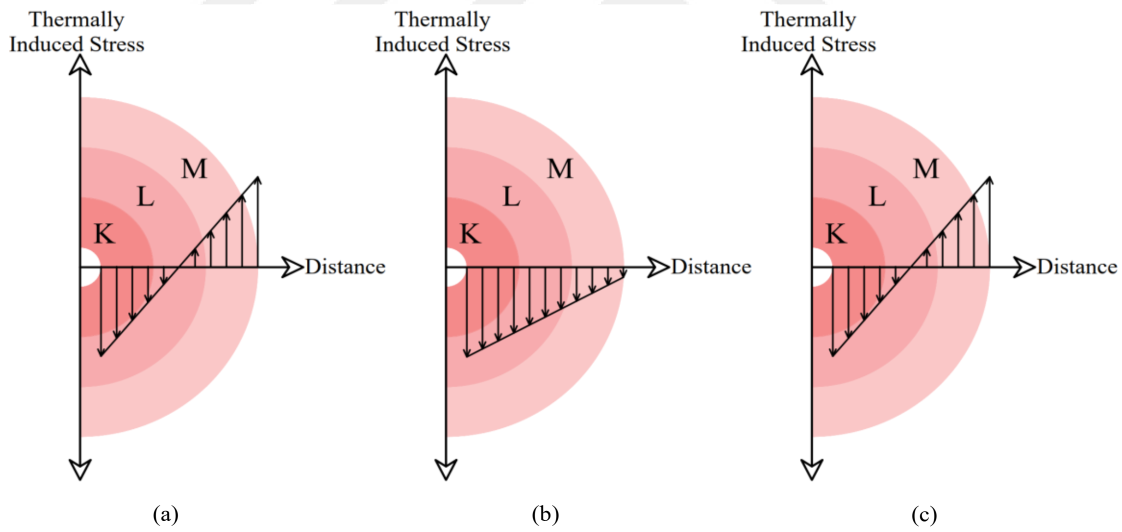

Figure 3.4. Radial distribution of thermal stresses induced by the thermal pipe during heat injection, with radial distance measured from the pipe: (a) axial stresses, (b) radial stresses, and (c) circumferential (hoop) stresses.

3.2. Zone 3: Strains and Stresses Induced by Linear Temperature Distribution

In Zone 3, the non-uniform temperature field follows a linear gradient, which requires a different analytical approach compared to the circular distribution observed in Zone 1.

While cylindrical coordinates are suitable for analyzing radial symmetry, the thermal and mechanical responses in this zone are more effectively evaluated using a Cartesian coordinate system. This coordinate framework allows the deformation and stress components to be assessed independently along the X, Y, and Z axes. In this study, the Cartesian axes are defined such that the X-axis is perpendicular to the wall, pointing from the soil side, where the thermal pipes are embedded, toward the building side; the Y-axis runs along the longitudinal direction of the wall; and the Z-axis represents the vertical direction.

To clarify how this linear temperature gradient leads to strain and stress development, an idealized conceptual model is introduced in Figure 3.5. Similar to the approach used for Zone 1 (Figure 3.3), this model assumes that adjacent regions do not restrict each other's deformation. Although this assumption does not reflect real boundary conditions, it serves to illustrate the fundamental mechanical processes caused by differential thermal expansion. As shown in Figure 3.5a, no deformation is present prior to thermal loading. Once heating begins, different regions expand to different extents, depending on the temperature they experience (Figure 3.5b). In particular, the region closest to the heat source (prism T) undergoes the most significant expansion in all three spatial directions, while the region farthest from the source (prism P) exhibits the least. Free strain is therefore highest in T and lowest in P, directly corresponding to the temperature gradient across the wall section.

However, due to the structural continuity of the energy wall, the different regions cannot expand independently. Instead, they are forced to accommodate each other's movement, resulting in constrained deformation (Figure 3.5c). These internal constraints generate blocked strains, which give rise to thermally induced stresses within the wall. This stress development is an important outcome of the mechanical interaction between regions subjected to varying thermal expansion.

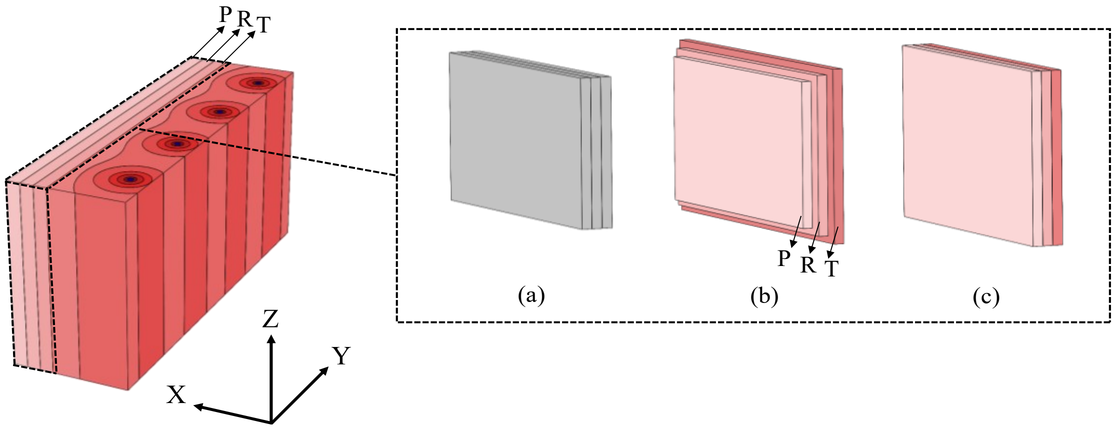

Figure 3.5. Conceptual illustration of thermal interactions and the resulting mechanical behaviour within the sections of Zone 3.

3.2.1. X Direction: Expansion and Thermal Stress Formation

In the X direction, thermal expansion leads to mechanical interaction between neighboring regions (P, R, and T, as shown in Figure 3.5b). Although the free thermal strain differs from one region to another due to the temperature gradient, the blocked strain remains constant along the X-axis, owing to the continuous mechanical connection between these regions.

If the energy wall is not restrained on the building side, thermal expansion in the X direction can occur without resistance. Under such conditions, no blocked strain or thermal stress develops, as illustrated in Figure 3.6a. However, if expansion is restricted at the building side, this constraint limits free movement along the X direction and leads to the development of compressive thermal stresses. Since mechanical interaction is continuous across the X-axis, all regions (from block T to block P) experience the same level of blocked strain, resulting in a uniform compressive stress throughout.

3.2.2. Y-Direction: Lateral Constraint Effects

Due to the considerable width of the energy wall, movement along the Y direction is generally restricted by adjacent structural components or contact with the surrounding soil. This constraint prevents any elongation in the Y-axis, causing all free thermal strains to be converted into blocked strains. As a result, compressive stresses develop along the Y direction. Since free strain varies with temperature, the blocked strain is larger in hotter regions such as prism T and smaller in cooler regions like prism P. This distribution is illustrated in Figure 3.6b. The overall magnitude of these stresses depends on the extent of lateral constraint applied to the wall's side surfaces.

3.2.3. Z Direction: Expansion and Thermal Stress Formation

In the Z direction, the presence of a temperature gradient causes prism T to undergo greater vertical expansion compared to prisms R and P. However, due to the structural continuity of the energy wall, this expansion cannot occur independently; instead, the entire system deforms in a coordinated manner. This interaction results in compressive stresses forming in the hotter region (prism T), with the stress gradually reducing toward the cooler region (prism P), as shown in Figure 3.6c.

If vertical movement is fully restricted, compressive stresses are maintained in all regions of the energy wall. However, if the wall is allowed to deform vertically (for example, if the top surface is free to move) then the stress state may change. In such a case, while compressive stresses still occur in prism T due to higher thermal expansion, tensile stresses may develop in prism P, where thermal expansion is smaller.

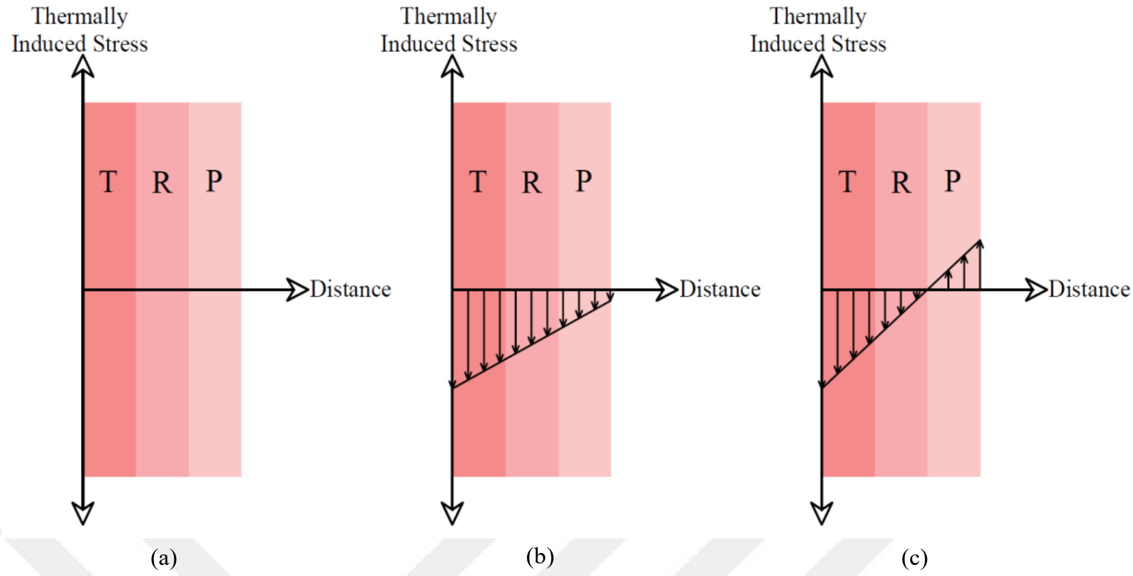

Figure 3.6. Expected thermal induced stresses within Zone 3: (a) X-direction, (b) Y-direction, and (c) Z-direction.

4. VALIDATION OF ENERGY PILE

To investigate and validate the thermo mechanical behaviour of energy geostructures through numerical modelling, a full-scale field test of an energy pile (Sutman, 2016) was selected as a benchmark. This test, conducted on a 15.24 m long and 45.7 cm diameter energy pile in Houston, Texas, involved axial stress measurements under thermal loading conditions. The field test results served as reference data for the numerical simulations developed in this study using COMSOL Multiphysics (Polat et al., 2025), which are presented in this chapter.

4.1. Field Test

The field test reported by Sutman (2016) was carried out at a site in Houston, Texas. Based on a series of in-situ and laboratory investigations conducted at the site (Brettmann and Amis, 2011; Sutman, 2016; Sutman et al., 2019a), the subsurface profile consists of three primary soil units: clay layers located above and below the groundwater table, underlain by a sand layer. The groundwater table was observed at a depth of approximately 3.7 m.

The test energy pile was constructed using the continuous flight auger (CFA) method and has a diameter of 45.7 cm and a length of 15.24 m. It is equipped with a single U-shaped polyethylene (PEX) heat exchanger pipe, with a nominal diameter of 25.4 mm and a wall thickness of 3.2 mm. Due to construction variability, the spacing between the legs of the U-pipe varies slightly along the pile length, averaging around 6.4 cm. The circulating fluid used for heat exchange consisted of 80% water and 20% ethylene glycol by volume. Thermal and mechanical properties of the soil layers and pile materials, used in the numerical modelling, are summarized in Table 4.1.

To monitor the thermal and mechanical response of the pile, two vibrating wire strain gauges were installed at five different depths along its length. The instrumentation layout is illustrated in Figure 4.1. Although the figure presents an idealised cross-sectional view, the exact positions of the sensors within the pile cross-section remain uncertain due to construction variability, particularly considering that the pile was constructed using the Continuous Flight Auger (CFA) method. As noted by Sutman et al. (2019a), the sensors were attached to the vertical reinforcement bars; however, their precise radial locations are likely to vary along the pile height.

Based on multiple trials accounting for the diameter and spacing of the reinforcement, as well as typical construction practices, it is estimated that the strain gauges are located at radial distances ranging from 11.7 cm to 12.9 cm from the centre of the pile. In the numerical model, these two radial positions (R = 11.7 cm and R = 12.9 cm) are used as the bounds for possible sensor placement. Accordingly, temperature and stress results are extracted at both locations to capture the response envelope and enable comparison with the field measurements.

Table 4.1. Thermal and mechanical properties of soil layers, pile and pipes.

Properties	**Symbol**	**Unit**	**Clay**	**Sand**	**Pile**	**PEX pipes**
Young's modulus	*E*	MPa	45	75	36000	-
Poisson's ratio	*ν*	-	0.495	0.30	0.18	
Unit weight	*γ*	kN/m^3	2005	1986	2044	-
Volumetric heat capacity	*C*	MJ/m^3°C	2.61	2.61	1.80	-
Thermal conductivity	*λ*	W/m°C	2.1	1	2	0.42
Thermal expansion coefficient	*α*	με/°C	1.5	1	12.9	-

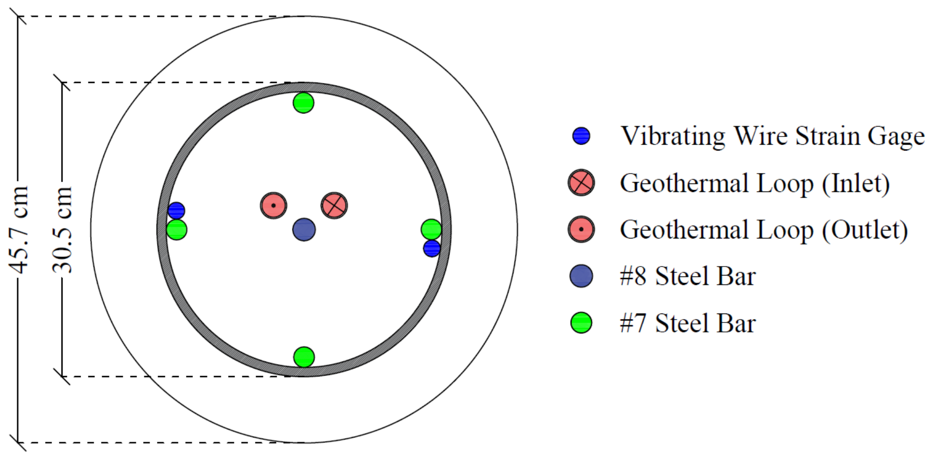

Figure 4.1. Cross-sectional layout of the sensors within the pile (modified after Sutman et al., 2019a).

During the field experiment, the energy pile was exposed to five cycles of thermal loading without any accompanying mechanical load. Each cycle involved a ±10 °C variation in the temperature of the circulating fluid, ranging between 8 °C and 43 °C. For the purposes of model validation, only the first thermal cycle and its associated measurements were considered in this study. The thermal loading profile for this initial cycle is shown in Figure 4.2.

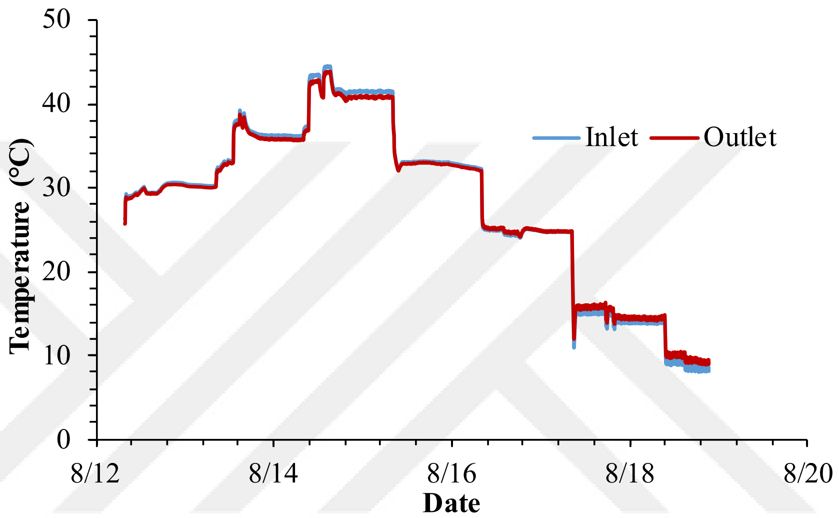

Figure 4.2. Thermal loads applied to the pile (modified after Sutman et al., 2019a).

4.2. Model Geometry

The numerical model was developed based on the stratigraphy identified during field investigations and corresponding laboratory test results. The subsurface profile consists of three distinct soil layers: clay above and below the groundwater table, underlain by a sand layer. At the centre of the model domain, an energy pile with identical geometric dimensions to the test pile (15.24 m length, 45.7 cm diameter) was positioned to minimise boundary effects.

To improve computational efficiency, the embedded U-shaped pipes within the pile were modelled as line elements. Their thermal properties and fluid flow parameters were subsequently defined using the Heat Transfer in Pipes module. The overall model domain extends 50 m × 50 m laterally and 40 m in depth, as illustrated in Figure 4.3.

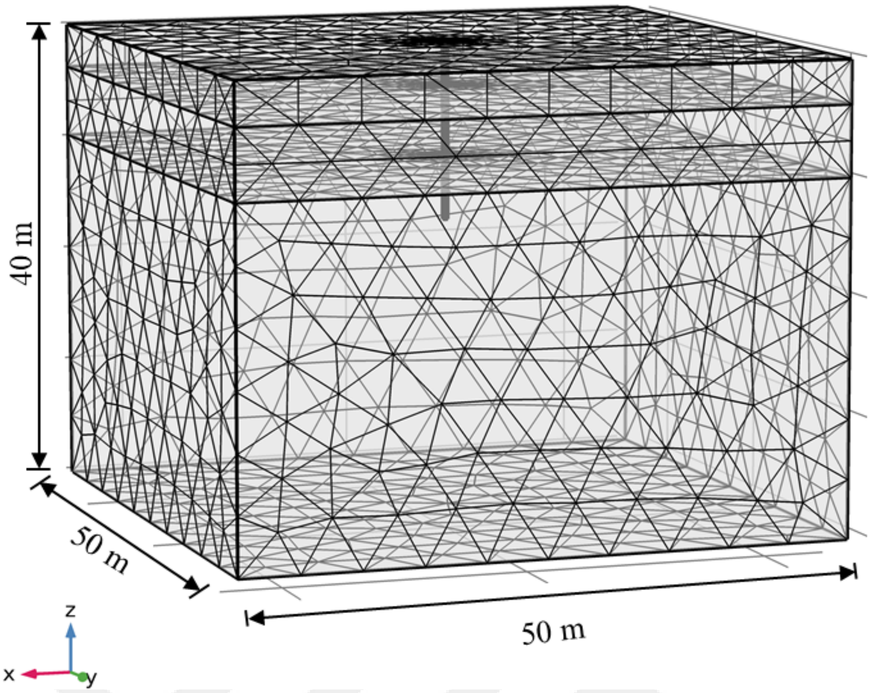

Figure 4.3. 3D view of the model.

4.3. Assumptions and Boundary Conditions

The soil and the pile were modelled as a porous medium. A linear elastic material model was assigned to the pile, while the soil behaviour was represented using the Mohr-Coulomb constitutive model. The interface between the soil and pile was assumed to be fully bonded; no separate interface elements were introduced. Material properties used in the model are summarised in Table 4.1, and it was assumed that these properties remain constant and are not affected by temperature variations.

For the mechanical boundary conditions, the bottom boundary of the model was fixed in all directions, while the lateral boundaries were constrained to prevent horizontal movement (roller boundaries). The top surface was left free. The soil domain was assumed to be in geostatic equilibrium under self-weight, whereas the pile was subjected to an isotropic stress state.

Regarding thermal boundaries, the initial temperature of the system was set to 21.6 °C, in accordance with field measurements taken prior to thermal loading. Adiabatic conditions were applied to the side and bottom boundaries to prevent external heat exchange. At the top boundary, heat flux was applied to simulate the influence of atmospheric conditions, based on weather data obtained from the nearest meteorological station, William P. Hobby (ASHRAE, 2013). Thermal loading was introduced through the inlet temperature of the circulating fluid, as shown in Figure 4.2.

4.4. Comparison of Results

To assess the accuracy of the numerical model in predicting thermally induced stresses, simulation results were compared with the experimental data reported by Sutman (2016). This comparison focused on the temperature evolution and axial thermal stresses during the first three days of thermal loading. As illustrated in Figures 4.4 to 4.6, the simulated results closely align with the measured temperatures and calculated axial stresses, demonstrating that the model reliably captures the thermomechanical behaviour of the system.

In particular, the temperature profiles obtained from the simulation match the measured data at multiple depths and time intervals, with deviations remaining within an acceptable range of ±1°C. This close agreement suggests that the model accurately replicates the transient heat transfer processes within the pile and surrounding soil, which is crucial for capturing the associated stress responses.

A more detailed evaluation was performed by considering the estimated radial positions of the strain gauges. As shown in Figures 4.4 to 4.6, the simulated axial thermal stresses at radial position R = 12.9 cm exhibited good agreement with the field measurements at all instrumented depths, with an error of less than 14%, except at the 8.7 m depth. At this depth, the numerical results corresponding to R = 11.7 cm were found to be more consistent with the experimental data.

This discrepancy is likely due to uncertainty in the precise radial location of the sensor at that particular depth. Given the construction method (CFA) and potential variability in sensor placement, it is plausible that the sensor at 8.7 m was positioned slightly closer to the pile centre than those at other depths. To support this interpretation, Figure 4.7 presents the distribution of thermally induced axial stress across the pile cross-section at the 8.7 m depth. As shown, the stress gradient increases significantly toward the pile centre, indicating that even small variations in radial sensor placement can result in substantial differences in measured stress values.

Overall, the close agreement between the numerical and experimental results—despite local variability—indicates that the developed model is capable of accurately simulating the thermal behaviour and stress development in energy piles.

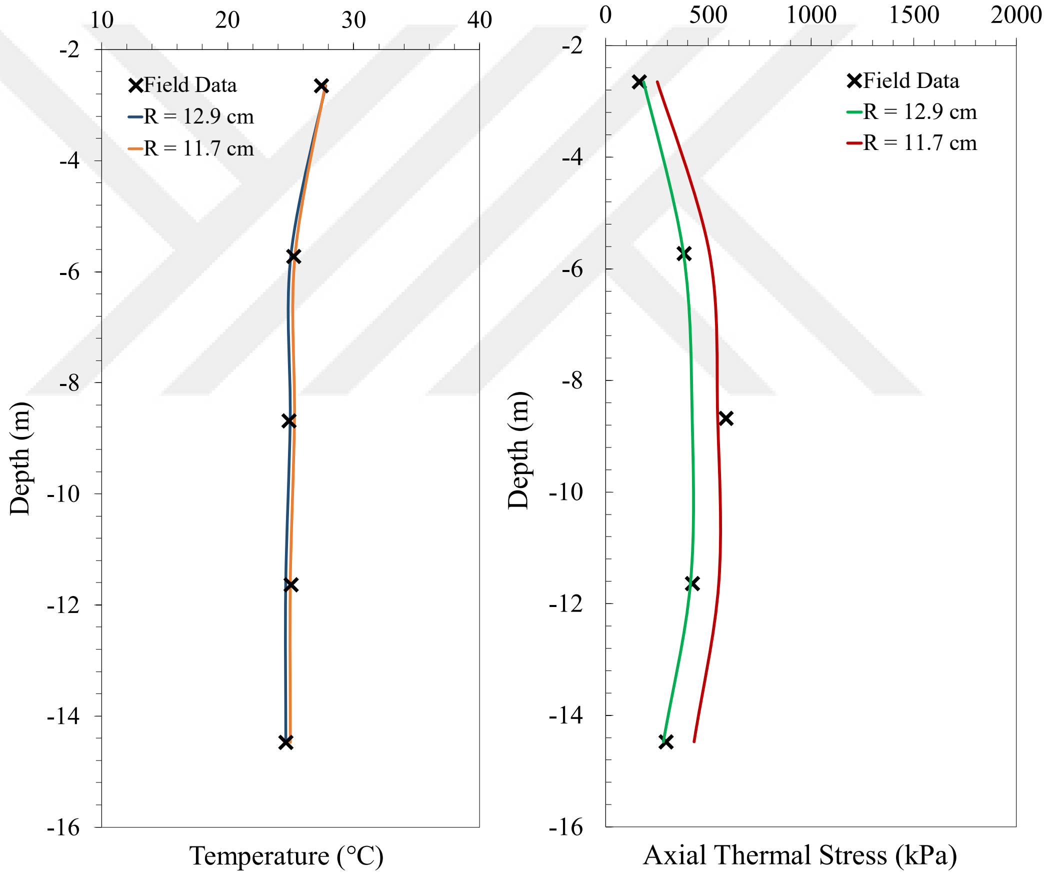

Figure 4.4. Comparison of temperatures and stresses along the pile between the field data and numerical simulation for Day-1.

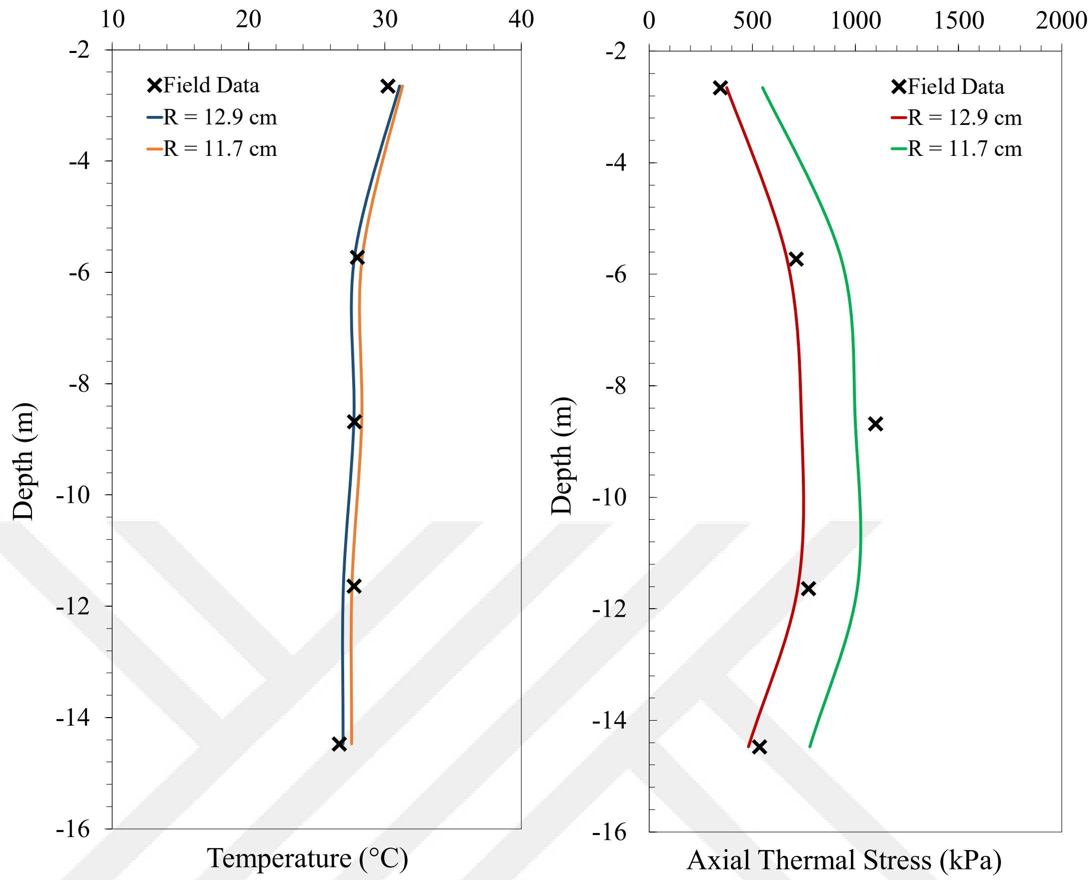

Figure 4.5. Comparison of temperatures and stresses along the pile between the field data and numerical simulation for Day-2.

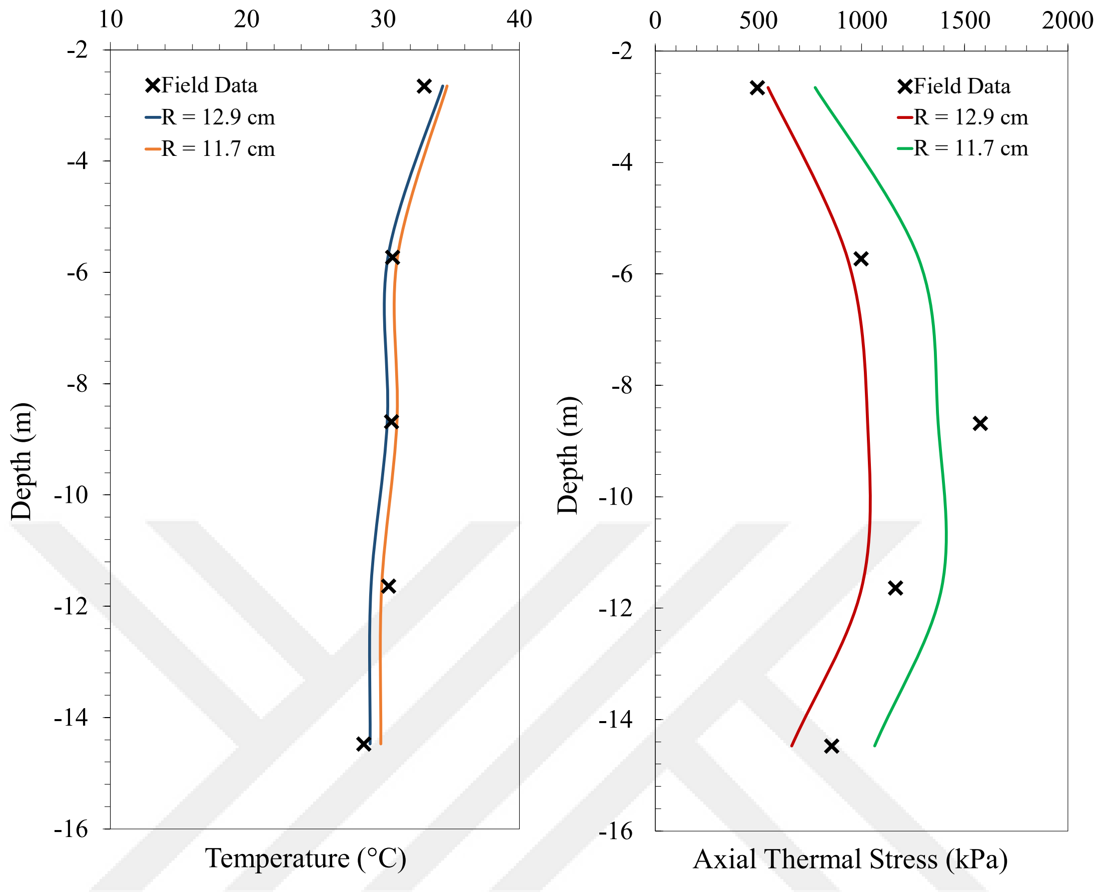

Figure 4.6. Comparison of temperatures and stresses along the pile between the field data and numerical simulation for Day-3.

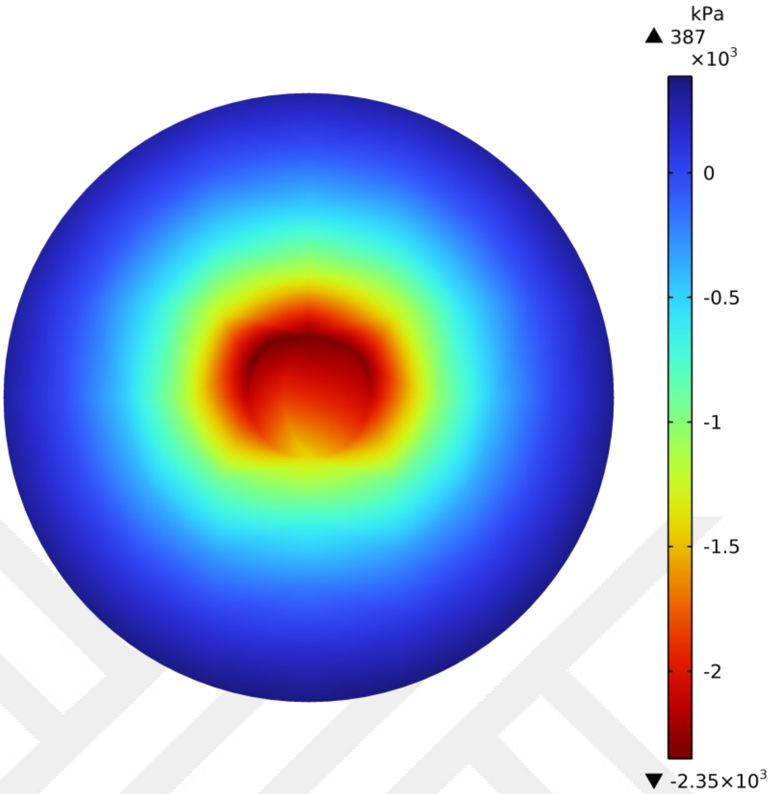

Figure 4.7. Thermally induced axial stresses in pile cross-section on day-1 at 8.7m depth.

5. VALIDATION OF ENERGY WALL

To evaluate the reliability of the developed numerical model, validation was performed using experimental data reported by Xia et al. (2012). Their field study was conducted between March and July 2011 in Shanghai, China, and focused on the thermal performance of a diaphragm wall located beneath the Shanghai Natural History Museum. In that study, three distinct heat exchanger configurations were investigated: (a) a W-shaped arrangement, (b) a modified W-shaped design, and (c) a single U-shaped pipe system. Each configuration was tested under different operational conditions, specifically varying inlet fluid temperatures and flow velocities, to assess their heat exchange effectiveness within an energy wall system.

The performance of each setup was evaluated under two operational regimes. The first was an intermittent mode, involving alternating cycles of 12-hour operation and 12-hour shutdown. The second mode was continuous operation, where the system remained active for 48 consecutive hours without interruption.

For the purpose of model validation in the current study, the single U-shaped pipe configuration was selected as the reference case. The simulation specifically replicates the continuous operation regime, during which the fluid was circulated at a velocity of 0.6 meters per second and entered the system at a temperature of 35°C. This configuration was chosen due to its relatively simple geometry and well-documented thermal performance, making it suitable for comparative analysis with numerical results.

5.1. Geometry

In the experimental setup, the single U-shaped pipes were manufactured using polyethylene material classified as PE-100. Each pipe had an outer diameter of 25 mm and a wall thickness of 2.3 mm, and they were installed at regular intervals of 75 cm. These pipes were embedded within diaphragm walls constructed from C30-grade concrete. The diaphragm wall structure extended to a total depth of 38 meters, with a uniform thickness of 1 meter and an excavation depth reaching 18.5 meters.

However, certain geometric parameters critical for accurate model representation were not explicitly stated in the original publication by Xia et al. (2012). Specifically, the authors did not provide details regarding the full width of the wall, the thickness of the concrete cover surrounding the pipes, or the precise vertical lengths of the embedded U-pipes. In order to address these omissions and allow for the generation of a complete numerical model, several assumptions were made based on supplementary literature. The wall width was taken as 1.5 meters and the concrete cover thickness as 100 mm, in line with recommendations found in Sun et al. (2013) and Sailer (2020).

Although the vertical extent of the embedded pipes has a relatively minor influence on the overall heat transfer performance, a vertical length of 37.5 meters was assumed for consistency with the values reported in Sailer (2020) and Bodas Freitas et al. (2024). Furthermore, according to the information provided by Xia et al. (2012), the base slab of the foundation structure was still under construction during the monitoring period. As such, this structural element was not included in the numerical validation model developed in the present study.

5.2. Initial Conditions

In the experimental study reported by Xia et al. (2012), temperature measurements were recorded at various depths along the diaphragm wall. Specifically, temperatures of 12.2°C, 25.0°C, and 21.2°C were measured at depths of 9 m, 25 m, and 35 m, respectively. Based on these observations, the average temperature of the wall was determined to be approximately 23°C. In comparison, the surrounding soil temperature was measured at 16.3°C, consistent with the regional average temperature range of 16°C to 17°C, as documented by Bodas Freitas et al. (2024).

The elevated temperatures observed in the deeper portions of the wall were attributed to heat generated during the concrete curing phase, during which temperatures reportedly reached between 60°C and 70°C due to the exothermic hydration process. In contrast, the lower temperatures in the upper section of the wall were likely influenced by direct exposure to the ambient atmosphere during cold weather conditions in March, when the experimental campaign commenced.

To accurately represent this thermal variation in the numerical model, the wall was divided into two zones with different initial temperature assignments. For the lower section, where the wall had reached thermal equilibrium with the surrounding soil over time, an initial temperature of 23°C was assigned, in line with the average reported by Xia et al. (2012). For the upper section, where the temperature is more susceptible to atmospheric variations and lacks precise test timing, a value of 16.3°C (matching the regional average) was used. This stratification method follows approaches adopted by previous researchers, including Dai et al. (2022) and Bodas Freitas et al. (2024).

The initial temperature of the soil posed a specific challenge. While the measured value was 16.3°C, prior studies such as Sailer (2020) highlighted that a thermal mismatch between the wall (23°C) and the soil (16.3°C) could impair the accuracy of simulation results. It is also reasonable to assume that heat from the hydration process likely increased the temperature of the surrounding soil near the wall interface. To avoid introducing artificial thermal discontinuities and ensure better agreement with realistic conditions, the initial temperature of the soil was set to 23°C, consistent with recommendations made by Sailer (2020) and Bodas Freitas et al. (2024).

5.3. Boundary Conditions

The thermal boundary conditions implemented in the numerical model were defined in accordance with the physical configuration of the experimental setup and the available environmental data. Due to the relatively short duration of the test (48 hours) and the sufficiently large spatial extent of the simulation domain, adiabatic (thermally insulated) boundary conditions were applied to the lateral (left and right) and bottom boundaries of the model. This assumption is commonly employed in short-term thermal simulations, where heat fluxes across distant boundaries are negligible.

The convective boundary conditions at the top surface and exposed excavation face presented additional complexity. No measurements or estimates for wind velocity or convective heat transfer coefficients were reported in the original study. Given the lack of this information and the short timeframe of the thermal loading, a constant temperature boundary condition was applied to these surfaces. The temperature was fixed at 16.3°C, representing the average ambient temperature for the region, which is consistent with values used in similar validation studies.

5.4. Material Properties

Since the study by Xia et al. (2012) did not include detailed thermo-mechanical property data for the concrete or the surrounding soil, these parameters were obtained from reliable sources in the existing literature to ensure realistic model inputs.

Table 4.1 summarizes the thermal and mechanical properties adopted in the model. The thermal conductivity, specific heat capacity, and density of both concrete and soil were sourced from Sailer (2020), while the linear coefficient of thermal expansion, Young's modulus, and Poisson's ratio were drawn from Dai et al. (2022). These values were chosen to ensure consistency with the most reliable studies available in the field.

Table 5.1. Material properties for soil and concrete.

Properties	Symbol	Unit	Concrete	Soil
Young's modulus	E	MPa	30000	23.7
Poisson's ratio	v	-	0.20	0.33
Density	ρ	kg/m^3	2500	1800
Specific heat capacity	c	J/kg°C	1690	1046
Thermal conductivity	λ	W/m°C	1.60	1.74
Thermal expansion coefficient	α	με/°C	1.20	0.60

5.5. Comparison of Results

To evaluate the accuracy of the numerical model, the simulation results were compared with the experimental data provided by Xia et al. (2012). This comparison focused on the temperature changes in the energy wall over the 48-hour test period. As shown in Figure 5.1, the simulation results closely follow the measured temperatures, showing that the model can reliably represent the real behaviour of the system.

A more detailed assessment was made by calculating the average error in two different time intervals. During the first 10 hours of the simulation, the average difference between the measured and simulated temperatures was 6.2%. This slightly higher error at the beginning is expected because temperature changes happen more quickly in the early hours, making accurate prediction more difficult.

After the 10th hour, the temperature field becomes more stable, and the model performs even better. Between the 10th and 48th hours, the average error dropped to 2.5%. When looking at the full 48-hour period, the overall average error was calculated as 3.3%.

These results show that the numerical model can successfully predict the thermal behaviour of the energy wall. The fact that the error becomes smaller over time also supports that the model works well not only at the beginning but also during longer-term operation.

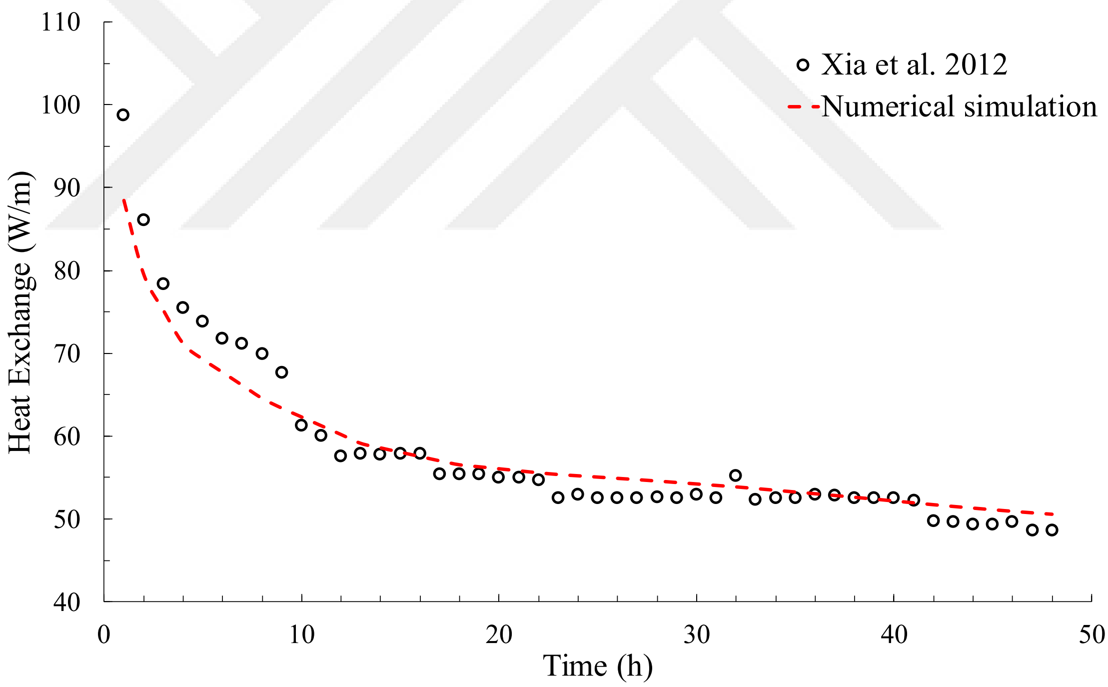

Figure 5.1. Comparison of measured data with numerical simulation.

6. NUMERICAL MODEL

This section outlines the numerical modelling approach used to analyse the thermo-mechanical response of an energy wall exposed to thermal loading. The primary focus is on investigate thermal stresses resulting from nonuniform temperature distributions within the wall. The subsequent subsections provide detailed information on the model setup, geometry, key assumptions, applied boundary conditions, thermal loading conditions and the adopted meshing strategy.

6.1. Description of The Model

In order to analyse the development of non-uniform stresses resulting from temperature variations within an energy wall, numerical simulations were carried out using COMSOL Multiphysics. The simulation framework incorporated three primary physics interfaces along with a multiphysics coupling feature:

- Heat Transfer in Porous Media – to simulate heat transfer within both the wall and surrounding soil.
- Heat Transfer in Pipes – to represent the thermal behaviour of the circulating fluid within the embedded heat exchanger.
- Solid Mechanics – to capture the mechanical response of the wall and soil.
- Thermal Expansion – to establish the coupling between heat transfer in porous media and solid mechanics modules, enabling the simulation of thermo-mechanical behaviour in both the energy wall and the surrounding soil.

6.2. Model Geometry

The numerical model was constructed to represent the geometry of an energy wall system embedded within a homogeneous soil medium. The diaphragm wall extends to a depth of 38 m below ground level, with a total thickness of 1 m and a width of 3 m. A concrete cover of 100 mm was applied along the wall to reflect typical construction practice. On the retained side, the soil height reaches 60 m, while on the excavated side it extends to 41.5 m, resulting in an excavation depth of 18.5 m. The model domain has a total horizontal span of 50 m to minimise the influence of boundary conditions. Two structural slabs are included in the model: a 1 m thick slab located directly on top of the excavated soil, and another 1 m thick slab positioned horizontally at ground level, aligned with the top of the diaphragm wall.

The embedded heat exchanger system consists of single W-shaped pipes spaced at 75 cm intervals along the wall. To reduce computational effort, these pipes were represented as line elements in the model. Their actual geometry was later defined in the Heat Transfer in Pipes interface using a pipe diameter of 25 mm and a wall thickness of 2.3 mm, corresponding to polyethylene (PE-100) material. The pipes were assumed to be positioned with a concrete cover of 100 mm, in line with typical construction practice. The vertical length of the heat exchanger pipes was assumed to be 37.5 m. A detailed view of the model geometry is presented in Figure 6.1.

6.3. Modelling Assumptions

The numerical model was developed based on a set of simplifying assumptions to ensure computational efficiency while capturing the key physical behaviour of the system. Both the soil and the wall–slab assembly were modelled as porous media. No interface elements were introduced between the soil and the energy wall; a fully bonded interaction was assumed. The soil, energy wall and the slabs were considered to behave as isotropic, linear elastic materials. Inertial effects were neglected, as the analysis focused solely on the quasi-static thermal and mechanical response.

Material properties used for the soil and concrete are summarised in Table 5.1. All material parameters were assumed to be constant and independent of temperature throughout the simulation. The heat exchanger fluid modelled as water with a flow rate of 0.6 m/s.

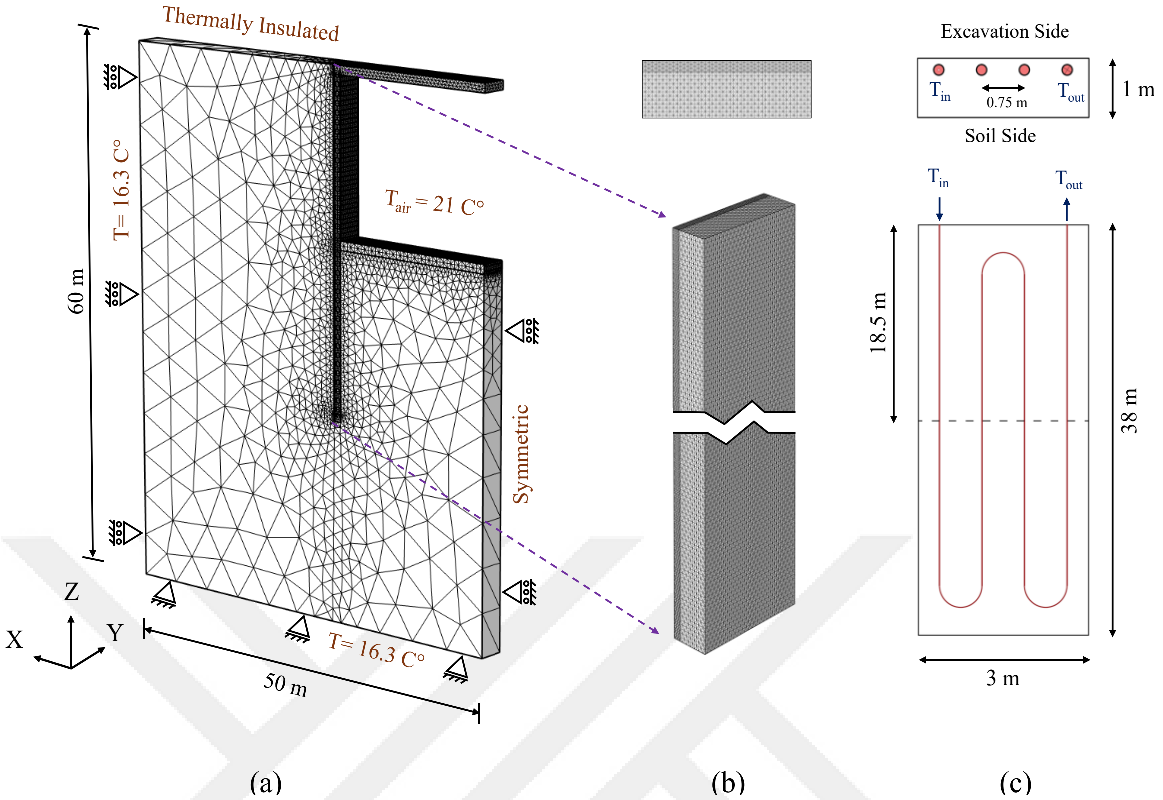

Figure 6.1. Numerical model setup: (a) 3D representation and boundary conditions, (b) Mesh configuration of the energy wall, (c) Cross-sectional layout of the pipe arrangement inside the energy wall.

6.4. Boundary and Initial Conditions

The thermal and mechanical boundary conditions applied in the model are illustrated in Figure 6.1. For the mechanical boundary conditions, the bottom surface of the model was fully fixed in all directions. The two vertical side boundaries, aligned with the wall's thickness direction, were assigned roller constraints to restrict horizontal displacement while allowing vertical movement. The lateral boundaries along the wall's width direction were treated as planes of symmetry, reducing the computational domain without compromising the accuracy of the results. The top surface was modelled as free.

For the thermal boundary conditions, the initial temperature of the entire model domain was set to 16.3 °C to represent the average undisturbed ground temperature. The left and bottom boundaries were held at a constant temperature of 16.3 °C throughout the simulation to mimic the thermal influence of the surrounding ground mass. The right-side boundary was treated as thermally symmetric, implying zero heat flux. The top surface was considered thermally insulated, assuming negligible heat exchange with the atmosphere.

To simulate the environmental conditions around the excavated area, natural heat convection was applied to the exposed boundaries. This boundary condition was defined using an ambient air temperature of 21 °C, representing a controlled thermal environment often present in practical applications such as basement levels or underground structures (Faizal et al., 2016).

6.5. Thermal Loading Conditions

The thermal loading in this study was designed to reflect continuous heat injection and extraction under extreme conditions (Ravera et al., 2024; Bosch et al., 2024) as the primary objective is to investigate the resulting thermal stress distributions. To simulate critical operating scenarios, a constant fluid temperature of 45 °C was applied for the heat injection case, and 5 °C for the heat extraction case. These boundary conditions were chosen to examine the system's behaviour under maximum thermal loading. The total simulation period was defined as 90 days for both heat injection and extraction scenarios to capture long-term thermal and mechanical responses.

6.6. Mesh

The mesh used in the numerical model is illustrated in Figure 6.1. The entire domain was discretized into a total of 1,946,801 finite elements. The soil and slab regions were meshed using free tetrahedral elements, while a mapped meshing technique was applied to the energy wall. This approach ensured more uniform element distribution along the wall and allowed for consistent stress calculations at each depth level.

A targeted mesh refinement was applied around the concrete cover region, where the heat exchanger pipes are embedded, to improve the resolution of thermal and mechanical responses in this critical zone. Of the total elements, 1,580,173 were assigned to the energy wall alone, providing sufficient resolution to accurately capture the coupled thermo-mechanical behaviour.

7. RESULTS AND DISCUSSIONS

The numerical model developed in this study was employed to investigate the thermal stress behaviour of energy walls subjected to non-uniform temperature distributions under two representative operational scenarios: heat injection during the summer period and heat extraction during the winter period. These scenarios reflect typical seasonal operating conditions of ground heat exchanger systems and are essential for evaluating the long-term structural performance of energy walls.

As previously discussed in Chapter 3, the directions and nature of thermally induced stresses vary significantly depending on the temperature distribution characteristics within the wall. In Zone 1, the temperature field exhibits a circular distribution due to the geometry and location of the embedded heat exchange pipes. Accordingly, a cylindrical coordinate system was used to conceptually explain the development of axial, radial, and circumferential stresses in this zone. On the other hand, in Zone 3, where the temperature gradient is more linear and aligned with the geometry of the wall, a Cartesian coordinate system was adopted to describe the resulting thermal deformations and stresses along the X, Y, and Z directions.

Although these conceptual frameworks help clarify the underlying mechanical mechanisms in different zones, the numerical results are presented using only the Cartesian coordinate system. This decision was made to enable a unified and continuous representation of the stress field across the entire cross-section of the energy wall. Using a single coordinate system also allows for the inclusion of intermediate regions such as Zone 2, where the temperature distribution gradually transitions from circular to linear, and where neither cylindrical nor Cartesian descriptions alone would be sufficient to fully capture the behaviour. Presenting all stress components in Cartesian coordinates facilitates clearer comparison between zones and provides a consistent basis for interpreting the overall response of the structure.

The analysis was conducted on a representative cross-section located at a depth of 9 meters, corresponding to approximately half the total excavation depth. This depth was selected to capture the typical thermal and structural behaviour in the central portion of the wall, where the effects of surface boundary conditions and base constraints are relatively balanced. The temporal evolution of the temperature distribution at this section was examined at six different time intervals: 0.1 hour, 2 hours, 1 day, 7 days, 30 days, and 90 days. These intervals were chosen to reflect both the short-term and long-term thermal response of the system.

Thermally induced stresses corresponding to each time step were computed and analyzed in all three principal directions (X, Y, and Z). The results are presented for two mutually orthogonal cross-sections (identified as Section A and Section B) to provide a more comprehensive understanding of the three-dimensional stress distribution within the energy wall. The locations and orientations of these sections are illustrated in Figure 7.1.

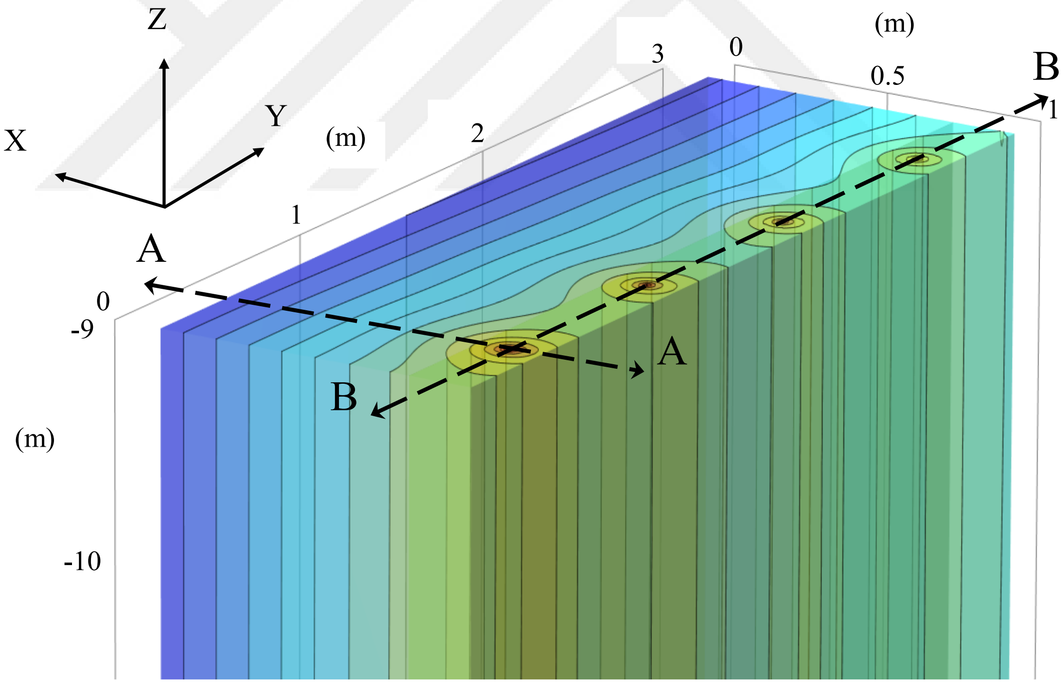

Figure 7.1. The locations of cross-sections A and B taken from the energy wall.

7.1. Evolution of Non-Uniform Temperature Distribution

Figures 7.2 and 7.3 illustrate the non-uniform temperature distributions within the energy wall cross-section located at a depth of 9 meters, for the heat injection and heat extraction scenarios, respectively. These figures present the spatial variation of temperature at selected time intervals, providing insight into how thermal gradients evolve over both short and long durations. In addition to these cross-sectional views, Figures 7.4 and 7.5 display the temporal development of the temperature profile along Section A (aligned perpendicular to the wall face) again for both heat injection and extraction cases. Similarly, Figures 7.6 and 7.7 show temperature evolution along Section B, which is orthogonal to Section A. These results collectively offer a more comprehensive understanding of the directional behaviour of heat propagation within the wall under seasonal thermal loads.

As expected, the largest temperature changes are observed in regions surrounding the inlet pipe, where the fluid first enters the heat exchanger system. The thermal effect gradually diminishes as the fluid moves along the pipe network toward the outlet, establishing a clear thermal gradient along the wall's cross-section. This behaviour reflects the influence of the fluid's thermal capacity and the continuous exchange of heat with the surrounding concrete and soil.

At the initial time steps, namely 0.1 hour and 2 hours, shown in Figures 7.2a, 7.2b, 7.3a, and 7.4b, temperature changes are confined to the immediate vicinity of the embedded pipes, forming a circular temperature distribution. This localized heating or cooling pattern arises because there has not yet been sufficient time for heat to diffuse through the wall mass. As time progresses, particularly after Day 1, the affected thermal zone expands outward from the pipes and begins to influence the building-facing side of the wall. As a result, the temperature field becomes increasingly complex: while the circular pattern around the pipes remains visible, a secondary linear temperature distribution begins to form near the interior surface of the wall.

The temperature data along Section A (Figures 7.4 and 7.5) further confirm this behaviour. In the early hours, especially up to Day 1, minor temperature changes are observed on the building-facing surface. These changes are partly due to heat transfer between the concrete surface and the adjacent air volume inside the basement. This effect is more pronounced in the heat extraction scenario (Figure 7.5), where the temperature near the surface initially increases. However, as the heat from the embedded pipes becomes the dominant influence over time, the contribution from air-side heat exchange becomes relatively negligible.

Throughout the full duration of the simulation, the circular thermal gradient around the pipes quickly reaches its maximum intensity within the early hours and then stabilizes in shape while slightly decreasing in magnitude. In contrast, the linear gradient observed near the building-facing surface strengthens progressively over time. This reflects the gradual migration of heat through the wall, highlighting the combined effects of conductive transfer and geometric configuration. The observed temporal shift from localized to more distributed heat propagation underscores the dynamic thermal response of the energy wall system under operational conditions.

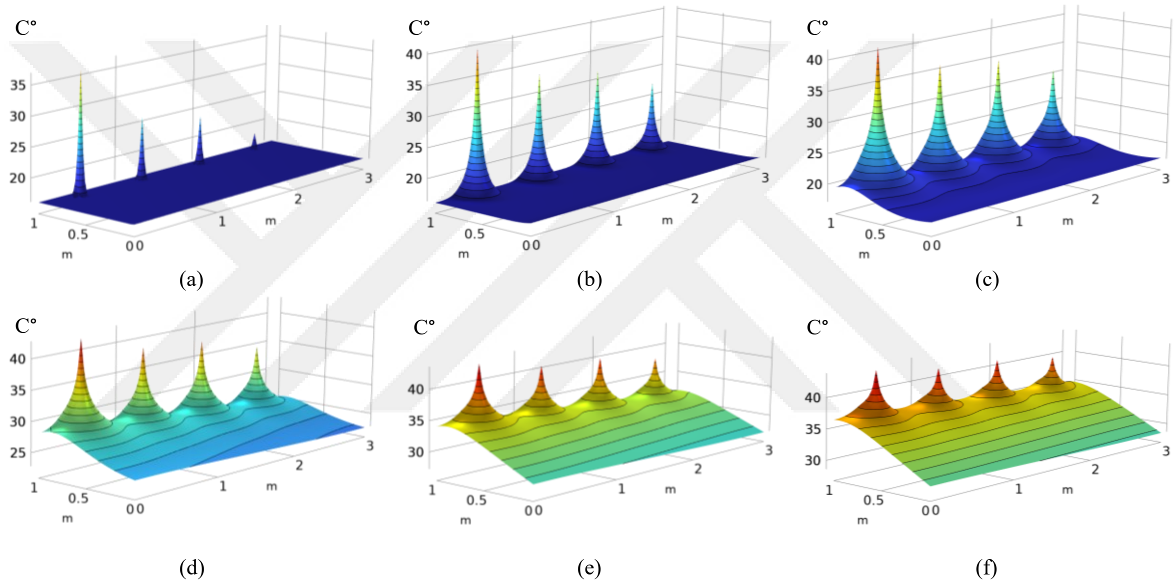

Figure 7.2. Evolution of non-uniform temperature distribution for the heat injection at different time intervals at -9 m section: (a) 0.1h, (b) 2h, (c) 1 day, (d) 7 days, (e) 30 days, (f) 90 days.

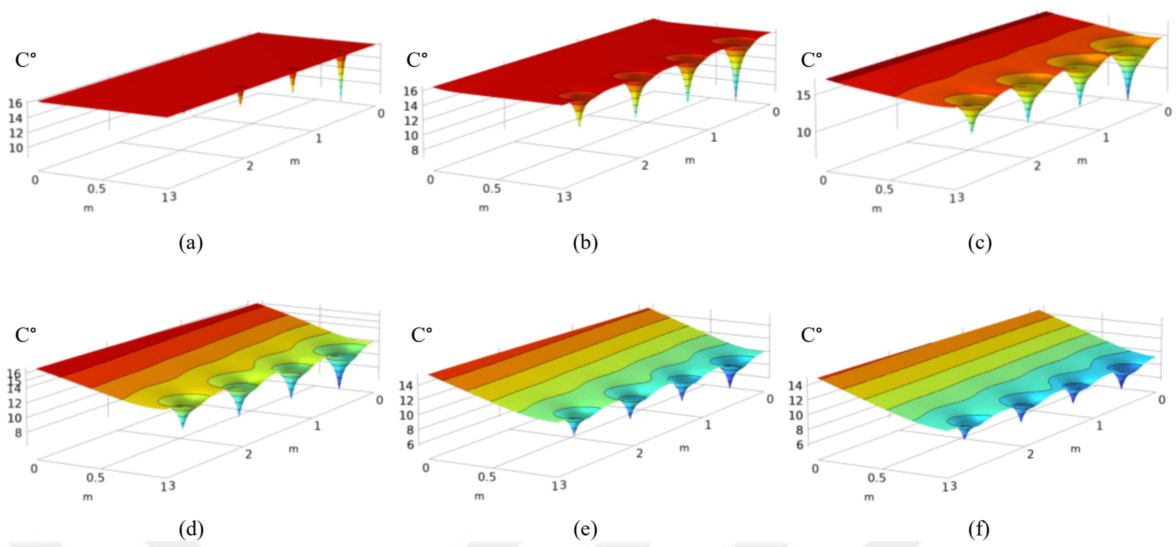

Figure 7.3. Evolution of non-uniform temperature distribution for the heat extraction case at different time intervals at -9 m section: (a) 0.1h, (b) 2h, (c) 1 day, (d) 7 days, (e) 30 days, (f) 90 days.

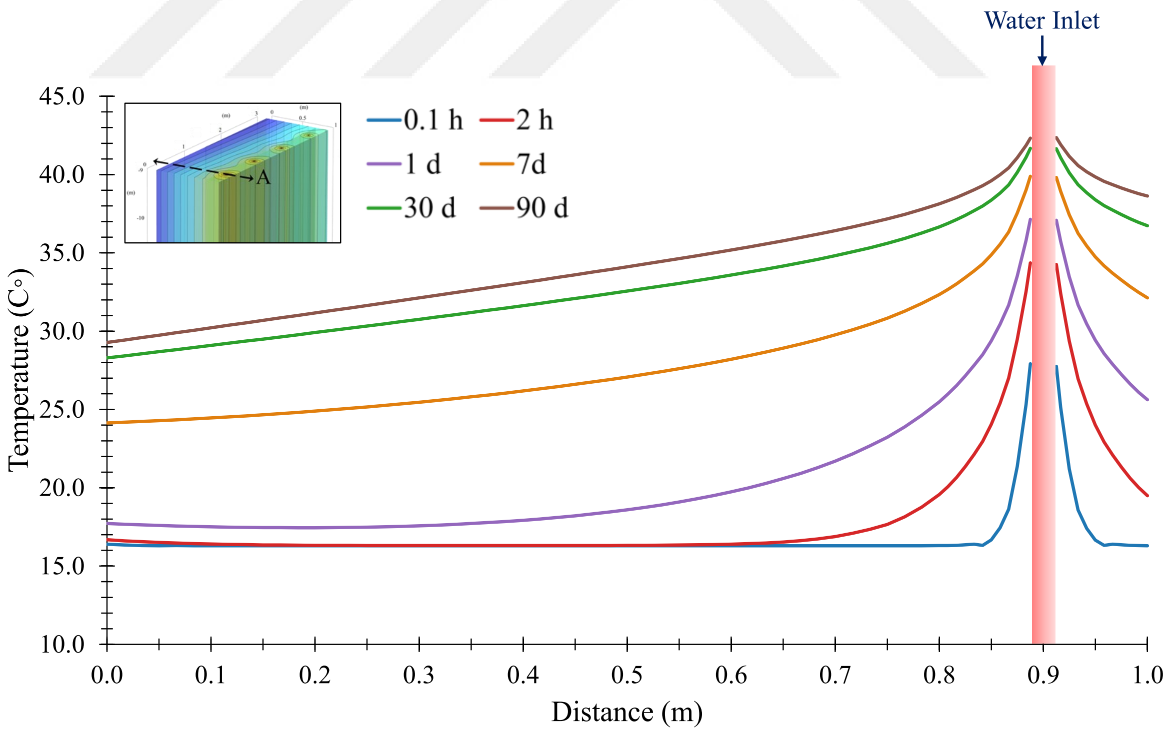

Figure 7.4. Distribution of temperature at section A under heat injection scenario.

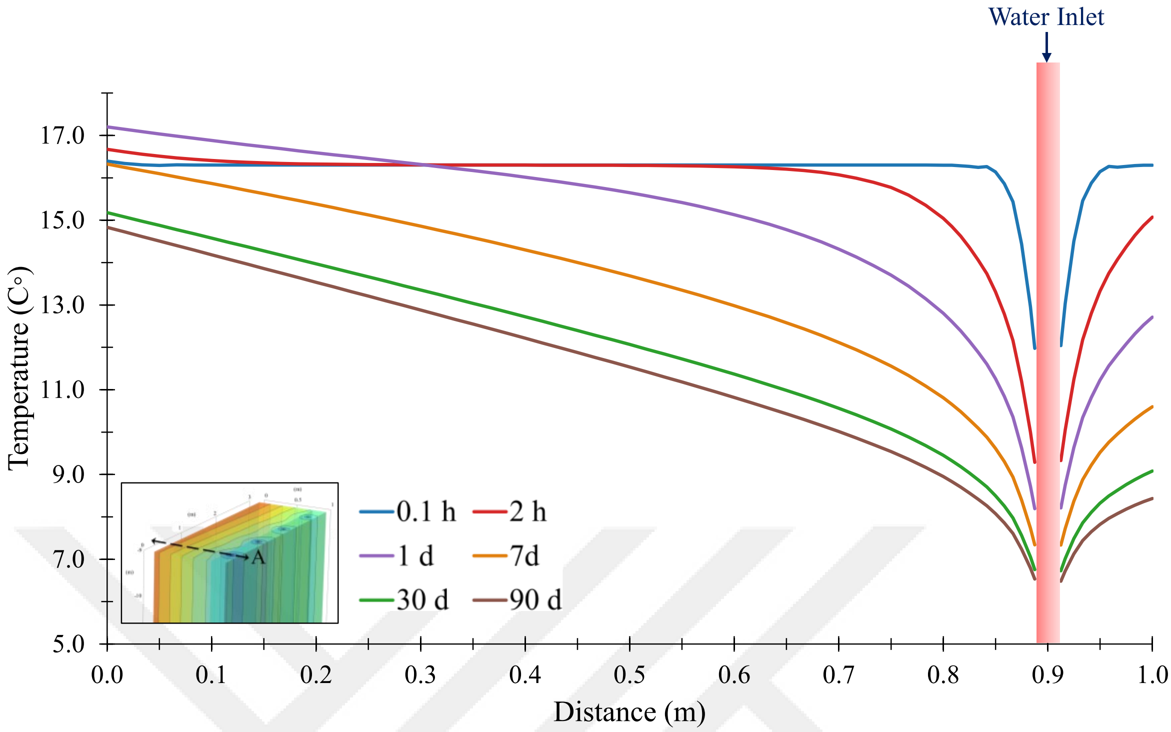

Figure 7.5. Distribution of temperature at section A under heat extraction scenario.

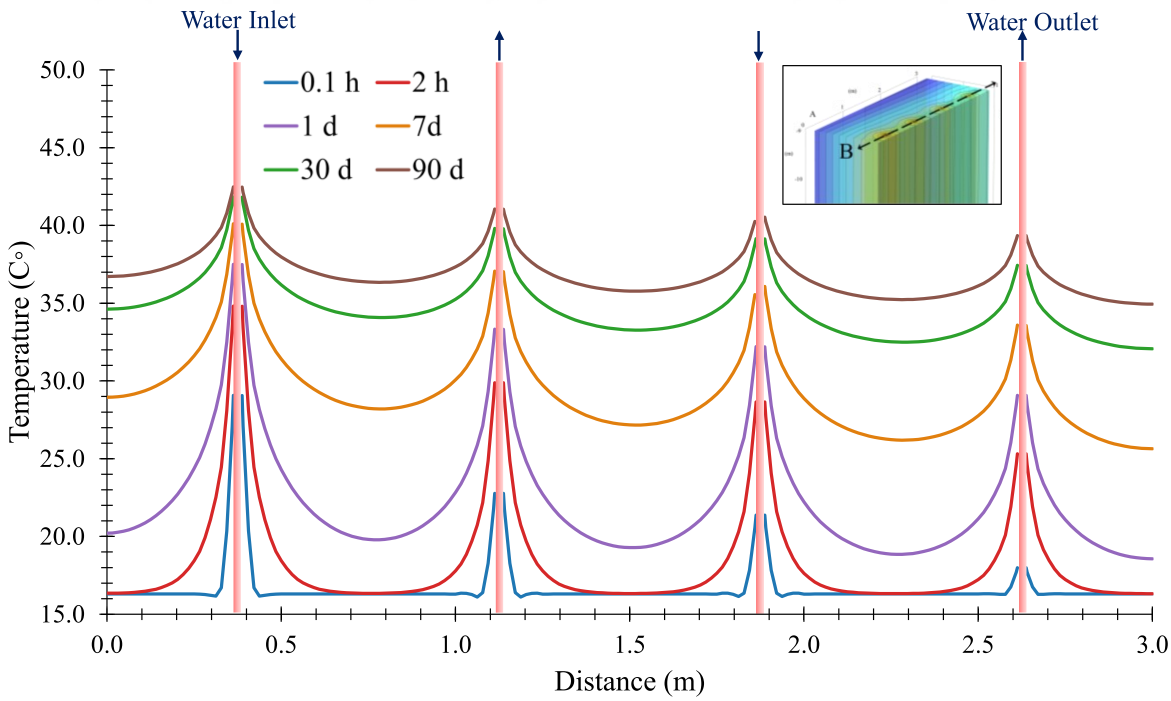

Figure 7.6. Distribution of temperature at section B under heat injection scenario.

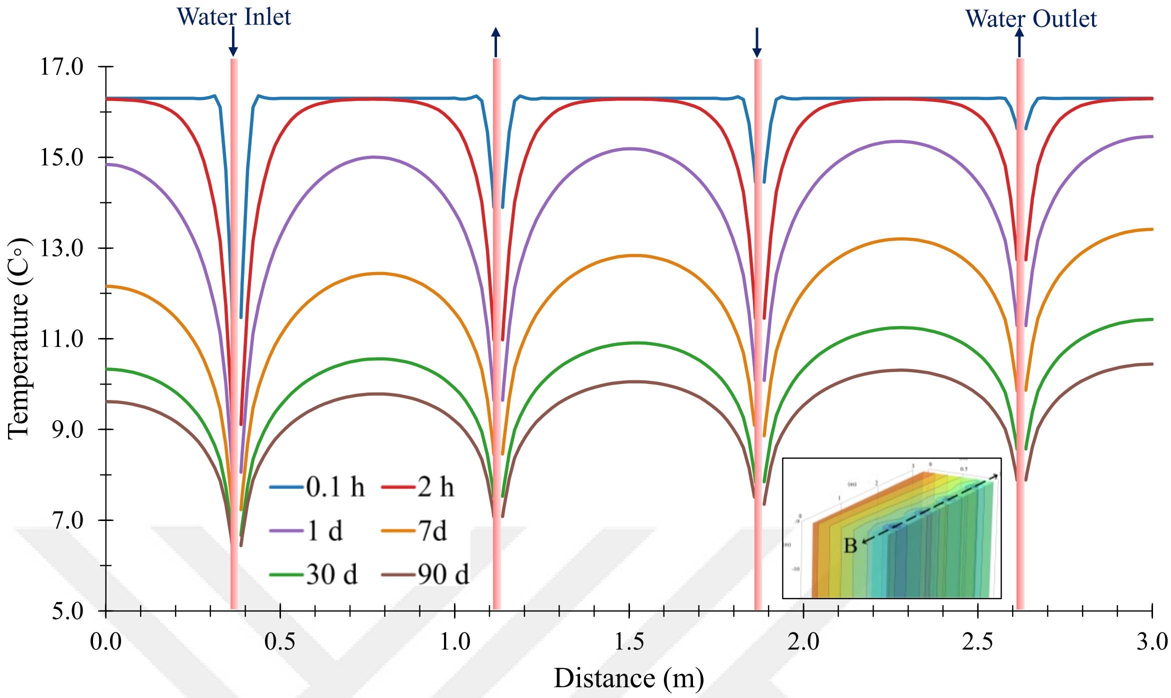

Figure 7.7. Distribution of temperature at section B under heat extraction scenario.

7.2. Influence of Non-Uniform Temperature Distribution and Boundary Conditions on Thermally Induced Stresses

This section presents the thermally induced stress components in the X, Y, and Z directions, evaluated along Sections A and B. The purpose is to investigate how spatial variations in temperature, combined with the imposed mechanical boundary conditions, contribute to the development of thermal stresses within the energy wall.

To simulate these effects, the numerical model incorporates the following boundary conditions for mechanical constraints:

- X direction: The wall is restrained only along its top and bottom edges on the building-facing side.
- Y direction: A representative 3-meter-wide segment of the wall is modelled, with full fixation applied along this axis, preventing lateral displacement.
- Z direction: No external vertical load is applied to the wall. The only restraint in

this direction comes from the interaction between the wall and the surrounding soil at the soil-wall interface.

By combining the effects of the non-uniform temperature field with these mechanical constraints, the model provides a clearer understanding of how thermal gradients lead to stress development in different directions. This integrated approach allows for a more realistic assessment of the structural behaviour of energy walls operating under typical field conditions.

7.3. Thermally Induced Stresses along Section A

The thermal stress distribution in the X direction was assessed at three distinct locations along Section A to capture the spatial variation of stress responses within the energy wall. The first location, referred to as “near the pipe” within Zone 1, corresponds to a horizontal distance of 0.9125 m and represents the area immediately adjacent to the thermal pipe. The second location, denoted as the “outer boundary of Zone 1,” is located at 1.0 m and marks the interface between the concrete wall and the surrounding soil cover. The third location, at 0.0 m, represents the building-facing surface of the wall and corresponds to the interface between the concrete and the adjacent air space. All discussions and comparisons for Section A reference these fixed points consistently.

Figures 7.8 and 7.9 present the thermally induced stress responses in the X direction for both heat injection and heat extraction conditions, respectively. The largest stresses are observed near the thermal pipe, where the temperature distribution is highly circular due to localized heating or cooling, representative of Zone 1 behaviour. As described in Chapter 3, the X direction corresponds to the radial axis in cylindrical coordinates. Hence, the reported X-direction stresses can also be interpreted as thermally induced radial stresses originating from the circular temperature field around the pipe.

In the heat injection scenario, thermally induced compressive stresses near the pipe rapidly reach a peak of approximately 4.15 MPa within the first 0.1 hours. These stresses then decrease steadily over time, falling to around 0.80 MPa by day 90. Similarly, in the heat extraction case, peak tensile stresses near the pipe initially reach about 2.10 MPa at 0.1 hours and gradually decline to roughly 0.45 MPa by day 90. As expected, stress values near the outer boundary of Zone 1 remain minimal in both scenarios, due to the limited confinement provided by the surrounding soil.

Toward the building-facing side of the wall, thermally induced stresses also remain close to zero. This is primarily attributed to the linear nature of the temperature distribution in this region and the absence of external mechanical restraints in the X direction. Between the pipe and the building-facing surface, the temperature distribution gradually shifts from circular to linear. This change occurs progressively rather than abruptly, and as a result, the thermal stresses also decrease smoothly along this path. The gradual reduction in stress is directly linked to this spatial transition in the temperature field, which reflects the changing thermal behaviour from Zone 1 to Zone 3.

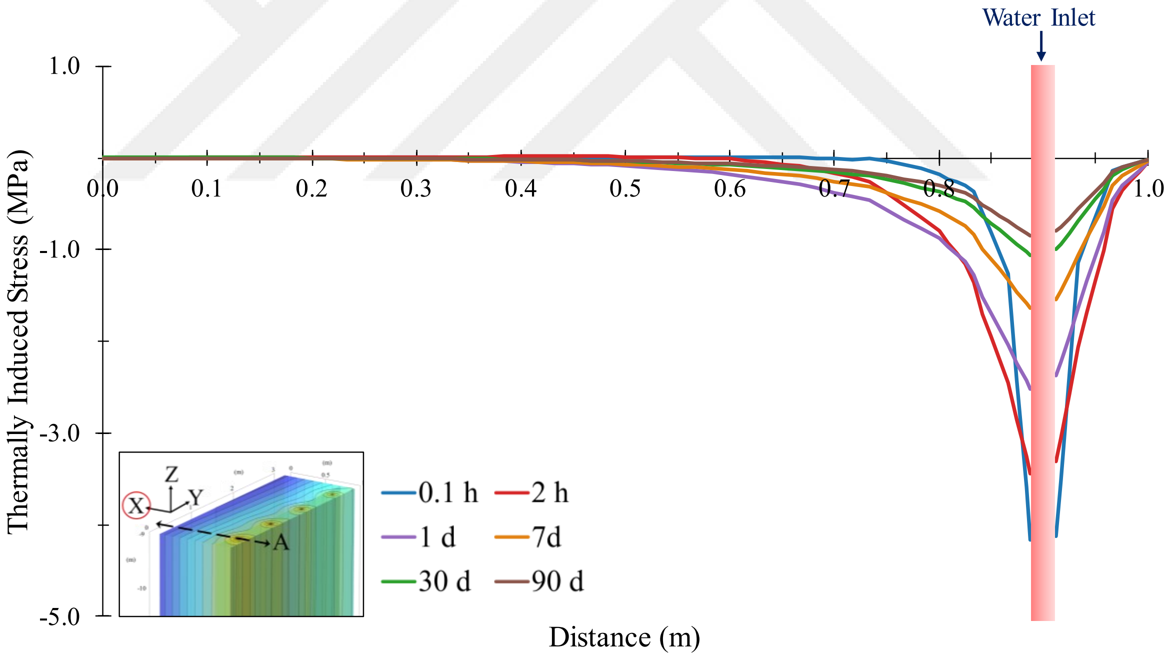

Figure 7.8. Thermally induced stresses in the X-direction at section A for the heat injection case.

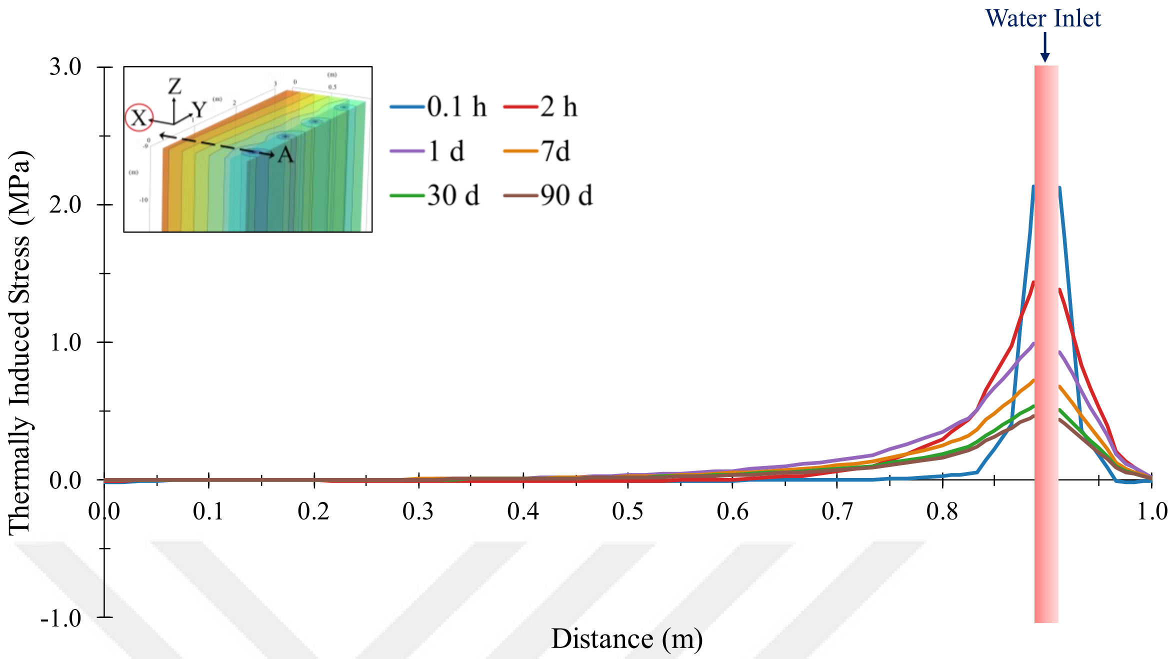

Figure 7.9. Thermally induced stresses in the X-direction at section A for the heat extraction case.

In addition to the X-direction stresses, thermally induced stresses in the Y direction at Section A are also evaluated. Within Zone 1, these stresses correspond to circumferential (hoop) stresses in the cylindrical coordinate system. Figures 7.10 and 7.11 present the Y-direction stress distributions for the heat injection and heat extraction scenarios, respectively.

In both scenarios, thermally induced stresses within Zone 1 and Zone 3 evolve considerably over time due to the influence of mechanical boundary conditions and the changing temperature field. The constraint along the Y-axis limits the lateral expansion and contraction of the wall, resulting in a progressive shift in stress distribution during thermal loading. This behaviour is observed in the form of gradual vertical changes in the stress profiles. Notably, the temporal evolution of temperature gradients differs between zones. In Zone 1, the gradient weakens over time, reducing thermal differentials and gradually flattening the stress profile. In contrast, in Zone 3, the gradient intensifies, leading to a steeper stress profile due to an increase in thermal differential.

Near the pipes, where the circular temperature distribution is strongest, thermally induced stresses vary depending on the thermal loading condition. Under heat injection, compressive stresses develop rapidly, reaching approximately 4.70 MPa within 0.1 hours. These stresses briefly decline but then steadily rise, reaching around 8.50 MPa by day 90, as shown in Figure 7.10. In the case of heat extraction, presented in Figure 7.11, tensile stresses initially reach 2.25 MPa within 0.1 hours. Following a short decline, they gradually increase to approximately 3.10 MPa by day 90. This overall trend is governed by the combination of a decreasing temperature gradient and a fixed lateral boundary condition, which together control the sustained rise in stress despite transient reductions in the thermal differential.

At the outer boundary of Zone 1, near the interface between the concrete wall and the surrounding soil, thermally induced stresses show a different trend. During heat injection, tensile stresses peak at about 3.45 MPa within the first 2 hours, but then progressively shift to compression, reaching around 6.30 MPa by day 90. In contrast, during heat extraction, compressive stresses develop initially, around 1.30 MPa, but gradually transition into tensile stresses that rise to nearly 2 MPa by day 90. These reversals in stress type and magnitude are mainly attributed to the Y-direction constraint and the evolving thermal conditions in this outer region of Zone 1.

In Zone 3, near the building-facing side of the wall where the temperature distribution is linear, thermally induced stresses gradually decrease toward the surface in alignment with the temperature gradient, as illustrated in Figures 7.10 and 7.11. While the influence of heat from the pipes begins to reach this region after approximately one day, thermal interaction between the wall surface and the adjacent indoor air starts from the beginning, as indicated in Figure 7.5. This early heat exchange leads to similar initial stress levels under both heat injection and extraction scenarios, with compressive stresses around 0.45 MPa observed at the wall surface. The similarity arises from the identical initial thermal conditions shared by the wall and the indoor environment.

After the first day, the stress behaviour near the building-facing side diverges between the two scenarios. In the heat injection case, compressive stresses steadily rise over time due to continued heat propagation from the pipes, reaching approximately 4.15 MPa by day 90.

Conversely, during heat extraction, compressive stresses near the building-facing wall surface gradually diminish and transition into tensile stresses, reaching around 0.20 MPa by day 90. This change occurs because, over time, the cooling influence of the pipes overtakes the initial warming effect caused by heat exchange with the indoor air.

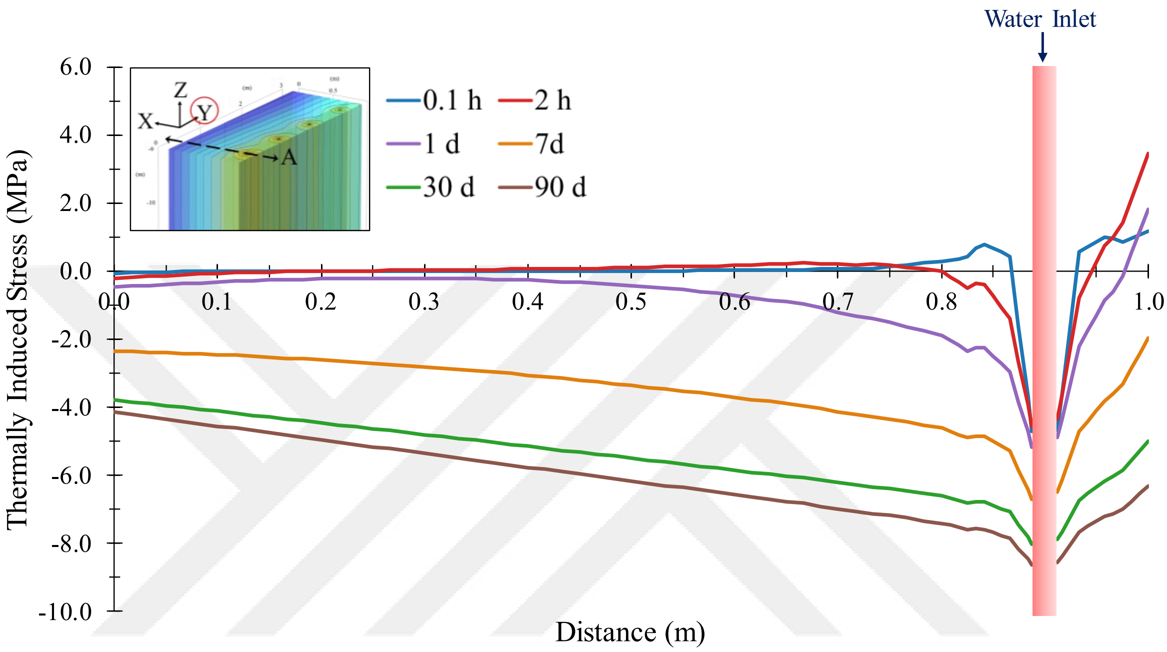

Figure 7.10. Thermally induced stresses in the Y-direction at section A the heat injection case.

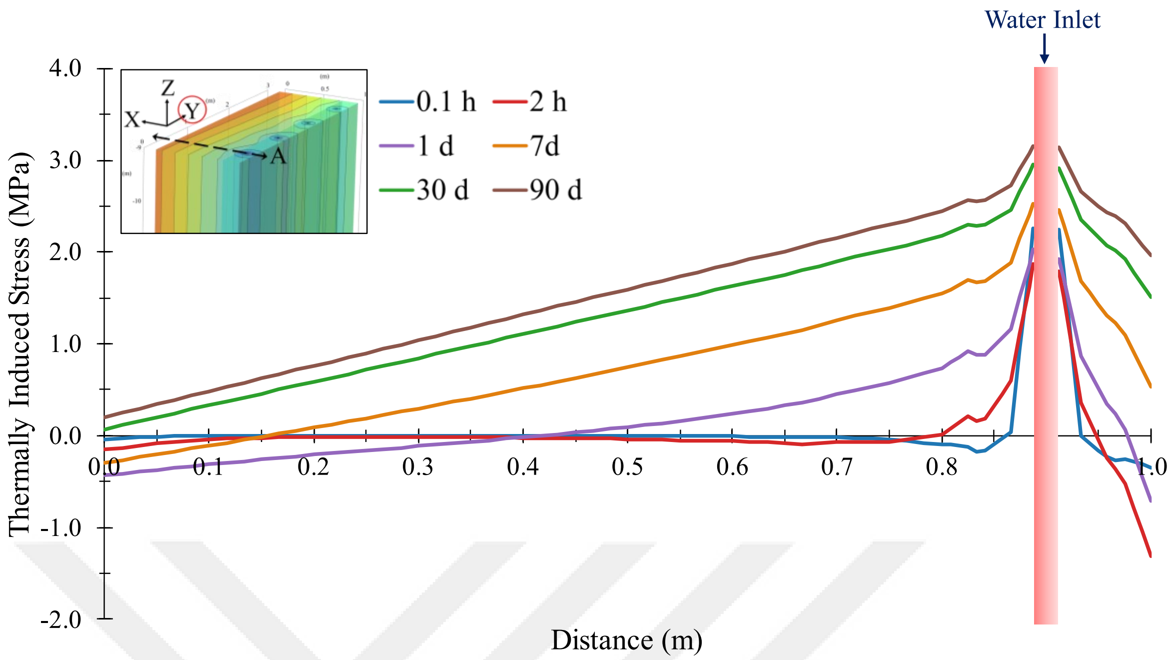

Figure 7.11. Thermally induced stresses in the Y-direction at section A the heat extraction case.

Thermally induced stresses in the Z-direction at Section A are presented in Figures 7.12 and 7.13 for the heat injection and heat extraction scenarios, respectively. In Zone 1, near the pipe, heat injection leads to a rapid increase in compressive stresses, reaching approximately 6.40 MPa within 0.1 hours, peaking at around 8 MPa by 2 hours, and then gradually decreasing to about 4 MPa by day 90. Under heat extraction, tensile stresses develop more moderately, reaching 2.70 MPa at 0.1 hours, increasing to 3.30 MPa at 2 hours, and decreasing slightly to approximately 2.35 MPa by day 90. These variations directly reflect the evolution of the local temperature gradient, which intensifies during the first two hours and gradually diminishes thereafter, as shown in Figures 7.4 and 7.5.

At the outer boundary of Zone 1, the behaviour differs. In the heat injection scenario, thermally induced stresses begin as slight tension at 0.1 hours, quickly transition to compression, and reach approximately 2 MPa by day 90. For the heat extraction case, initial stresses are nearly zero in compression but progressively transition into tension, ultimately reaching around 1.30 MPa by day 90. Although no external vertical load is applied, the soil-structure interaction at the wall interface plays a crucial role in shaping this stress response.

In Zone 3, near the building-facing side of the wall, the thermal stress behaviour exhibits a directional shift. In the heat injection scenario, compressive stresses near the pipe gradually evolve into tensile stresses closer to the building-facing surface. In contrast, the heat extraction scenario shows a transition from tension near the pipe to compression toward the building-facing surface. By day 90, stresses at the excavation-facing surface reach approximately 1.90 MPa in tension under heat injection and around 1.30 MPa in compression under heat extraction. These distributions are primarily governed by the local temperature gradients and the absence of vertical loading in the Z-direction.

A key insight from this analysis is the influence of constraint conditions on thermal stress behaviour. In less constrained directions, such as the X-direction, stresses are more sensitive to temperature gradients. In contrast, in more restricted directions like the Y-direction, changes in average temperature become the dominant factor. This distinction arises because, in unconstrained settings, neighbouring regions serve as internal restraints, amplifying the impact of local temperature gradients.

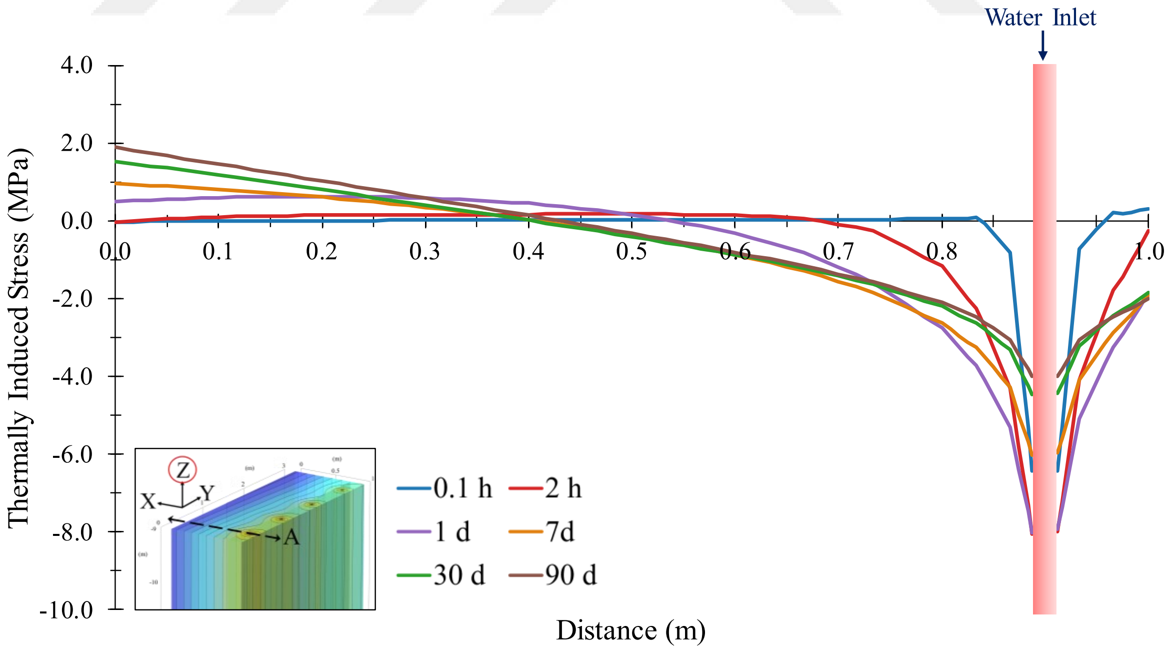

Figure 7.12. Thermally induced stresses in the Z-direction at section A for the heat injection case.

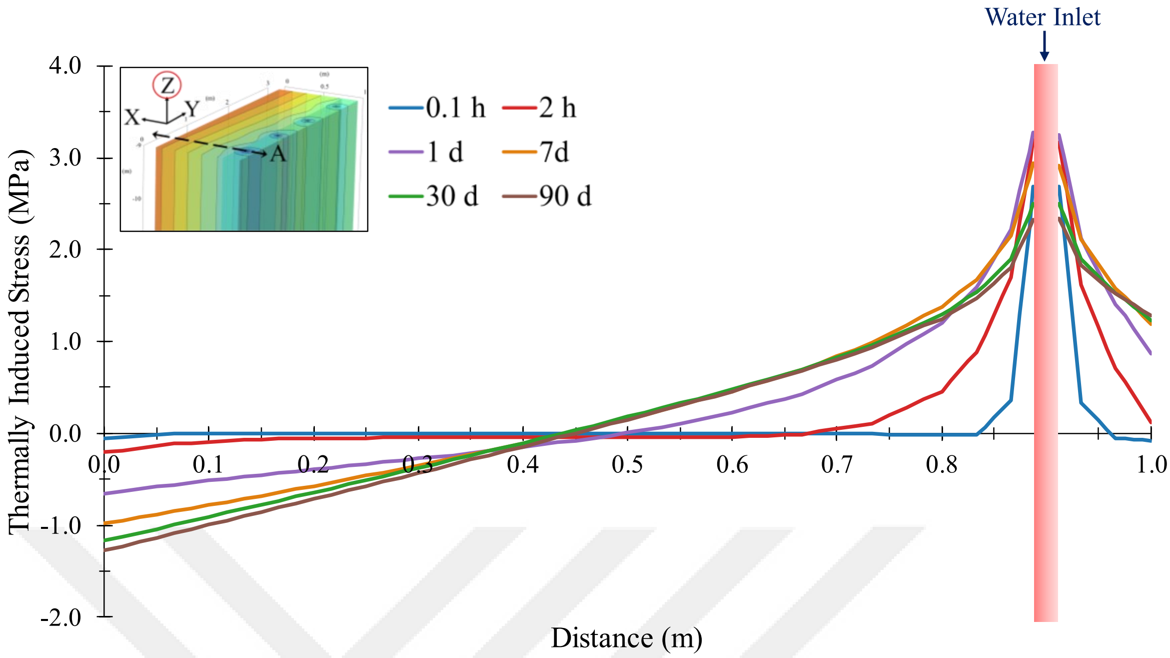

Figure 7.13. Thermally induced stresses in the Z-direction at section A for the heat extraction case.

7.4. Thermally Induced Stresses along Section B

Section B is analysed to further explore the evolution of temperature fields and thermally induced stresses over time within the energy wall. As shown in Figure 7.1, this section is orthogonal to Section A and intersects four thermal pipes, each surrounded by a circular temperature distribution zone (Zone 1). Between these pipes lie transitional regions defined as Zone 2, where the temperature distribution becomes irregular and leads to more complex stress patterns. Unlike Section A, Section B does not extend into Zone 3, and its stress profiles are influenced solely by the configuration of Zones 1 and 2.

The analysis focuses on the inlet pipe region, as it shows the highest temperature difference from the wall and is therefore the most critical for evaluating thermal effects. X-direction stresses for heat injection and extraction cases are shown in Figures 7.14 and 7.15. In this analysis, "near the inlet pipe" refers to 0.3875 meters on the horizontal axis labelled "Distance," which represents the area adjacent to the pipe wall.

In Section B, the outer boundary of Zone 1 moves over time as a result of thermal diffusion. A similar shift occurs in Section A, but the wall-soil interface there serves as a fixed reference point. Another key difference is the direction of analysis. In Section A, the X-direction aligns with the radial direction, whereas in Section B, it corresponds to the circumferential or hoop direction in cylindrical coordinates. As a result, the stresses shown in Section B represent thermally induced circumferential stresses caused by the uneven temperature distribution around the pipes.

During heat injection, thermally induced compressive stresses near the inlet pipe rapidly develop, reaching approximately 4.90 MPa within 0.1 hours. As the temperature gradient surrounding the pipe decreases, these stresses gradually diminish, reaching about 0.75 MPa in compression by day 90. Under heat extraction conditions, tensile stresses rise to around 2.55 MPa within 0.1 hours and then steadily decline, reducing to approximately 0.42 MPa tension by day 90. This decreasing trend in both scenarios reflects the diminishing thermal differential near the pipe wall over time.

At the outer boundary of Zone 1, a similar reduction in stress magnitude is observed. In the heat injection scenario, thermally induced tensile stresses initially develop, reaching approximately 1.25 MPa at 0.1 hours and then decreasing to about 0.15 MPa by day 90. Likewise, in the heat extraction scenario, tensile stresses form initially at around 0.35 MPa and gradually decline to approximately 0.08 MPa by day 90. These diminishing stresses result from the decreasing temperature gradient and the relatively unconfined conditions at the pipe-soil interface.

As anticipated, stress development is minimal at the midpoints between adjacent pipes. These locations fall within Zone 2, where the temperature distribution is no longer circular, and the gradient becomes less uniform. As a result, thermally induced circumferential stresses do not significantly develop in these regions.

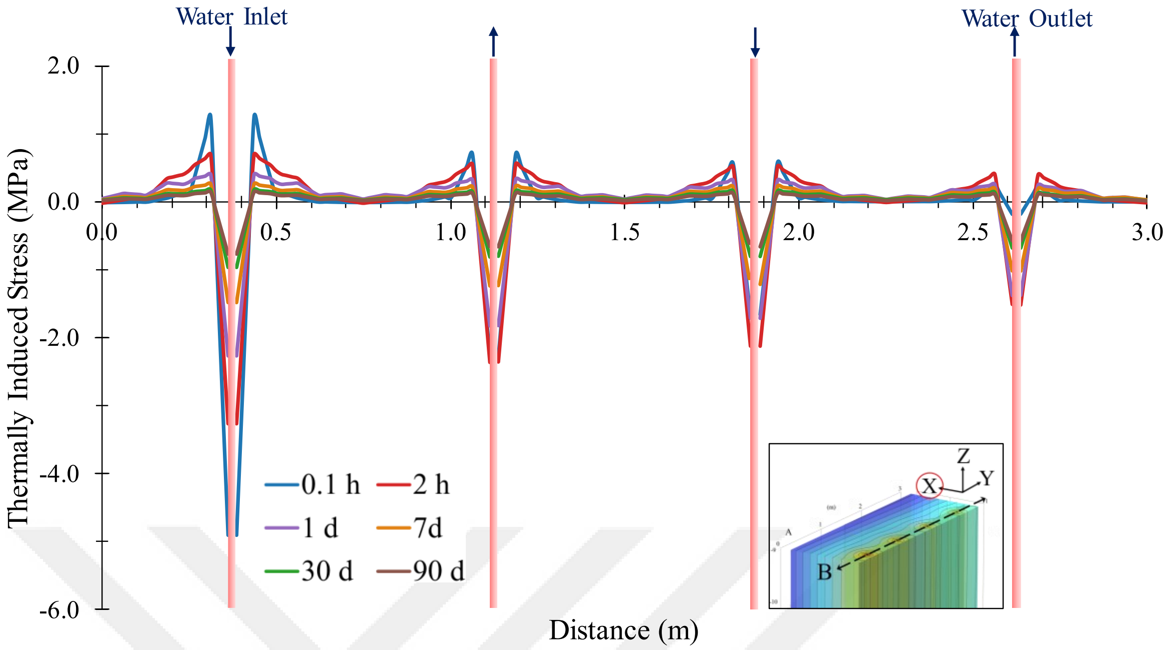

Figure 7.14. Thermally induced stresses in the X-direction at Section B for the heat injection case.

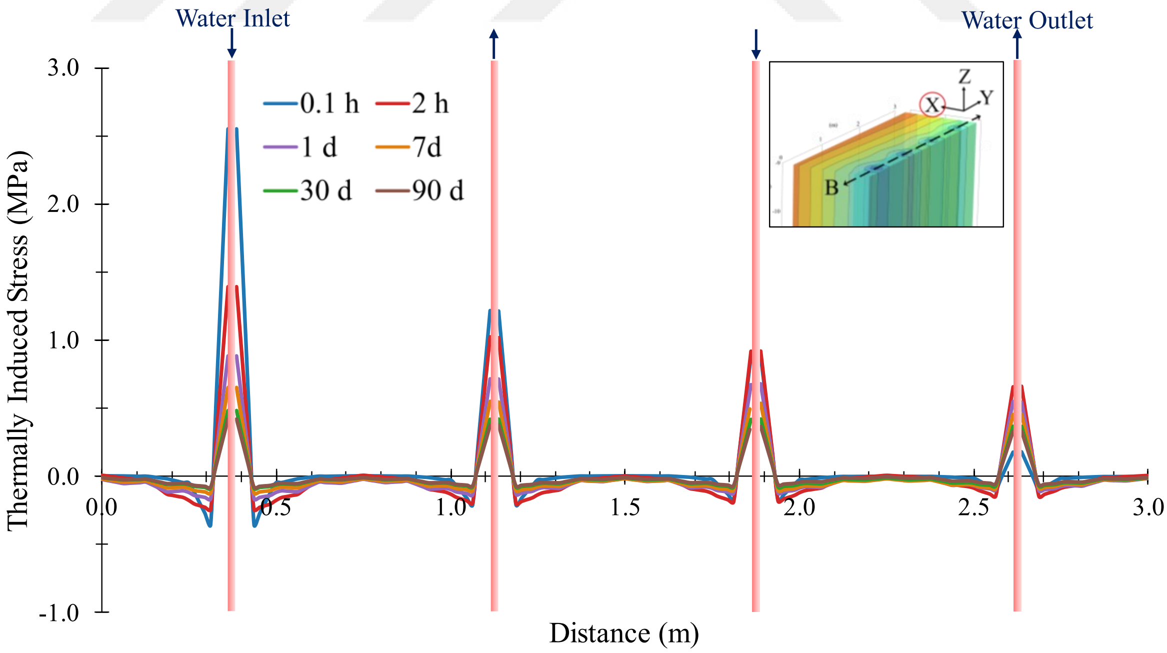

Figure 7.15. Thermally induced stresses in the X-direction at Section B for the heat extraction case.

Figures 7.16 and 7.17 display the thermally induced stress distributions in the Y direction for both thermal loading scenarios. In Section B, the Y direction corresponds to the radial direction in cylindrical coordinates, and the observed stresses represent radial thermally induced stresses.

In both heat injection and extraction cases, thermally induced stresses near the inlet pipe evolve considerably over time due to the restriction along the Y-axis and variations in the local temperature field. This axis constrains lateral deformation, resulting in a temporal shift in stress profiles, evidenced by gradual vertical changes over the simulation period. In Zone 1, the temperature gradient decreases steadily, reducing the driving force for thermal stress development and consequently flattening the stress curves over time.

During heat injection, radial compressive stresses near the inlet pipe peak at approximately 6.22 MPa within the first 0.1 hours. Although a slight reduction follows this peak, the stresses then increase steadily, reaching about 8.80 MPa by day 90. In the heat extraction scenario, radial tensile stresses rise to approximately 2.85 MPa within 0.1 hours and, after an initial decline, gradually increase to around 3.30 MPa by day 90. These trends are governed by the diminishing thermal gradient near the pipe wall and the consistent boundary constraint along the Y-axis, which dominates the stress evolution as time progresses.

At the midpoints between adjacent pipes, the stress distribution remains consistent within each time interval, with no radial thermally induced stresses developing in this region. This is due to the absence of a circular temperature distribution in Zone 2, where the thermal gradient follows a different pattern. However, stresses in this region gradually increase over time due to the constraints on the wall.

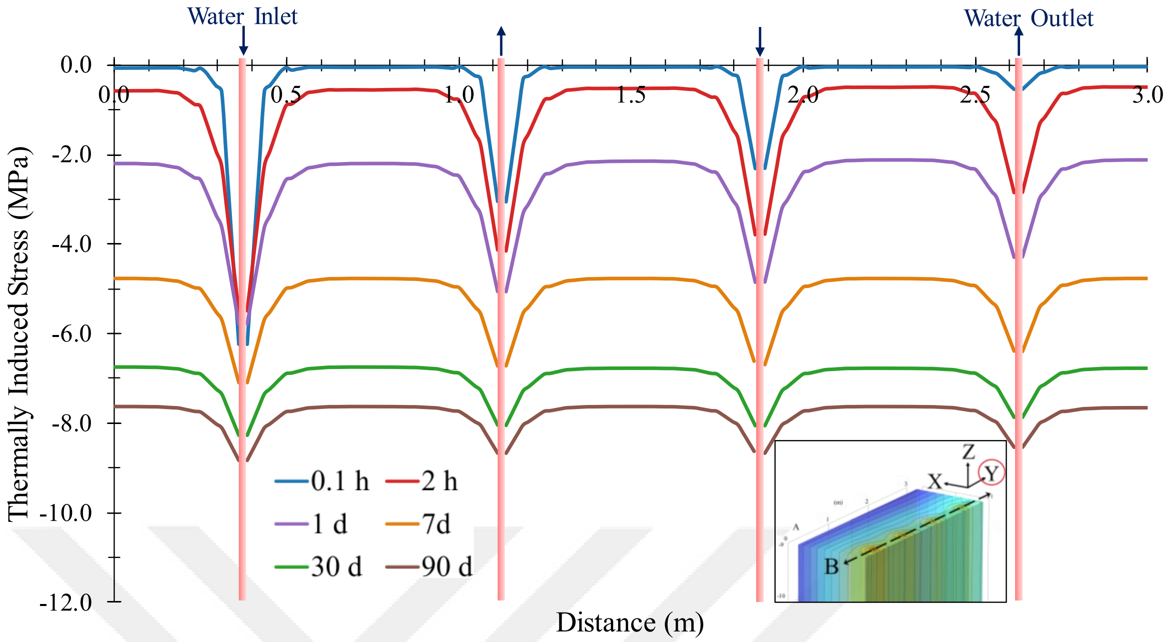

Figure 7.16. Thermally induced stresses in the Y-direction at Section B for the heat injection case.

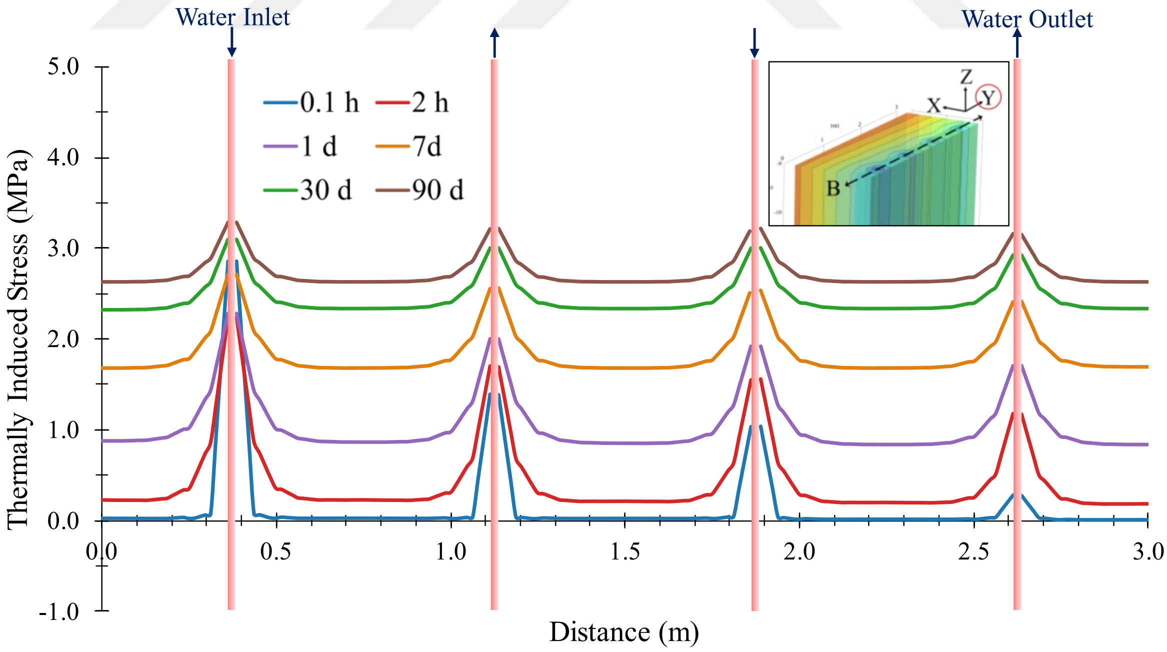

Figure 7.17. Thermally induced stresses in the Y-direction at Section B for the heat extraction case.

For the heat injection and heat extraction scenarios, thermally induced stresses in the Z-direction at Section B are shown in Figures 7.18 and 7.19, respectively. As outlined in Section 2, Zone 1 corresponds to the axial direction in the cylindrical coordinate system for the Z-direction at Section B, like Section A.

In Zone 1, near the inlet pipe under the heat injection scenario, thermally induced compressive stresses develop rapidly, reaching approximately 7.80 MPa within 0.1 hours. These stresses continue to increase, peaking at around 8.65 MPa compression at 2 hours before gradually decreasing to approximately 4.15 MPa by day 90. Conversely, in the heat extraction scenario, thermally induced tensile stresses initially form, reaching about 3.24 MPa within 0.1 hours. These tensile stresses further increase to approximately 3.45 MPa at 2 hours before gradually declining to around 2.40 MPa tension by day 90. This stress evolution closely aligns with the progression of the temperature gradient around the pipes, which, as shown in Figures 7.4 and 7.5, rises until 2 hours before gradually diminishing.

At the outer boundary of Zone 1, a distinct stress transition occurs. In the heat injection scenario, thermally induced stresses initially manifest as minor tension at 0.1 hours but quickly shift to compression. In the heat extraction scenario, initial compressive stresses (close to zero) develop at 0.1 hours before rapidly transitioning to tension. Although no external vertical load is applied in this analysis, the soil-structure interaction at the soil-wall interface plays a significant role in shaping this stress development pattern.

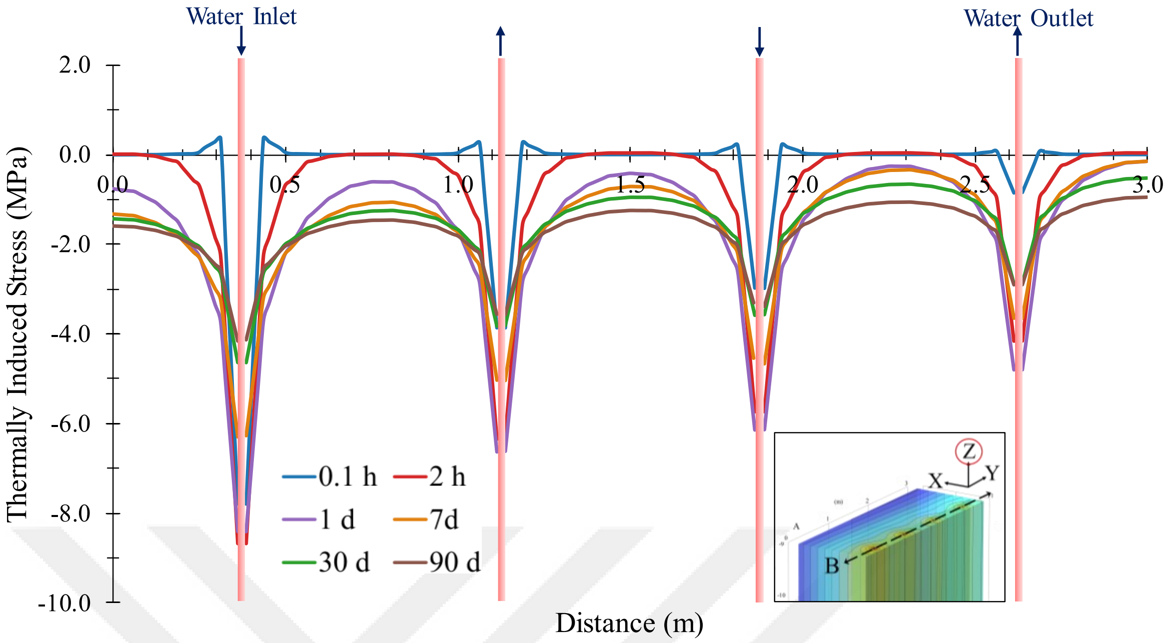

Figure 7.18. Thermally induced stresses in the Z-direction at Section B for the heat injection case.

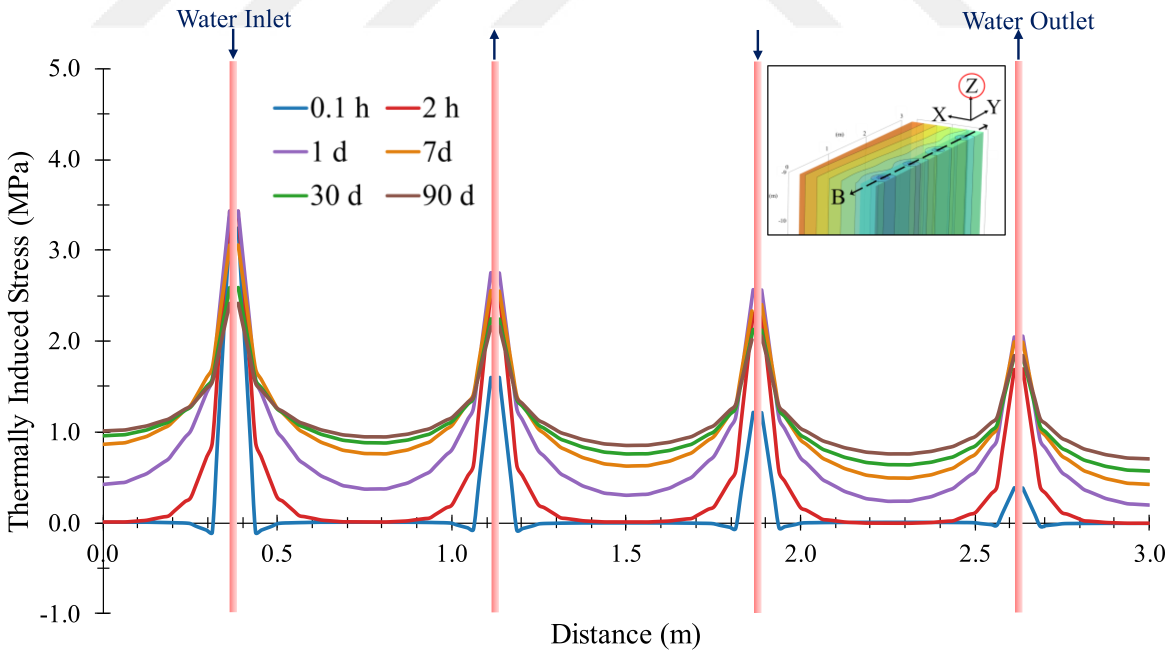

Figure 7.19. Thermally induced stresses in the Z-direction at Section B for the heat extraction case.

8. STRATEGIES TO MINIMIZE THERMALLY INDUCED STRESSES

Energy walls are multifunctional structural systems that simultaneously serve as load-bearing elements and enable geothermal energy exchange. However, due to their exposure to thermal fluctuations during operation, they are prone to developing non-uniform temperature distributions across their cross-sectional plane. These uneven temperature gradients lead to differential thermal expansion within the concrete, as regions closer to embedded pipes heat up more rapidly than outer zones. The resulting mismatch in thermal strain creates complex internal deformation patterns and stress accumulations in multiple directions. To ensure the long-term structural integrity of energy walls and to manage thermally induced stresses effectively, various design and operational strategies have been proposed. Nonetheless, the effectiveness of these strategies should be verified through dedicated experimental studies and detailed numerical analyses specific to the geometry and boundary conditions of each application.

One of the suggested approaches is to enhance the concrete's resistance to cracking by incorporating fiber reinforcement. Fibers such as steel or glass can significantly improve the tensile performance of the concrete matrix. When exposed to non-uniform tensile thermal stresses, fiber-reinforced concrete may delay the onset of cracking or limit its spread. This improvement is particularly valuable in summer operation, where sharp temperature gradients often form in the concrete cover between the heat exchanger pipes and surrounding soil. Still, the degree of benefit from fiber use varies depending on wall geometry, fiber type, and dosage. Therefore, the actual contribution of this method should be validated through focused material testing and modeling efforts.

Another important recommendation is to avoid sudden shifts to high operational temperatures. Allowing the system to gradually reach its target temperature enables the concrete to respond more smoothly to thermal changes. Such a stepwise heating approach promotes a more even distribution of temperature across the section and reduces abrupt stress accumulation. Rapid expansion near the pipes, when restrained by cooler concrete at the edges, can generate tensile stresses. Therefore, controlling the rate of temperature increase during system start-up may serve as a practical mitigation strategy for such effects.

Equally important is the uniform and sufficiently dense arrangement of heat exchanger pipes within the energy wall section. A closely spaced and symmetrical piping layout can promote a more homogeneous thermal field, thereby reducing temperature gradients that might otherwise trigger localized stress concentrations. However, increasing the number of pipes may not always be feasible due to efficiency trade-offs and potential increases in construction costs. For this reason, determining the optimal pipe spacing and configuration requires project-specific evaluation. Numerical modeling can be a powerful tool in this context, allowing designers to balance thermal performance, mechanical integrity, and economic feasibility by simulating various pipe layouts under realistic boundary conditions.

In addition, efforts to improve the thermal conductivity of concrete can help smooth temperature transitions across the wall section. Higher thermal conductivity allows heat to disperse more uniformly and quickly through the concrete, reducing the intensity of temperature differentials. This can be especially beneficial in zones where heat changes rapidly. The thermal conductivity of concrete is influenced by multiple factors, including the type and proportion of aggregate, the presence of specific additives or fibers. However, it is important to note that such modifications can also affect the mechanical behaviour of concrete. Therefore, any alteration aimed at enhancing thermal conductivity should be evaluated holistically within the material and structural design context.

In summary, the strategies outlined above represent potential methods to control thermally induced stress development in energy walls. However, their true effectiveness cannot be fully understood through theoretical reasoning alone. It is essential to support these approaches with application-specific testing, calibrated numerical modeling, and realistic simulations. Such comprehensive investigations will not only improve the structural safety of energy walls but also enhance their long-term energy performance and operational reliability.

9. CONCLUSIONS

This study focused on evaluating thermally induced stresses within energy walls under realistic heat injection (summer) and heat extraction (winter) operational conditions. Special emphasis was placed on understanding how non-uniform temperature distributions influence the structural response of these multifunctional geostructures. A validated numerical model was developed using COMSOL Multiphysics, allowing detailed analyses of both temporal and spatial variations in temperature gradients and resulting stress distributions across critical sections of the energy wall.

The results clearly highlighted the importance of considering realistic, non-uniform temperature gradients, as well as their interactions with structural constraints, since these factors significantly affect the thermo-mechanical behaviour of energy walls. To systematically interpret the temperature variations observed, the wall cross-section was categorized into three distinct zones, each characterized by unique thermal distribution patterns. These zones included Zone 1, exhibiting a circular temperature distribution around the embedded thermal pipes; Zone 2, defined as a transitional area where the temperature field gradually changed from circular to linear; and Zone 3, characterized by a linear temperature gradient near the building-facing side. Notably, the geometry and intensity of the temperature gradients within these zones varied distinctly over time. Zone 1 displayed rapid initial temperature changes, followed by a gradual reduction, whereas Zone 3 experienced a continuous increase in temperature gradients as heat propagated progressively through the wall thickness.

The geometry and intensity of these temperature distributions, along with the imposed boundary constraints, played a fundamental role in determining the magnitudes and spatial distribution of thermal stresses within the wall. Specifically, radial and circumferential stresses were found exclusively within Zone 1, closely linked to the circular geometry of the temperature field around the pipes. Over time, as the temperature gradient diminished and transitioned from circular to linear, these stresses gradually decreased and eventually disappeared.

Additionally, clear differences emerged between the stress distribution patterns observed during heating and cooling conditions. During the heat injection scenario, significant compressive stresses quickly developed around the heated regions adjacent to the thermal pipes. Simultaneously, tensile stresses appeared prominently at the soil-wall interface, particularly during the initial stages of heating. On the building-facing side of the wall, vertically oriented tensile stresses gradually built up throughout the entire heating duration, becoming notably significant by the conclusion of the simulation period.

Conversely, the heat extraction scenario revealed an opposite stress development pattern. Pronounced tensile stresses initially emerged near the cooled areas around the pipes, decreasing gradually with distance. Closer to the soil-wall interface, these stresses transitioned into compressive stresses that intensified progressively, especially during the early phase of cooling. Likewise, compressive stresses became more pronounced over time at the excavation-facing surface of the wall, indicating a distinctly different thermo-mechanical response compared to the heat injection case.

The study's findings emphasize that thermally induced stresses within energy walls can reach substantial levels under realistic operational conditions. Given the relatively low tensile strength characteristic of concrete, particularly the tensile stresses identified in this study may pose significant risks to the structural integrity of energy walls. Therefore, careful consideration and detailed assessment of these stresses are essential in the design phase to ensure long-term safety and functionality.

To manage the development of thermally induced stresses in energy walls, several practical strategies can be considered during the design and operational phases. One approach is to enhance the concrete’s resistance to cracking by incorporating fiber reinforcement, which can help control stress-related damage, especially in regions experiencing high temperature gradients. Another useful method is to gradually increase system temperatures during start-up, rather than applying full heat immediately. This allows the wall to adapt more evenly and reduces sudden internal stress build-up. A well-balanced and uniform pipe layout within the wall can also support more homogeneous heat distribution, although the number and spacing of pipes should be optimized with respect to performance and cost through project-specific evaluations. Lastly, improving the thermal conductivity of the concrete mix may help even out temperature differences across the section, contributing to a more stable stress profile. While these strategies are proposed as potential solutions, their effectiveness should be further verified through focused testing and numerical studies tailored to the characteristics of each project.

In conclusion, this study highlights the critical necessity of accurately representing non-uniform temperature fields and realistic structural constraints when evaluating the thermo-mechanical response of energy walls. Traditional simplified methods, which often assume uniform temperature distributions and neglect complex interactions with structural boundaries, can lead to inaccurate predictions, underestimating critical stress conditions. Consequently, this research underscores the importance and utility of employing detailed numerical modeling approaches, such as the one developed herein, to reliably predict the structural behaviour of energy geostructures and thus contribute to safer, more effective, and sustainable designs.

REFERENCES

Abdelaziz, S., and T. Y. Ozudogru, 2016, “Non-Uniform Thermal Strains and Stresses in Energy Piles”, *Environmental Geotechnics*, Vol. 3, No. 4, pp. 237–252.

Alqawasmeh, Q. I., G. A. Narsilio, N. Makasis, and M. J. Kreitmair, 2024, “The Impact of Soil Layering and Groundwater Flow on Energy Pile Thermal Performance”, *Geomechanics for Energy and the Environment*, Vol. 38.

Anis Akrouch, G., M. Sánchez, and J. L. Briaud, 2020, “Thermal Performance and Economic Study of An Energy Piles System Under Cooling Dominated Conditions”, *Renewable Energy*, Vol.147, pp. 2736–2747.

ASHRAE Data Viewer 5.0 [Computer software], 2013, American Society of Heating, Refrigerating and Air-Conditioning Engineers, Georgia, United States.

Barbier, E, 2002, “Geothermal Energy Technology and Current Status: An Overview”, *Renewable and Sustainable Energy Reviews*, Vol. 6, pp. 3-65.

Batini, N., A. F. Rotta Loria, P. Conti, D. Testi, W. Grassi, and L. Laloui, 2015, “Energy and Geotechnical Behaviour of Energy Piles for Different Design Solutions”, *Applied Thermal Engineering*, Vol. 86, pp. 199–213.

Bodas Freitas, T. M., R. A. Matos Sirgado, P. J. Bourne-Webb, and D. N. de Jesus Silva, 2024, “The Influence of Geometry on The Heat Exchange Potential of Embedded Planar Retaining Walls with Seasonally-Balanced Thermal Load”, *Applied Thermal Engineering*, Vol. 246.

ten Bosch, S., E. Ravera, and L. Laloui, 2024, “Performance of Energy Piles Foundation in Hot-Dominated Climate: A Case Study in Dubai”, *Renewable Energy*, Vol. 220.

Bourne-Webb, P. J., T. M. Bodas Freitas, and R. A. Da Costa Gonçalves, 2016, "Thermal and Mechanical Aspects of The Response of Embedded Retaining Walls Used as Shallow Geothermal Heat Exchangers", *Energy and Buildings*, Vol. 125, pp. 130–141.

Brandl, H, 2006, "Energy Foundations and Other Thermo-Active Ground Structures", *Geotechnique*, Vol. 56, No. 2, pp. 81–122.

Brettmann, T., and T. Amis, 2011, "Thermal Conductivity Evaluation of a Pile Group Using Geothermal Energy Piles", *Geo-Frontiers 2011, Dallas, Texas, United States*.

Cecinato, F., and D. Salciarini, 2022, "Energy Performance Assessment of Thermo-Active Micro-Piles Via Numerical Modeling and Statistical Analysis", *Geomechanics for Energy and the Environment*, Vol. 29.

Chen, R., D. Wu, T. Zhang, G. Kong, and J. Fang, 2025, "Thermo-Mechanical Behavior of Energy Piles Equipped with PCM Tubes", *Computers and Geotechnics*, Vol. 179.

Chen, Z., X. Lian, J. Tan, H. Xiao, Q. Ma, and Y. Zhuang, 2023, "Study on Heat-Exchange Efficiency and Energy Efficiency Ratio of a Deeply Buried Pipe Energy Pile Group Considering Seepage and Circulating-Medium Flow Rate", *Renewable Energy*, Vol. 216.

Dai, Q., A. F. Rotta Loria, and J. Choo, 2022, "Effects of Internal Airflows on The Heat Exchange Potential and Mechanics of Energy Walls", *Renewable Energy*, Vol. 197, pp. 1069–1080.

Di Donna, A., F. Loveridge, M. Piemontese, and M. Barla, 2021, "The Role of Ground Conditions on The Heat Exchange Potential of Energy Walls", *Geomechanics for Energy and the Environment*, Vol. 25.

Erginag, U. C., M. Guner, S. Polat, M. Sutman, and O. Cinicioglu, 2025, "Thermally Induced Tensile Hoop Stresses in Energy Piles: Implications for Design and Operation", *Geomechanics for Energy and the Environment*, Vol. 43.

Faizal, M., A. Bouazza, and J. S. McCartney, 2025, "The Impact of Heat Exchanger Loop Configuration on Heat Transfer in Energy Piles", *Geomechanics for Energy and the Environment*, Vol. 41.

Faizal, M., A. Bouazza, J. S. McCartney, and C. Haberfield, 2019, "Axial and Radial Thermal Responses of Energy Pile Under Six Storey Residential Building", *Canadian Geotechnical Journal*, Vol. 56, No. 7, pp. 1019–1033.

Faizal, M., A. Bouazza, and R. M. Singh, 2016, "An Experimental Investigation of The Influence of Intermittent and Continuous Operating Modes on The Thermal Behaviour of a Full Scale Geothermal Energy Pile", *Geomechanics for Energy and the Environment*, Vol. 8, pp. 8–29.

Fang, J., G. Kong, Y. Meng, L. Wang, and Q. Yang, 2020, "Thermomechanical Behavior of Energy Piles and Interactions Within Energy Pile–Raft Foundations", *Journal of Geotechnical and Geoenvironmental Engineering*, Vol. 146, No. 9.

Hassani Nezhad Gashti, E., M. Malaska, and K. Kujala, 2014, "Evaluation of Thermo-Mechanical Behaviour of Composite Energy Piles During Heating/Cooling Operations", *Engineering Structure*, Vol. 75, pp. 363–373.

Hu, C., J. Cui, M. Wang, Y. Zhang, J. Luo, and L. Li, 2025, "Optimizing the Restoration Performance of Pipe Energy Piles Using Energy Injection in Winter Mode: A Numerical Investigation", *Journal of Energy Storage*, Vol. 114.

Kalogirou, S., and G. Florides, 2005, "Measurements of Ground Temperature at Various Depths", *8th REHVA World Congress,* Lausanne, Switzerland.

Laloui, L., and M. Sutman, 2021, "Experimental Investigation of Energy Piles: From Laboratory to Field Testing", *Geomechanics for Energy and the Environment*, Vol. 27.

Laloui, L., and A. F. Rotta Loria, 2020, *Analysis and Design of Energy Geostructures*, Academic Press, Cambridge.

Lee, S., J.G. Speight, S.K. Loyalka, 2007, *Handbook of Alternative Fuel Technologies*, CRC Press, Boca Raton.

Lou, Y., P. fei Fang, X. yu Xie, C. S. A. Chong, F. yuan Li, C. yang Liu, Z. jin Wang, and D. yong Zhu, 2021, "Numerical Research on Thermal Response for Geothermal Energy Pile Groups Under Groundwater Flow", *Geomechanics for Energy and the Environment*, Vol. 28.

Makasis, N., and G. A. Narsilio, 2020, "Energy Diaphragm Wall Thermal Design: The Effects of Pipe Configuration and Spacing", *Renewable Energy*, Vol. 154, pp. 476-487.

Makasis, N., and G. A. Narsilio, 2022, "Investigating the Thermal Performance of Energy Soldier Pile Walls", *Geomechanics for Energy and the Environment*, Vol. 30.

Makasis, N., G. A. Narsilio, A. Bidarmaghz, I. W. Johnston, and Y. Zhong, 2020, "The Importance of Boundary Conditions on The Modelling of Energy Retaining Walls", *Computers and Geotechnics*, Vol. 120.

Mi, M., G. Cai, X. Li, H. Li, W. Zheng, and Y. Shi, 2024, "Investigation on Heat Transfer Performance of Energy Diaphragm Walls Under Groundwater Flow Condition", *Journal of Building Engineering*, Vol. 88.

Moradshahi, A., M. Faizal, A. Bouazza, and J. S. McCartney, 2021, "Cross-Sectional Thermo-Mechanical Responses of Energy Piles", *Computers and Geotechnics*, Vol. 138.

Moradshahi, A., M. Faizal, A. Bouazza, and J. S. McCartney, 2022, "Thermomechanical Responses of Thermally Interacting Field-Scale Energy Piles", *International Journal of Geomechanics*, Vol. 22, No. 11.

Ng, C. W. W., A. Farivar, S. M. M. H. Gomaa, and F. Jafarzadeh, 2021, "Centrifuge Modeling of Cyclic Nonsymmetrical Thermally Loaded Energy Pile Groups in Clay", *Journal of Geotechnical and Geoenvironmental Engineering*, Vol. 147, No. 12.

Ng, C. W. W., C. Shi, A. Gunawan, L. Laloui, and H. L. Liu, 2015, "Centrifuge Modelling of Heating Effects on Energy Pile Performance in Saturated Sand", *Canadian Geotechnical Journal*, Vol. 52, No. 8, pp. 1045–1057.

Ou, C. Y., 2006, *Deep Excavation: Theory and Practice*, Taylor & Francis, London.

Park, H., S. R. Lee, S. Yoon, and J. C. Choi, 2013, "Evaluation of Thermal Response and Performance of PHC Energy Pile: Field Experiments and Numerical Simulation", *Applied Energy*, Vol. 103, pp. 12–24.

Polat, S., U. C. Erginag, M. Guner, O. Cinicioglu, and M. Sutman, 2024, "A Model-Scale Test Setup Development to Monitor Temperature and Moisture Content Variations Around Energy Piles", *Geotechnical Engineering Challenges to Meet Current and Emerging Needs of Society*, pp. 3247–3250, CRC Press.

Polat, S., M. Guner, U. C. Erginag, M. Sutman, and O. Cinicioglu, 2025, "Analyses of Thermoactive Piles Considering Surface Radiation and Wind Convection Effects", *International Journal of Geomechanics*, Vol. 25, No. 1.

Ravera, E., A. F. Rotta Loria, and L. Laloui, 2024, "Performance of Complex Energy Geostructures", *Geomechanics for Energy and the Environment*, Vol. 38.

Sailer, E, 2020, *Numerical Modelling Of Thermo-Active Retaining Walls,* Ph.D Thesis, Imperial College London.

Soga, K., and Y. Rui, 2016, *Energy Geostructures, In S. J. Rees, Advances in Ground-Source Heat Pump Systems*, Woodhead Publishing, Cambridge.

Sterpi, D., A. Coletto, and L. Mauri, 2017, "Investigation on The Behaviour of a Thermo-Active Diaphragm Wall by Thermo-Mechanical Analyses", *Geomechanics for Energy and the Environment*, Vol. 9, pp. 1–20.

Sterpi, D., G. Tomaselli, and A. Angelotti, 2020, "Energy Performance of Ground Heat Exchangers Embedded in Diaphragm Walls: Field Observations and Optimization by Numerical Modelling", *Renewable Energy*, Vol. 147, pp. 2748–2760.

Stewart, M. A., and J. S. McCartney, 2014, "Centrifuge Modeling of Soil-Structure Interaction in Energy Foundations", *Journal of Geotechnical and Geoenvironmental Engineering*, Vol. 140, No. 4.

Sun, M., C. Xia, and G. Zhang, 2013, "Heat Transfer Model and Design Method for Geothermal Heat Exchange Tubes in Diaphragm Walls", *Energy and Buildings*, Vol. 61, pp. 250–259.

Sutman, M, 2016, *Thermo-Mechanical Behavior of Energy Piles: Full-Scale Field Testing and Numerical Modeling*, Ph.D Thesis, Virginia Polytechnic Institute and State University.

Sutman, M., T. Brettmann, and C. G. Olgun, 2019a, "Full-Scale In-Situ Tests on Energy Piles: Head and Base-Restraining Effects on The Structural Behaviour of Three Energy Piles", *Geomechanics for Energy and the Environment*, Vol. 18, pp. 56–68.

Sutman, M., C. G. Olgun, and L. Laloui, 2019b, "Cyclic Load–Transfer Approach for the Analysis of Energy Piles", *Journal of Geotechnical and Geoenvironmental Engineering*, Vol.145, No. 1.

Sutman, M., G. Speranza, A. Ferrari, P. Larrey-Lassalle, and L. Laloui, 2020, "Long-Term Performance and Life Cycle Assessment of Energy Piles in Three Different Climatic Conditions", *Renewable Energy*, Vol. 146, pp. 1177–1191.

Vitali, D., A. K. Leung, S. Feng, J. A. Knappett, and L. Ma, 2022, “Centrifuge Modelling of The Use of Discretely Spaced Energy Pile Row to Reinforce Unsaturated Silt”, *Geotechnique*, Vol. 72, No. 7, pp. 618–631.

Xia, C., M. Sun, G. Zhang, S. Xiao, and Y. Zou, 2012, “Experimental Study on Geothermal Heat Exchangers Buried in Diaphragm Walls”, Energy *and Buildings*, Vol. 52, pp. 50–55.

Yang, W., W. Xia, Y. Qiang, and F. Wang, 2025, “Experimental and Numerical Investigations on Thermo-Mechanical Behaviours of Energy Pile Group with Different Seepage Parameters”, *Construction and Building Material*, Vol. 472.

Zannin, J., A. Ferrari, P. Larrey-Lassalle, and L. Laloui, 2022, “Early-Stage Thermal Performance Design of Thermo-Active Walls Implemented in Underground Infrastructures”, *Geomechanics for Energy and the Environment*, Vol. 30.

Zeng, C., F. Tang, Y. Yuan, X. Cao, F. Haghighat, and K. Panchabikesan, 2021, “Thermal Performance of Energy Diaphragm Wall (EDW) Adjacent to Air-Conditioned Space from The Underground-Engineering Perspective”, *Geothermics*, Vol. 91.

Zhao, Q., B. Chen, and F. Liu, 2016, “Study on The Thermal Performance of Several Types of Energy Pile Ground Heat Exchangers: U-Shaped, W-Shaped and Spiral-Shaped”, *Energy and Buildings*, Vol. 133, pp. 335–344.

Zhou, X., Y. Yuan, Z. Leng, X. Cao, and C. Zeng, 2023, “Numerical Study on The Thermal-Induced Mechanical Behavior in Deep Energy Diaphragm Wall (EDW): The Long-Term Soil Elastoplastic Effects”, *Tunnelling and Underground Space Technology*, Vol. 132.

Zhu, P., C. Wang, G. Kong, and X. Ding, 2024, “Effects of The Ground Surface Thermal Boundary Condition on The Long-Term Thermal Performance of Energy Diaphragm Walls”, *Applied Thermal Engineering*, Vol. 236.